TESTING RPC PERFORMANCE WITH DISCHARGES IGNITED BY UV LASER PULSES:
PRECISE MEASUREMENT OF GAS PARAMETERS IN APPROXIMATELY REALISTIC RPC CONFIGURATIONS

Xingming Fan

**WISSENSCHAFTLICH-
TECHNISCHE BERICHTE**

HZDR

HELMHOLTZ
ZENTRUM DRESDEN
ROSSENDORF

Xingming Fan

TESTING RPC PERFORMANCE WITH DISCHARGES IGNITED BY UV LASER PULSES: PRECISE MEASUREMENT OF GAS PARAMETERS IN APPROXIMATELY REALISTIC RPC CONFIGURATIONS

HZDR

HELMHOLTZ
ZENTRUM DRESDEN
ROSSENDORF

TECHNISCHE UNIVERSITÄT DRESDEN

Testing RPC Performance
with Discharges Ignited by UV Laser Pulses:

Precise measurement of gas parameters
in approximately realistic RPC configurations

Dissertation

zur Erlangung des wissenschaftlichen Grades
Doktor rerum naturalium

vorgelegt von

Xingming Fan
geboren am 16.11.1988 in Beijing, China

Fakultät Mathematik und Naturwissenschaften

der Technischen Universität Dresden

2019

Eingereicht am:

1. Gutachter: Prof. Dr. B. Kämpfer

2. Gutachter: Prof. Dr. A. Straessner

Verteidigt am:

Abstract

This thesis is devoted in two associated topics: a unique laser facility for researches of gaseous detectors; the investigations of Resistive Plate Chamber (RPC) detectors and the measurement of gas parameters in a realistic condition of timing RPC.

A pulsed UV laser test facility is assembled in HZDR. The focus of laser pulses is placed in a specific position in a gaseous detector sample to produce laser plasma, where electrons are ionized with well defined number, micro-meter scale and micro-meter spatial accuracy. It provides a method, independent from accelerators, to make investigations with gaseous detectors in a laboratory.

Samples of RPC detectors are designed and assembled for experiments with the laser test facility. Methods are developed to acquire the waveforms of electron avalanches for different drift lengths and to obtain the key gas parameters: the effective Townsend coefficient and the electron drift velocity. We have succeeded in the direct measurement of gas parameters at the field strength of timing RPC under atmospheric pressure for the first time in experimental condition.

The research has acquired different achievements. The laser test facility is proven to be a powerful tool for the measurement of gas parameters, and has a potential to contribute to the eco-gas research for future RPC. The possible measurement range of electric field of gas parameter in atmospheric pressure is extended by a factor of two, from the range of trigger RPC to timing RPC. The results of experiments have revealed some fundamental mechanisms, which will extend the understanding of RPC performance and electron avalanche process.

Zusammenfassung

Diese Arbeit beschäftigt sich mit zwei miteinander verbundenen Themen: einer einzigartigen Laser-Testanlage für die Erforschung von gasgefüllten Detektoren sowie der Untersuchungen von Widerstandsplatten-Zählern (RPC) und der Messung von Gasparametern unter realistischen Bedingungen der Timing-RPC.

Eine gepulste UV-Laser-Testanlage wurde im HZDR aufgebaut. Der Fokus des Pikosekunden-Lasers wird in einem mit Zählergas gefüllten Detektor an einer bestimmten Stelle platziert, um ein Laser-Plasma zu erzeugen, wobei eine definierte Anzahl freier Elektronen durch Gas-Ionisation in einem Gas-Volumen mit einer Genauigkeit im Mikrometerbereich erzeugt wird. Es ist eine von Beschleunigern unabhängige Methode, um Untersuchungen an gasgefüllten Detektoren im Labor durchzuführen.

Proben von RPC-Detektoren wurden für Experimente mit der Laser-Testanlage entworfen und gefertigt. Es wurden Verfahren entwickelt, um die Wellenformen von Elektronenlawinen für verschiedene Elektronen-Driftlängen zu erfassen und die wichtigsten Gasparameter zu bestimmen: den effektiven Townsend-Koeffizienten und die Elektronendriftgeschwindigkeit. Erstmalig wurden die Gasparameter direkt für die hohe Feldstärke des Timings-RPC bei Atmosphärendruck unter Experimentbedingungen gemessen.

Es wurde gezeigt, dass sich die Laser-Testanlage für präzise Messungen der Gasparameter eignet und das Potenzial besitzt, um zur Öko-Gas-Forschung für zukünftige RPCs beizutragen. Der Messbereich des elektrischen Feldes der Gasparameter bei Atmosphärendruck wurde verdoppelt, vom Bereich des Trigger-RPC bis zu dem des Timing-RPC. Die Experimente haben einige grundlegende Mechanismen offenbart, die das Verständnis für die Eigenschaften von RPC und den Prozess der Elektronenlawine erweitern werden.

Contents

List of Figures

List of Tables

Chapter 1

Introduction

The Resistive Plate Chamber (RPC) technology plays an important role in high energy physics experiments [1] by providing timing information of charged particles with very high accuracy in the order of sub-hundred picoseconds. A RPC detector is a parallel plate gaseous detector with electrodes made of resistive material. The strong homogeneous electric field in the gas gap provides fast amplification of ionization signal or discharges. The simplicity of the structure of RPC provides high flexibility in the design of geometries and shapes. Because of its detection performance, including time resolution, spatial resolution, detection efficiency, stability, radiation hardness, relatively lower cost, manpower and budget, RPCs have been widely used in high energy physics and other fields.

The improvement of RPC technology relies on both experimental experiences and fundamental detector physics researches. Currently, the physical explanations for RPC performances have been established: the process from primary ionization to signal transmission are described [2, 3], and the Monte Carlo simulation methods and tools have been developed for simulations of the RPC performance.

However, difficulties still exist in fundamental researches because of the extreme high electric field. Currently, compared to the comprehensive physical model of signal process, direct experimental observations are still incomplete: a number of measurements are performed under reduced gas pressure and reduced electric field [4]; while some other measurements are operated at atmospheric pressure [5, 6], but cannot cover the full range of possible field strengths of RPCs; so that there is no direct measurement result of gas parameters at atmospheric pressure and field strength on excess of a certain range, because of the limitation of current experimental facilities.

The direct measurement data is important because, from the viewpoint of RPC detector physics, the effective Townsend coefficient and the electron drift velocity are fundamental variables for the characteristics of RPCs, including the avalanche process, the charge of signals, the time resolution of RPCs, etc. Currently, the physical model cannot fully explain the behaviour of RPC detectors in the range where the electric field strength is beyond the working field strength of trigger RPC. A direct measurement is needed to improve the understanding.

Meanwhile, an upcoming challenge for RPC technology is requiring further understanding of fundamental physics of RPC, where new methods and tools are necessary.

This thesis describes experimental studies aiming at the above mentioned objectives. A test system, named 'HZDR Laser-driven Detector Test Facility' is assembled with combined technologies aiming at a precise measurement of gas and RPC parameters. Series of experiments for the test of gas parameters are carried out.

This facility can analyse the properties of signals of gaseous detectors in a highly controlled situation: primary electrons are generated with controlled number and position near the laser focus. The devices, software and methods of the laser test facility were constantly upgraded and improved in the previous few years, and have been completed by the end of the year 2017. The RPC detectors in the laser test facility are designed and implemented similar to real RPC counters with very high homogeneous electric fields at atmospheric pressure and room temperature.

With the laser test facility, we are able to obtain the gas parameters at field strengths of up to $100\,\mathrm{kV/cm}$ at atmospheric pressure, being the only group in the world we know that could measure gas parameters in timing RPC under real RPC working conditions. Our measurement results have shown gradually deviation from simulation results or from the parameters measured in reduced gas pressure, when the electric field is beyond the range of trigger RPC.

This thesis will be devoted to two main parts: (i) development of the HZDR laser test facility, and (ii) a comprehensive overview measurement results of gas parameters.

The experimental results will be discussed and compared to existing data from simulations and experiments. Methods and phenomena during the experiments will also be cross compared to other works.

Chapter 2

Background

Investigation of the characteristic of matter under extreme experimental conditions is of high importance for the development of theories and methods in physics, especially for understanding astrophysical phenomena and the interaction of particles at a fundamental level. For this reason, high energy experiments are constructed and operated in different countries and facilities all over the world.

These experiments are usually operated in the following way: a beam of charged particles gains energy from an accelerator, then the high-energy particles interacts with a fixed target in the beam line or other accelerated particles from the opposite position in collider experiments. A system that contains different kinds of detectors is then constructed around the interaction point for a measurement of the characteristics of the emitted particles.

The research in this thesis involves in the Resistive Plate Chamber (RPC) detector in the Time-of-Flight (TOF) system of the Compressed Baryonic Matter (CBM) experiment at the future Facility of Antiproton and Ion Research (FAIR), in Darmstadt. In this chapter, a brief introduction of CBM and its TOF system will be presented.

2.1 The Compressed Baryonic Matter (CBM) experiment

2.1.1 Quantum Chromo-Dynamic and phase diagram of matter

Quantum Chromo-Dynamics (QCD) [7] is the commonly accepted theory of strong interaction. The theory describes the strong interactions between quarks and gluons, and how the quarks and gluons form hadrons such as protons, neutrons, pions, kaons, etc.

QCD exhibits two important properties: asymptotic freedom and chiral symmetry:

- The "theory of asymptotic freedom" has pointed out the fact that, for the energies much larger than a certain QCD energy scale of about $200\,\mathrm{MeV}$, the quarks and gluons interacts weakly. This behaviour is of the origin of the idea that, on relativistic and ultra relativistic heavy-ion collisions, a state of strongly interaction matter is called the quark-gluon plasma (QGP). On the other hand, of low energies, the interaction of quarks and gluons becomes strong, and quarks and gluons are confined into hadrons.

- The "theory of chiral symmetry" has pointed that for a certain kind of particles, another kind of particles with approximately same mass and opposite parity exists, such states of hadrons are called chiral partners. However, the chiral symmetry is spontaneously broken in the low energy sector. This chiral symmetry breaking greatly contributes to the mass generation of light quarks. It is expected that the chiral symmetry will be restored approximately for deconfined or QGP matter.

A thermodynamic QCD matter has two important external parameters: the temperature T and the net baryon density ρ_B, or its conjugate variable, the baryon-chemical potential μ_B. It is believed that there is a fine structure of the QCD phase diagram, shown in Figure 2.1.

The hadron phase shown in Figure 2.1 can be subdivided into several phases: for low T and μ_B, nuclear matter contains nucleons only; at medium T and μ_B, nucleons are excited to short-lived states (baryonic resonances) and mesons are emitted from their decay; at higher T, baryon-antibaryon pairs are created, and this mixtures of baryons, antibaryons, mesons, and strongly interacting nucleons are generally called hadronic matter.

For $\mu_B = 0$, the QCD phase transition has been carefully studied by lattice simulations. The result of the simulations has shown a smooth transition from hadronic phase to QGP at a temperature of about $155\,\mathrm{MeV}$, where deconfinement and chiral symmetry restoration sets in.

However, when $\mu_B \neq 0$, the present lattice QCD calculation method cannot be applied. From alternative models, it is very likely that there is a QCD critical point located at a certain value of $T = T_C$ and $\mu_B = \mu_C$, where the chiral transition crossover happens when $\mu_B < \mu_C$, and a first-order when $\mu_B > \mu_C$.

Given the uncertainties of $\mu_B > 0$, several options of the phase structure have been discussed, for instance, the critical point is where the two coincident transitions - deconfinement and chiral - became separated. The separated transition lines have given rise to the quarkyonic matter phase between the hadron phase and the QCD phase. The critical point is the triple point of hadron phase, quarkyonic matter phase and QGP phase. The search of the critical point is of high experimental interest.

If μ_B is so large that it far exceeds the boundary of hadronic phase, and the temperature is not very high, the nuclear matter will be in the colour superconducting phase. It is an analogue between electrons in metal, and quarks in quark matter. It is anticipated that the QCD matter at low T will form Cooper pairs leading to superconductivity [8].

2.1.2   Physical motivations of CBM

The phase diagram of QCD can be investigated by studying the strongly interacting nuclear matter under extreme conditions, where the transition from hadron to QGP appears. The extreme conditions in a laboratory can only be achieved by heavy ion collisions. In heavy-ion collisions, nucleus are accelerated to relativistic or ultra relativistic energies and brought to collisions to achieve high compressions and high temperatures.

In the past decades, great efforts, both experimental and theoretical, have been made for the exploration of QCD phase diagram. However, there is only limited experimental knowledge about it because of the high requirement of temperature and density.

Experimental results from the Large Hadron Collider (LHC) at CERN [9] and the Relativistic Heavy Ion Collider (RHIC) at BNL [10] have reported strong evidence of transition to QGP in recent years. In the experiments at LHC and RHIC, the energy of nucleus are accelerated to very high energies. In such a way, the properties about the QCD phase diagram at extremely
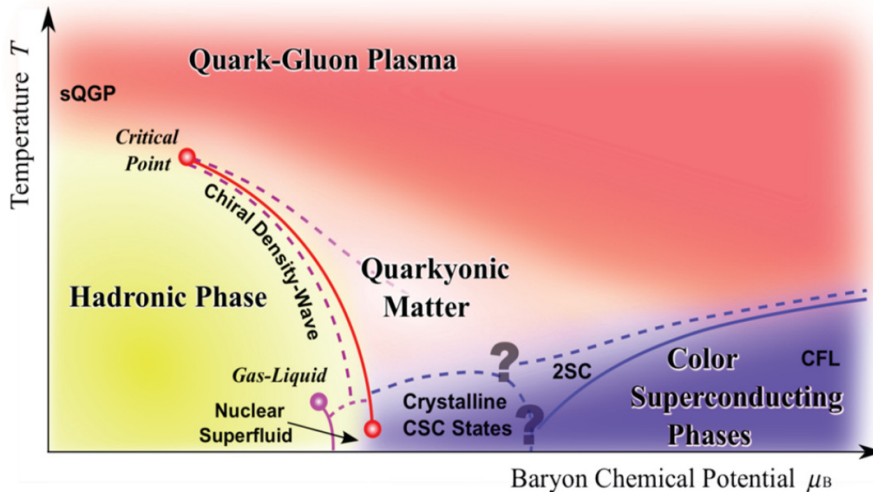
Figure 2.1: Schematic drawing of phase diagram of strongly interacting mat-
ter over wide scale of temperature and net baryon density. The
diagram exhibits the conjectured different states of matter.
The figure is a schematic drawing. In this figure, the maximum
value of baryon chemical potential is approximately 1 GeV, the
maximum value of temperature is approximately 200 MeV.
Figure is taken from [7].

high temperatures and small net-baryonic densities are probed.

At SPS and AGS [11] beam energies (fixed target experiments), the onset of deconfinement
effects has been claimed, but the evidences are not so obvious. At the UNILAC and SIS18 [12]
energies, one operates on a regime where hadron degrees of freedom are relevant.

Meanwhile, the QCD phase diagram has predicted the existence of QGP at large net baryon
density. A complementary discovery of QCD phase diagram in the region of high density will be
a great step in the understanding the rich structure of the QCD phase diagram. The exploration
in the high density region will be provided by Compressed Baryonic Matter (CBM) experiment
at Facility of Antiproton and Ion Research (FAIR) in Darmstadt, Germany. The different regions
accessible at above listed facilities are schematically shown in Figure 2.2.

CBM experiment is currently (in year 2018) under construction and will be one of the
most important scientific projects of FAIR [14, 15, 16]. The physical motivation of CBM is to
investigate rare probes as messengers of the dense phase of strongly interacting matter with
high accuracy. As the performances of rare probes can only be investigated by complete analysis
and reconstruction, the experimental setup is composed of subsystems with different objectives
and technologies. CBM will perform an important role in the exploration of the QCD phase
diagram in the region of high baryon densities with high-energy nucleus-nucleus collisions. In
the future facility of FAIR, the new research of compressed matter under QGP will be provided
presumably at the highest net baryon density accessible in laboratories.

2.1.3 Experimental setup

The CBM experiment is a fixed target experiment located at FAIR. A schematic view of the
layout of CBM is shown in Figure 2.3. The CBM will perform experiments with nucleus-nucleus,
proton-nucleus and proton-proton collisions. It will start with the SIS-100 synchrotron, with
protons up to 29 GeV, Au up to $11A$ GeV, nuclei with $Z/A = 0.5$ up to $14A$ GeV. In the future,
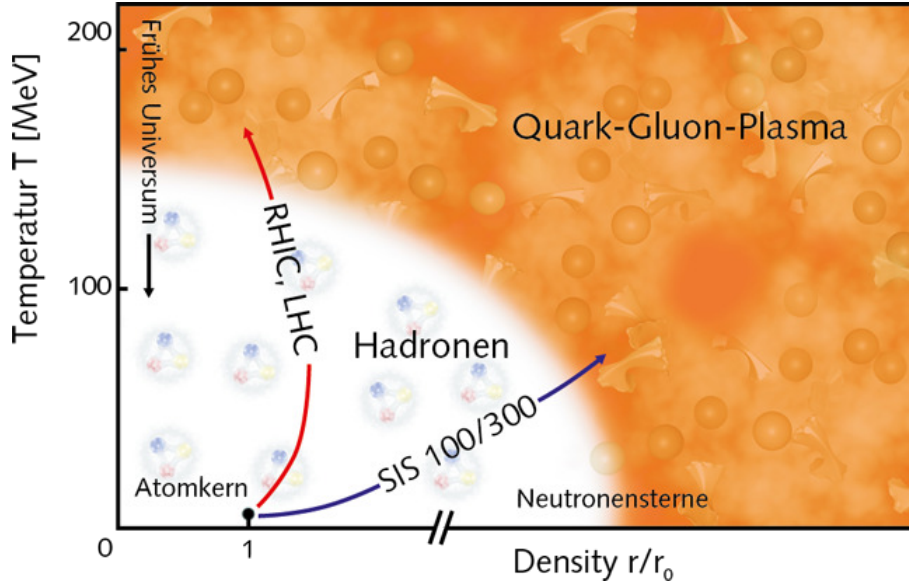
Figure 2.2: Schematic phase diagram similar to Figure 2.1, however, with the regions of research at different experimental facilities. The red line shows the existing experimental facilities operating at LHC and RHIC. The blue line shows the future experimental range of CBM SIS 100 and 300 with high net baryon density. The figure is taken from [13].

it will then continue with beams from SIS-300 synchrotron, with proton beams up to $90\,\mathrm{GeV}$, Au up to $35A$ GeV, nuclei with $Z/A = 0.5$ up to $45A$ GeV.

Two CBM configurations will be considered. Figures 2.4(i) and 2.4(ii) exhibit the setups with the electron detector and the muon detector options, respectively. Both of them will be realized by different stages.

The CBM system will contain several kinds of detectors for detection of different particles including hadrons, electrons and muons. The measurement will be performed with a reaction rate up to $10\,\mathrm{MHz}$, requiring fast and radiation hard detectors and high-speed data acquisition system to withstand the high luminosity environment.

CBM consists of the following components:

- The Superconducting Dipole Magnet [18]. It provides a field integral of $1\,\mathrm{Tm}$ for bending the tracks of charged particles according to their momenta and charges.

- Micro-Vertex Detector (MVD). It is the tracking device located behind the collision point designed for providing the information of first decays of short lived particles. The distance of the MVD to the target is only several centimeters. The MVD consists of four layers of high resolution detectors, placed at the distance of 5 to $20\,\mathrm{cm}$ respectively from the fixed target. The requirement of high spatial resolution and low budget, are met by the Monolithic Active Pixel Sensors (MAPS) [19]. The pixel size of the detector will be between $20\,\mu\mathrm{m} \times 40\,\mu\mathrm{m}$ and $18\,\mu\mathrm{m} \times 18\,\mu\mathrm{m}$, and the spatial resolution is 3.5 to $6\,\mu\mathrm{m}$ depending on the pixel size.

- Silicon-Tracking system (STS) [20]. The STS is the central detector to perform particle tracking reconstruction and measurement of momentum. The system consists of 8 tracking layers of silicon detectors, placed downstream of the target at the distance between 30 and $100\,\mathrm{cm}$ inside the magnet dipole field. The required momentum resolution is in the order of 1%.
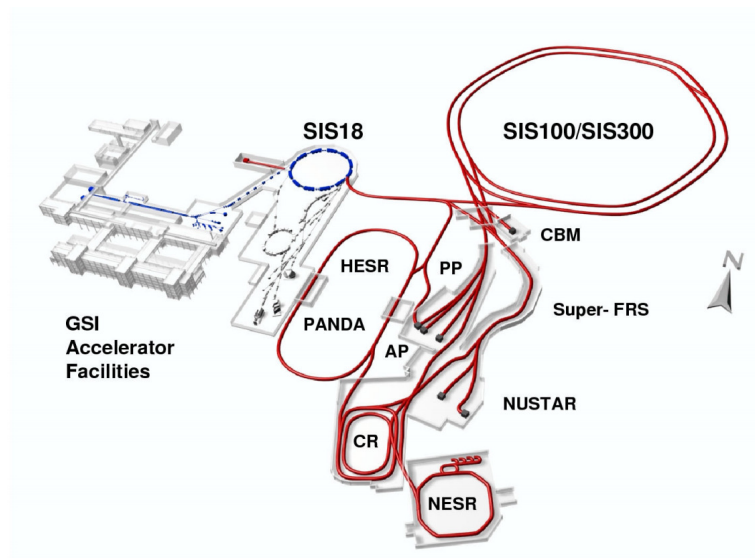
Figure 2.3: Schematic drawing of FAIR layout. It represents the experimental layout of the CBM experiment along with the full FAIR facility. Figure is taken from [17].
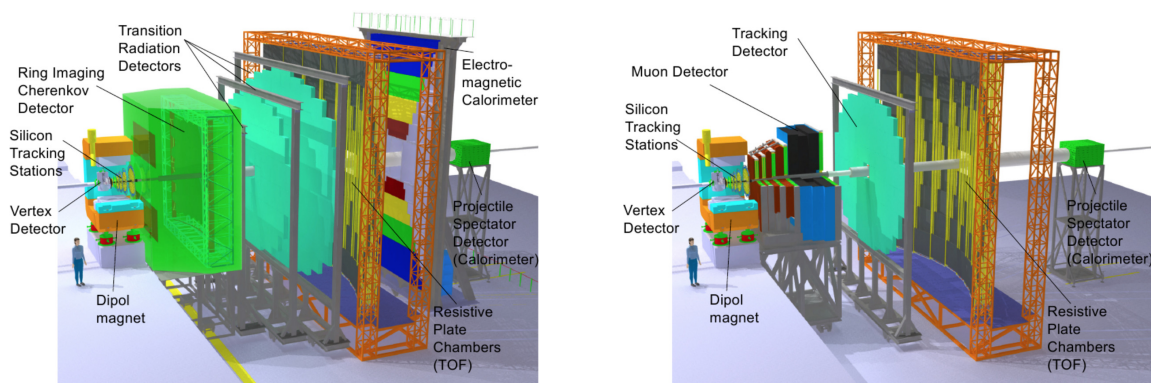
(i) The CBM experimental facility with the option of electron detectors RICH and TRD.

(ii) The CBM experimental facility with the option of the muon detection system.

Figure 2.4: Two experimental setup options for CBM experiment. All detector components of the CBM are presented in this figure. The figure is taken from [17].

- Ring-imaging Cherenkov Detector (RICH) [21]. It is designed for the identification of electrons and suppression of pions in the momentum range below $10\,\mathrm{GeV/c}$, by the measurements of their Cherenkov radiation. It is located behind the dipole magnet at the distance of about $1.6\,\mathrm{m}$ from the target. It is a gaseous RICH detector built in a standard projective geometry, with focusing mirror elements and a photon detector.

- Muon Chamber System (MUCH) [22]. It is applied in the configuration of muon-hadron radiation of experiment. It is designed for providing identifications of low-momentum muons in the environment of high particle densities. The concept is to track the particles through a hadron absorber system to perform a momentum-dependent muon identification. In the actual design, it contains six hadron absorber layers (carbon and ion plates) and six gaseous tracking chamber triplets. 6 layers of absorber detectors are placed downstream of the Silicon-Tracking system (STS). The tracking chambers are based on different detectors, including Gas Electron Multiplier (GEM) detectors, straw tube detectors and four layers of Transition Radiation Detector (TRD).

- Transition Radiation Detector (TRD) [23]. It aims at providing particle tracking and identification for electrons and positrons with $p > 1GeV/c$ ($\gamma \geq 1000$), and thus extend the electron identification capability of Ring Image Cherenkov (RICH) detector above momenta of $5\,\mathrm{GeV/c}$ The system will have different layouts in the two configurations, consists of four detector layers, or ten detector layers, respectively. The detectors are located approximately 4.1 to $5.9\,\mathrm{m}$ downstream of the target, i.e. between the STS and TOF wall. The TRD detectors are Xe/CO_2 based Multi-Wire Proportional Chambers (MWPC) detector, combined with radiators which are currently under considerations. The TRD detector readout will be rectangular pads with a spatial resolution of 300 to $500\,\mathrm{\mu m}$ across and 3 to $30\,\mathrm{mm}$ along the pad.

- Time-of-Flight System (TOF) [17]. It is for the hadron identification by providing the time-of-flight of the reaction products. The total area is about $120\,\mathrm{m}^2$, located at about $6\,\mathrm{m}$ to $10\,\mathrm{m}$ distance to the target. The detectors of the CBM TOF wall are timing Multi-Gap Resistive Plate Chambers (MRPC). The required time resolution is on the order of $80\,\mathrm{ps}$. Meanwhile, as the range of physical properties covers a wide range, the configuration of T_0 reference need to be adjusted accordingly. A detailed discussion will be provided in Section 2.2.

- Electromagnetic Calorimeter (ECAL) [24]. The purpose of the ECAL detector is the identification and the measurement of energy and position of photons and electrons. Each calorimeter module is a 'shashlik' type calorimeter, be composed of modules which consist of 140 layers of lead and scintillator sheets. It will be arranged in varied distances from the target.

- Projectile Spectator Detector (PSD) [25]. It provides an experimental measurement of a heavy-ion collision centrality and orientation of its symmetry plane. It is placed in the most downstream position. The PSD is a compensating lead-scintillator calorimeter, with 44 individual modules, each containing 60 lead/scintillator layers. The detector is designed to measure the number of non-interacting nucleons from a projectile nucleus in nucleus-nucleus collisions.

All the detectors in CBM are designed for high rate capabilities and high radiation hardness.

2.2 Time-of-Flight system in CBM

The Time-of-Flight (TOF) system is one of the most important detectors in CBM, which is applied in both two setup options.

To meet the requirements of TOF, the typical time resolution of a single channel should not exceed 60 ps, meanwhile the detection efficiency should be at least 95%, and the active area should be 120 m^2. At present, the system of Multi-gap Timing Resistive-Plate Chambers (MRPC) detectors is considered the only possible solution that can meet the requirements with affordable costs. Since RPC detector technology has found applications successfully in the high energy experiments such as ALICE and ATLAS in LHC, the TOF system in CBM also uses RPC as detectors.

2.2.1 Particle identification

Particle identification requires the combination of different detection methods [26, 27]. When a high energy particle is emitted or generated as the product of a collision, it goes through different detectors. The identification process can be described in the following way:

The momentum p is measured by the bending of the track R in a specific defined field with

$$p \sim \frac{R}{z} \,, \tag{2.1}$$

where z is the charge of the particle, a known value of the particle for identification; and R is the radius reconstructed from track. A particle with rest mass m_0 and momentum p has the relativistic velocity:

$$\beta = \frac{p}{\sqrt{p^2 + m_0^2}} \,, \tag{2.2}$$

where $\beta = v/c$ is the particle velocity normalized to the velocity of light in vacuum. For a path length of L, the time T is given by:

$$T = \frac{L}{v} = \frac{L}{c\beta} \,. \tag{2.3}$$

Then, two particles with different masses but the same momentum will have a difference in time of flight within the distance L:

$$\triangle T = T_1 - T_2 = \frac{L}{c} \left(\sqrt{1 + \frac{m_1^2}{p^2}} - \sqrt{1 + \frac{m_2^2}{p^2}} \right) \approx (m_1^2 - m_2^2) \frac{L}{2c\,p^2} \,, \tag{2.4}$$

where $\triangle T$ is the difference of time, m_1 and m_2 are the rest mass of the two particles, respectively. If the time resolution of the detector is σ_T, then the separation power n_σ can be given by:

$$n_\sigma = \frac{\triangle T}{\sigma_T} \ .$$

(2.5)

The separation power is determined by the mass of particles, the momenta of the particles, the length of flight paths and the time resolution of detector. A figure that represents the dependence of the separation power as a function of momentum, time resolution and track length is shown in Figure 2.5.
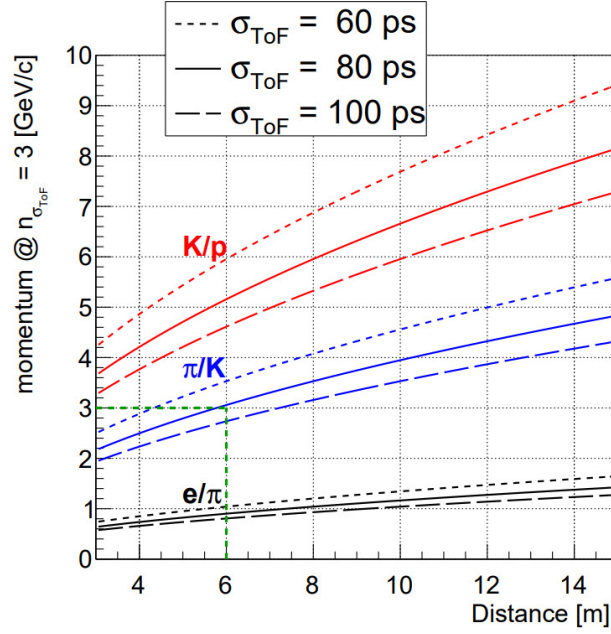
Figure 2.5: Dependence of separation power of TOF system as a function of momentum for different time resolutions (60, 80 and 100 ps) and the particle combinations of e/π, π/K and K/p. Figure is taken from [17].

2.2.2   Layout of CBM TOF WALL

The TOF wall is planned to cover the polar emission angles between 2.5 and 25 degrees and an area of about $120\,\mathrm{m}^2$. It will be placed between 6 and 10 m from the target depending on different experimental objectives. To distinguish kaons, pions and protons well, the required full time resolution including the start time T_0 is in the order of 80 ps [17].

In order to accumulate enough statistics of rare probes, the CBM detector has to run at ion beam intensities up to $1 \times 10^9\,\mathrm{Hz}$, resulting in a target interaction rate of about 10 MHz. A simulation of the distribution of particle flux [28] is presented in Figure 2.6. According to the simulation, the flux varies approximately two orders of magnitude depending on the position of the TOF wall. The maximum flux is around the center of TOF wall, around 1×10^6 particles/$(\mathrm{s} \cdot \mathrm{cm}^2)$.

Because of the high requirements for time resolution and flux capability, a system of Multi-gap Timing Resistive-Plate Chambers (MRPC)[1] with sub-millimeter narrow gas gaps are considered the only possible solution that satisfies the requirements at affordable costs.

---

[1]'Multi-gap Resistive Plate Chamber (MRPC)' is the standard name for this type of detector. In this thesis, except for the background introduction, the name 'timing RPC', is used more often than the name 'MRPC', due to two reasons: timing RPC is a name comparable to trigger RPC; and the RPC sample for experiment is single gap structure. In general, 'MRPC' and 'timing RPC' is equivalent.
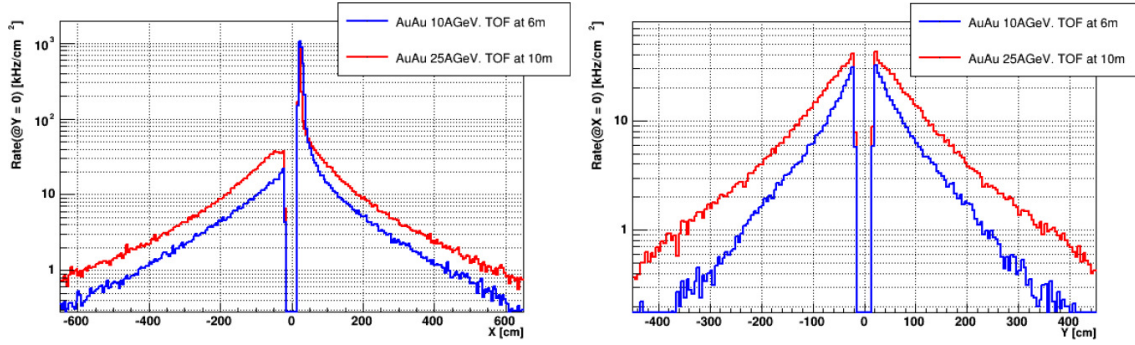
Figure 2.6: The calculation result of rate distribution on CBM TOF wall placed at 10 m (red) and 6 m (blue) behind the target, respectively. The rate includes the contribution of secondary particles produced in the upstream material of CBM. The left figure shows the flux distribution at $Y = 0$ in the horizontal direction, and the right figure is for $X = 0$ in the vertical direction. The figure is taken from [28].

Resistive Plate Chambers (RPC) is a kind of gaseous detector that is widely applied in high energy physics; a detailed introduction will be presented in Chapter 3. The CBM TOF wall consists of 1376 MRPCs, with five different kinds of different shapes, materials and designs. The active area is ranged from $300\,\text{mm} \times 100\,\text{mm}$ to $320\,\text{mm} \times 530\,\text{mm}$. Considering the flux distribution on the CBM TOF wall shown in Figure 2.6, the region where the rate is below $1\,\text{kHz/cm}^2$ will be composed of MRPCs with float glass electrodes, while in the region where the rate is between $1\,\text{kHz/cm}^2$ to $30\,\text{kHz/cm}^2$, low resistivity glass electrodes will be used. The CBM TOF is shown in Figure 2.7.

2.2.3 T_0 reference provided by the Beam Fragmentation T_0 Counter.

The start time T_0 reference is required for the measurement of TOF, where

$$TOF = T_{measurement} - T_0.$$

The TOF system will be applied for different experiments, where the physical properties and irradiation environment covers a very wide range. For the reference time, there is no single configuration that can be applied in all the situations. Instead, different solutions are pointed out.

The time resolution for the full TOF system is required to be better than 80 ps. If the time resolution of the modules of the TOF wall is 60 ps, the required time resolution of the T_0 reference time is 50 ps. As a reference, it is also required that the detection efficiency is 100%. The methods towards different running conditions are:

- Using the in-beam starting detector (SD). It is for the experiments with low beam rates and calibrations. SD will be installed inside the beam pipe in vacuum and provide the arrival time of every beam particle. For the CBM, the solution is considered an in-beam diamond SD [29].

- Reconstruction by software. This method use the multiplicity of registered particles to reconstruct the time reference from the fastest hits in TOF wall. It can be applied for
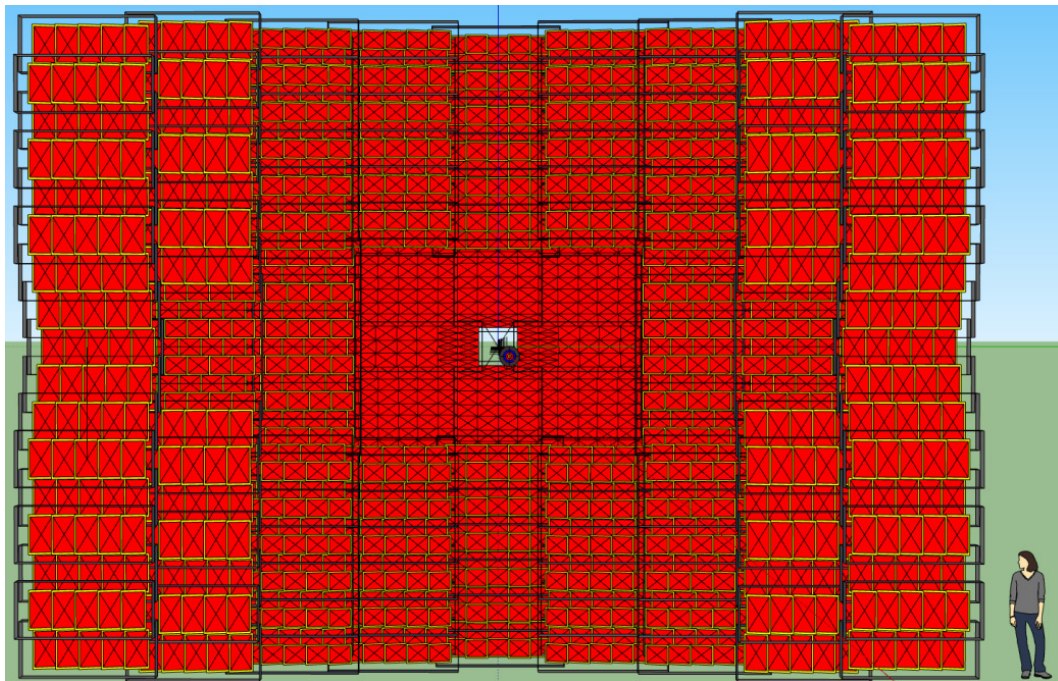
Figure 2.7: Front view of the CBM TOF wall. It is 9 m height, 13.5 m width, the active is about 120 m^2. It contains 1376 modules. Each module is a independent units that contains several MRPC detectors. The modules are drawn in red color with black cross. The size of MRPC detectors ranges from 300 mm × 100 mm to 320 mm × 530 mm; the materials are float glass or low resistivity glass depending on the estimated flux on the position of the respective RPC module. Figure is taken from [17].

particles generated from central collisions. This method is independent from the particle rate.

- Using a high resolution T_0 counter composed of an array of high rate timing RPCs in the fragmentation region. The Beam Fragmentation T_0 Counter (BFTC) is applied for high-rate semi-central reactions.

- For the extraction of a time reference signal in high rate proton-induced reactions, the development of a reaction detector outside the CBM spectrometer acceptance in the angular region of 35 deg to 65 deg is considered.

In the concept design, the BFTC consists of single cell MRPCs with ceramics electrodes [30] of dimension of 20 mm × 20 mm. The requirements in this region is high rate capability and radiation hardness. The BFTC will be placed close to the reaction point, the distance is between 25 cm and 50 cm. A schematic drawing is shown in Figure 2.8.
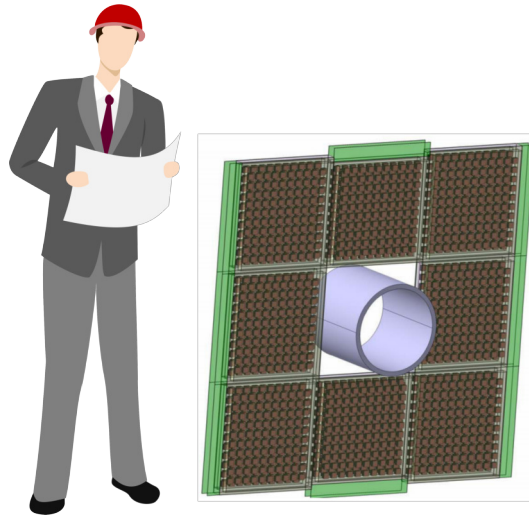
Figure 2.8: Conceptional design of CBM BFTC with high rate capability, radiation hard RPCs. The area of the BFTC is 120 cm × 120 cm. The RPCs are assembled with low resistivity ceramic electrodes of 20 mm × 20 mm. Figure is reproduced from a figure in [17].

Chapter 3

The Resistive Plate Chambers

The Resistive Plate Chamber (RPC) detectors have found applications in the field of high energy physics and other fields as well.

The technology has been developed since nearly 30 years ago. In the past decades, different kinds of RPCs are developed for various fields, especially the high energy physics and the Astroparticle physics. Nowadays, in the field of high energy physics, the development of RPC technology is highly related to the ongoing CBM experiment.

The purpose of this chapter is to present a detailed discussion of the RPC technology that are related to high energy physics. Both experimental knowledges and physical understandings will be presented. For experimental discussions, methods for testing the performances of RPC detectors will be introduced; for the physical part, the discussions will be devoted into current understanding of physical models and parameters, and how they determine the performance of RPC detectors.

As the physical model of RPC has achieved great success in exploring the RPC performance, we shall also find that there is a possibility to extend the researches of fundamentals of RPC. This possibility has led to our objective in this thesis, which will be presented in Section 3.4.

In addition, a discussion about how the fundamental research in this thesis can contribute to a challenge in the application of RPC: finding eco-friendly solution, will be presented.

3.1   Introduction to RPC

3.1.1   Overview

RPC technology was developed in the 1980s by Santonico and Cardarelli [1, 31]. After more than 20 years of research and development, it has been used in many of the high energy physics experiments such as ATLAS, CMS, ALICE at LHC, CERN. The RPC is generally used in Time-of-Flight (TOF) systems or trigger systems, providing the timing information. It also has some other fields of applications as well, such as position determination of particles, etc.

RPC is a kind of gaseous detector. A schematic drawing of the simplest RPC configuration is shown in Figure 3.1. A RPC consists of two electrodes made from material with bulk resistivity of around 10^9 to 10^{13} Ωcm. The gap between the two plates is filled with working gas. The outer

(i) Signal is readout from the conductive layer.

(ii) Signal pickup electrodes are seperated from high voltage.
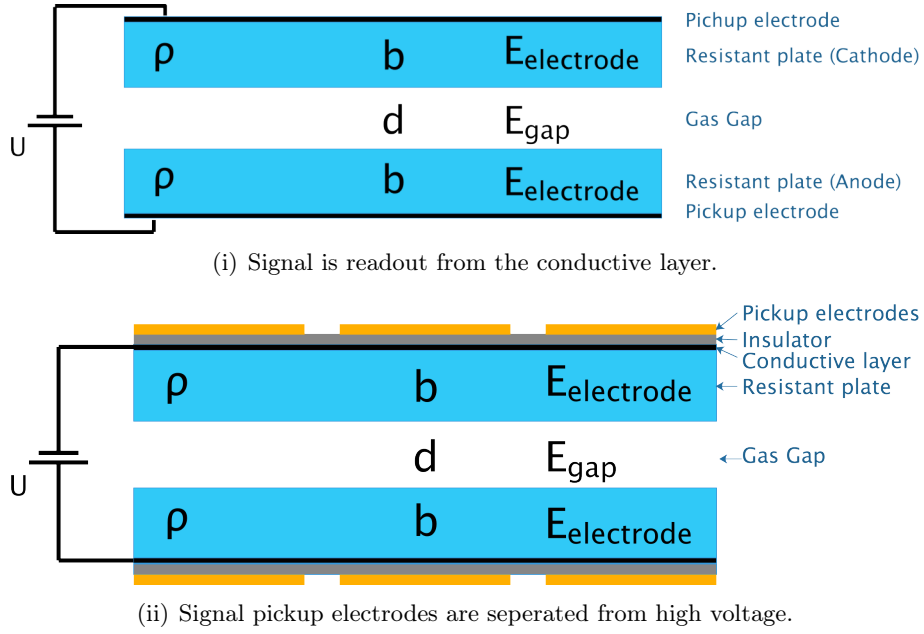
Figure 3.1: Schematic drawing of RPC with two signal read-out concepts. b and d are the thickness of electrodes and gap width respectively, ρ is the resistivity of electrodes. The field strength inside the electrode and inside the gas gap are $E_{electrode}$ and E_{gap}, respectively.

sides of the electrodes are covered by a conductive layer and are connected to a high voltage supply.

By applying high voltage on the conductive layer of electrodes, homogeneous high electric field is generated within the gas gap. The working voltage of electric field in the gas gap can be up to $50\,\mathrm{kV/cm}$ or $100\,\mathrm{kV/cm}$ depending on different uses of RPC detector.

In the geometry shown in Figure 3.1(i), the conductive layer is made of high conductive material such as metal. A signal splitter box is used to separate the signal from the high voltage potential. For the geometry shown in Figure 3.1(ii), the conductive layer is usually made from carbon paint. The bulk resistivity of the electrodes is beyond $10^9\,\Omega\mathrm{cm}$, while the conductive layer is in the order of around 10^6 to $10^7\,\Omega\mathrm{cm}$. The bulk resistivity of conductive layer is much smaller than the resistive layer, but much larger than the signal pick-up electrodes made from metal. As a result, on the time scale of a fast signal, the charge will only be induced on the signal pick-up electrodes. The two different geometries are equivalent for the physics processes within the gas gap.

As shown in Figure 3.2, when charged particles pass through the gas gap, primary ionizations may occur on the gas molecules. By ionization, free electrons and ions are produced in the gas gap, then drift to different electrodes in the high electric field.

The electrons gain energy while drifting in the electric field until they are accelerated to the energy for ionization. As the same amplification process on the secondary electrons continue, thereby an electron avalanche[1] or streamer[2] will be formed in the gas gap. As the ions are much heavier than electrons, the drift of ions will not influence the fast signal peak from the electrons. With the directional drift and amplification of electrons in an avalanche, a signal is induced on

---

[1] An electron gains energy in electric field, then ionize gas molecules and generate secondary electrons. If the process continues and more and more particles are ionized, an avalanche is formed.

[2] An streamer signal is generally a spark signal. In RPC detectors, streamers are likely developed from avalanches, and the charge of streamer signal is much lager than avalanche signal, and the performance of timing is worse.

the pick-up electrodes and recorded by electronic systems.
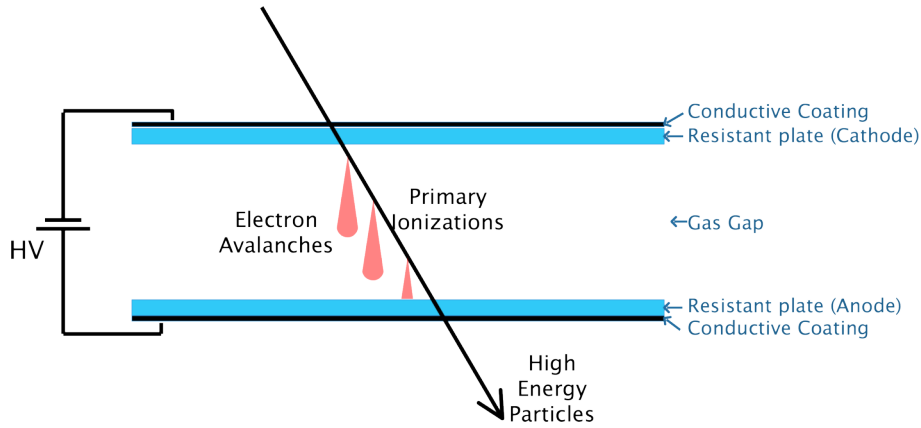
Figure 3.2: Schematic drawing of avalanches in RPC. A high energy charged
particle passes through the gas gap of RPC, and the working gas
inside RPC detector is ionized. The electrons gain energy from
the electric field of RPC and ionize gas molecules. An electron
avalanche is produced by the process of continuous ionization.

3.1.1.1 Main characteristics of RPC

The wide use of RPC technology is mainly due to its characteristics. In general, some of the
main advantages of RPC detectors are listed as follows:

- **High time resolution.** Because of the very high electric field and the short drift length,
  the response to a charged particle and the development of signal is very fast. As a result,
  the time resolution of RPCs is good. Measuring the time resolution is a basic process for
  performance investigation of RPC detectors, the results are usually in the order of nanosec-
  onds for trigger RPCs and sub-hundred picoseconds for timing RPCs. (The description of
  two kinds of RPC is presented in Section 3.1.2.2.)

- **Limited charge and streamer ratio.** The resistance of electrode would prevent the
  development of large signals and streamers. It increases the rate capability and prevent
  ageing effect of the RPC detectors.

- **High detection efficiency.** The efficiency of a RPC is also very high due to the very
  high amplification.

- **High rate capability.** By using lower resistivity material as electrodes, the rate capability
  is in the order of $10 \times 10^5 \, \mathrm{cm^{-2} s^{-1}}$

- **Easy construction..** The mechanical structure of a RPC detector is not complicated, the
  shapes of components of RPCs are regular, and the assemble process of RPC only requires
  clean environment. Due to these properties, RPC is suited for high quality repetitive
  construction.

- **Large area and low thickness.** The size of RPC can be designed according to require-
  ments. Also because the low thickness perpendicular to the direction of particle track,
  RPC can be arranged in different ways such as a wall or surrounding a volume without
  too much occupation of space.

- **Cost saving.** All the above mentioned properties and the simple electronics readout system, have made RPCs very cost saving. In particular when the material of electrodes is float glass or Bakelite. In the case of low resistivity glass or ceramic, although the cost is higher as compared to RPCs with float glass or Bakelite electrodes, it is still a more acceptable option compared to other technologies.

3.1.1.2 Applications of RPC

RPCs have been used in many different physical experiments such as ARGO-YBJ [32], BES III [33], STAR [34], etc. Especially, the use of RPC detectors in the LHC experiments: ATLAS [35], ALICE [36] and CMS [37] has shown that RPC technology is capable to satisfy some extreme performance requirements. As the thesis is devoted to RPC developments for CBM, the comparable RPCs are ATLAS, CMS, ALICE in LHC. All the three experiments use trigger RPC for the muon detection system. Meanwhile, the ALICE experiment also uses timing RPC in the TOF system. The description of two kinds of RPC is presented in Section 3.1.2.2.

3.1.1.2.1 ATLAS RPC   The ATLAS RPC [35] is used in the muon spectrometer. The muon chamber contains totally 596 RPC detectors covering an area of $3650\,m^2$. For each single RPC module, the electrodes are made from $2\,mm$ thick Bakelite. The gap width of the RPC module is $2\,mm$. The gas mixture is 94.7% Freon + 5% iso-Butane + 0.3% SF_6, the field strength within the gas gap is $45\,kV/cm$. Many tests have shown the great stability and reliability of the ATLAS RPC. In the test, the time resolution of the RPC is in the order of nanoseconds.

3.1.1.2.2 CMS RPC   The CMS RPC [37] is designed for the muon system as well. CMS uses double-gap RPCs in order to increase the efficiency. The system contains 612 different kinds of RPC covering an area of about $3000\,m^2$ [38]. The material of the electrodes is $2\,mm$ thick Bakelite, gap width of the RPC is $2\,mm$. The gas is 95.2% Freon + 4.5% iso-Butane + 0.3% SF_6. The field strength in the gas gap is 47 to $49\,kV/cm$.

3.1.1.2.3 ALICE RPC   The ALICE experiment contains two different kinds of RPC [36]: the trigger RPC and the TOF MRPC. The trigger system consists of 72 RPC modules and covers an area of $140\,m^2$. The gap width is $2\,mm$. The gas mixture is 89.7% Freon + 10% iso-butane + 0.3% SF_6, and the field strength is 50 to $51\,kV/cm$.

The TOF system contains 1638 modules in total, covering the area of $160\,m^2$. Each module contains 10 gas gaps. The electrodes are made from float glass, the gap width is $250\,\mu m$. The gas mixture is 90% Freon + 5% iso-butane + 5% SF_6, and the field strength is 92 to $108\,kV/cm$. The efficiency is beyond 95%.

3.1.2 Different kinds of RPC detector

RPC detectors can be distinguished by several different types. The first classification is about the signal process, where streamer RPCs and avalanche RPCs are distinguished. In most works related to RPC physics, the streamer RPC is usually not concerned as the focus because of the

limitation of rate capability. In this thesis, the discussions of detector physics are concentrated on avalanche RPCs as well.

Thereafter, the avalanche RPCs can be further subdivided into two main types: trigger RPCs and timing RPCs. In the research of this thesis, the experimental devices are designed for possibility to work as either trigger RPCs and timing RPCs.

Understanding the difference of trigger RPCs and timing RPCs is very important for the investigations of the experimental results. A detailed discussion is provided in Section 8.

3.1.2.1   From streamer mode to avalanche mode

The development of RPC is not only the investigation of existing results and improvement of design. There are breakthroughs that have brought new RPC technology, for example the development from streamer RPC to avalanche RPC.

In the early researches and applications, RPCs are operated in streamer mode [1]. Streamer signals are very large and can simplify the signal readout electronics. The streamer RPCs are applied in the experiments where the requirements of rate capability is up to several Hz/cm^2.

The investigations of transitions from electron avalanche to streamer, and the application of electronegative gas components, have resulted in the developments of the methods to operate RPC detector in avalanche mode [39, 40]. Compared to streamer mode, there are more critical requirements of the gas mixture in the detector, as the amplification of number of electrons should be limited, to avoid development of streamer signals.

The appearance of avalanche RPC has brought the possibilities for RPC detectors in many aspects, by greatly improving the possible rate capability and time resolution. Currently, most RPCs applied in experiments are avalanche RPCs due to its advantages; and streamer RPCs are used in some specific conditions.

Recent researches on RPC detectors are focused on avalanche RPC, as avalanche RPC has higher rate capacity and is widely used in trigger system and Time-of-Flight system. The work related to this thesis is also a research about the gas parameters measured in avalanche mode RPC.

3.1.2.2   From trigger RPC to timing RPC

3.1.2.2.1   Comparison of trigger RPC and timing RPC in physical view   RPCs that works in avalanche mode can be divided into two main kinds: trigger RPCs and timing RPCs.

The key difference of the two kinds of RPCs are their objectives: the trigger RPCs are designed to yield a time resolution in the scale of nanoseconds; while the timing RPCs are for time resolution much better than the scale. The typical time resolution of timing RPC is sub-hundred picoseconds.

The difference in objectives has brought differences in nearly every main aspects:

- **Structure.**

  Trigger RPCs are usually single-gap with width of several mm, in order to ensure the

detection efficiency[3] and a sufficient charge of signal; while for timing RPCs, the gas gap is narrow and the electric field is high, to improve the time resolution. Therefore, as the gas gap is narrow, the number of gas gaps must be multiple in order to ensure the detection efficiency.

As a result, the field strength in the gas gap is usually around $50\,\mathrm{kV/cm}$ for trigger RPCs, and $100\,\mathrm{kV/cm}$ for timing RPCs.

- **Gas mixtures.**

  There are more options of gas mixtures for trigger RPCs than for timing RPCs, as the timing RPCs are operated with higher amplification. To reduce the streamer ratio in timing RPCs, the gas mixture must ensure the certain ratio of strong electronegative gas.

  In this thesis, the gas mixture for trigger RPC mode is 94.7% Freon + 5% iso-Butane + 0.3% SF_6, while for timing RPC mode is 85% Freon + 5% iso-Butane + 10% SF_6. The gas mixtures we use are typical gas mixtures for the two modes of RPC detectors, respectively.

In a realistic situation, the design and function of trigger RPC and timing RPC are so different, that one can always distinguish the difference between the two types. In this work, the situation is different: we are working with simplified RPC samples designed for representing both kinds of RPC. By changing the gap width, field strength and gas mixtures, the working mode can be switched between trigger mode and timing mode. As a conclusion, we have achieved a high flexibility for measuring the performance of RPC with the laser test facility.

3.1.2.2.2 Brief review of development from trigger RPC to timing RPC The development of timing RPC is another breakthrough in the field. At present, timing RPCs have found applications in the TOF systems of many high energy physics experiments.

Great efforts are taken for the development of timing RPC technology. From the single gap RPCs to multi-gap timing RPCs, two significant milestones are identified in the approach:

- Double stack RPC was invented, and the research result has shown that the performance is better than single gap RPC [41]. A schematic drawing of double gap RPC is shown in Figure 3.3.

- A wide gap RPC was constructed [42]. In the performance test, it is found that the charge of a signal is much larger than normal RPC, and the rate capability is limited. To limit the charge, more resistive plates are added into the gas gap to reduce the signal charge. The geometries are presented in Figure 3.4.

Finally, the multigap RPC with high electric field was designed [43, 44].

An example of timing RPC is the MRPC in ALICE experiment, shown in Figure 3.5. The alice timing RPC is designed as double stack multigap RPC [26]. each stack contains five gas gaps with the width of $250\,\mathrm{\mu m}$. In the working condition, the gas mixture is 90% Freon+5% iso-Butane+5% iso-Butane+5%SF_6. When the applied voltage is 11.5 to $13.5\,\mathrm{kV}$, the efficiency is beyond 95% and the time resolution is $50\,\mathrm{ps}$. The average charge of signal is $2\,\mathrm{pC}$. The rate capability is $1\,\mathrm{kHz/cm^2}$.

---

[3]The detection efficiency is defined as the number of detected particles divided by the total number of particles when a certain number of charged particles passes through the detector. The common value of efficiency for RPC detectors is beyond 90%, even close to 100% for minimum ionizing particles.
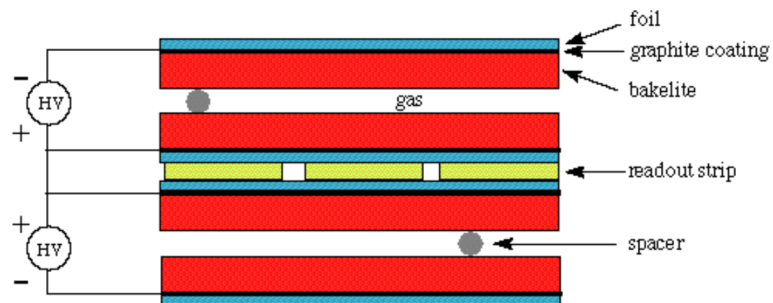
Figure 3.3: A schematic drawing of double gap RPC taken from [45]. The double gap RPC is designed from the idea that a second gas gap will increase the possibility of detection.

(i) The wide RPC.   (ii) First MRPC.
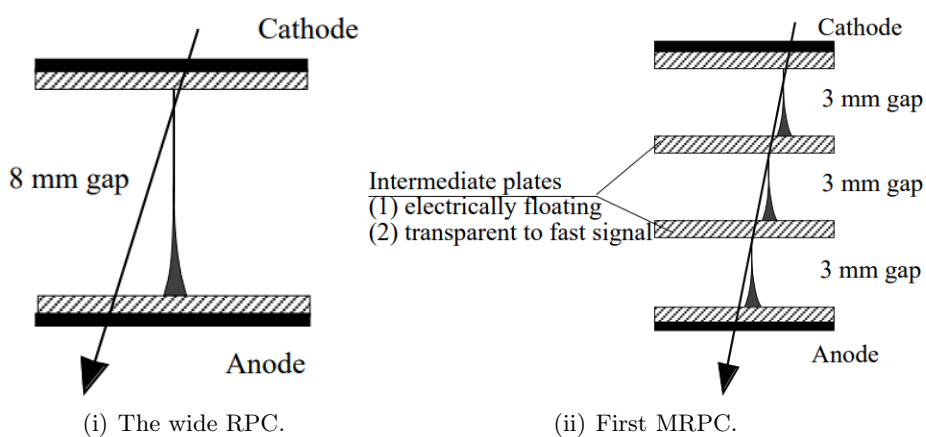
Figure 3.4: Development from RPC to MRPC [43]. A wide gap RPC was first constructed. more electrodes are assembled inside the gas gap to limit the electron avalanches.
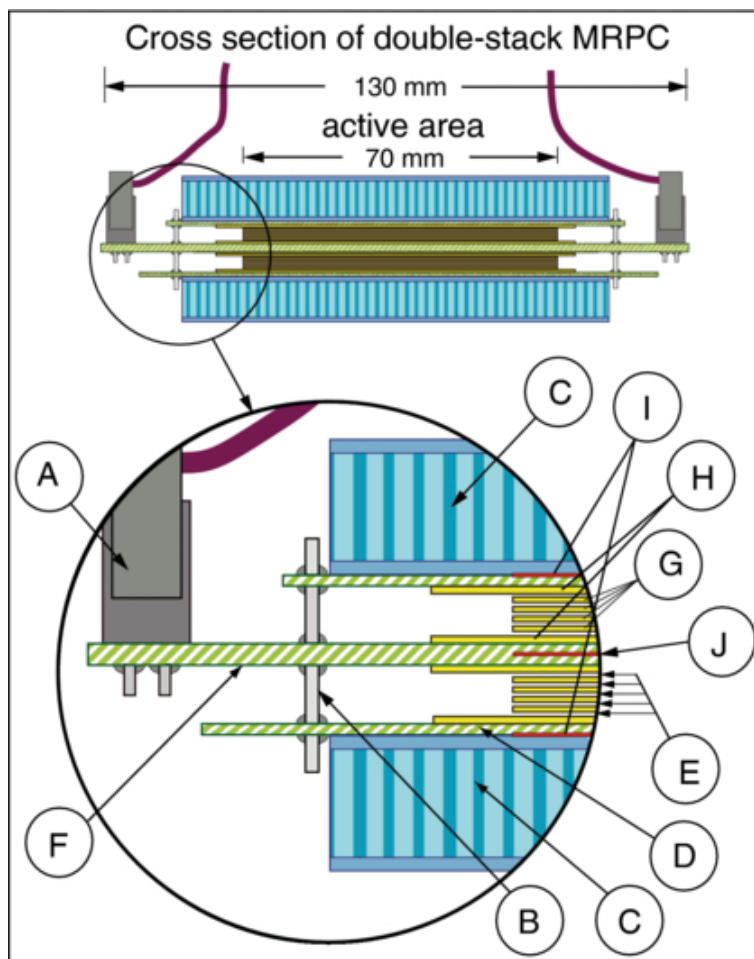
Figure 3.5: Geometry of timing MRPC used for the ALICE TOF taken from
[26]. It is a two-stack MRPC with ten 250 μm gas gaps in total.
In the working condition, the field strength inside the gas gap is
set to around 100 kV/cm. Components on the schematic drawing:
(A) cable connector; (B) pins to bring signal from the cathode to
central;(C) 1 cm thickness honeycomb; (D) PCB (Printed Circuit
Board) with cathode readout; (E) 250 μm gas gaps; (F) central
PCB; (G) 400 μm thickness glass plates (H) 550 μm thickness elec-
trodes with conductive layer outside; (I) cathode pad; (J) anode
pad.

3.1.2.3   Conclusions

The above discussions in Section 3.1.2.2 have clarified the differences of trigger RPC and timing RPC. A trigger RPC has wide gas gap(s) of about $2\,\text{mm}$ to ensure the efficiency and amplification. For achieving a higher rate capability, the field strength should be reduced so that the amplification factor is reduced. At last, the voltage is selected a value not too much above the field strength that electron avalanche begin to occur. The typical field strength for trigger RPC is $\approx 50\,\text{kV/cm}$, and σ time resolution is $\approx 1\,\text{ns}$.

For timing RPC, time resolution becomes the prior concern. Stronger field strength will yield better time resolution (will be discussed in Section 3.2), as a result, the field strength is set to a high value until limitations. Then a smaller gas gap is applied to limit the charge of the signal. However, if the gap is too small, the possibility that an primary ionization occurs in the gap becomes smaller and the efficiency is decreased, so that the number of gaps should be multiplied to guarantee a efficiency near 100%. The typical field strength for timing RPC is $\approx 100\,\text{kV/cm}$, and time resolution is sub-hundred picoseconds.

The gas parameters of both types of RPC will be measured and discussed in this thesis.

3.1.3   RPC detectors in CBM

3.1.3.1   MRPCs in the CBM TOF wall

The CBM TOF wall [17] will be constructed with 1376 MRPC modules of five different types of designs, which is introduced briefly in Section 2.2.2. The detector system is organized in a modular way: the basic components of the TOF wall are independent modules, and each module contains the MRPC detectors and associated electronics. A schematic drawing of the TOF wall that composed of modules is shown in Figure 2.7.

A list of the MRPCs used in the modules is shown in Table 3.1. According to flux distribution (Shown in figure 2.6.) over the TOF wall, the material of electrodes are chosen low resistivity glass and float glass, respectively, from center outward.

The designs of the MRPCs differ in many aspects, such as the shape, material of electrodes, voltage supply setups. As CBM is still under construction, alternative solutions with different structures of readout is also under consideration [46].

Despite a great variety of differences, the geometry of RPC, which is independent from material or shape, can be classified into only two types: two-stack type and single-stack type. The similarities in the geometries have brought simplification in the practical use of the RPCs.

Various performance studies have been carried out for the prototypes of MRPCs in CBM. In the performance tests, the efficiency and time resolution of the MRPCs have achieved the experimental requirements:

3.1.3.1.1   Float glass MRPCs: for the MRPC with float glass in the lower flux region, cosmic ray tests [47] and in-beam tests [48] have shown that the efficiency of the MRPC is beyond 98% and 95% (according to the setup of readout threshold), the time resolution is about 40 and $50\,\text{ps}$, respectively.

	MRPC1	MRPC2	MRPC3a	MRPC3b	MRPC4
Glass size [mm^2]	320×100	320×200	330×280	330×280	330×540
Active area [mm^2]	300×100	300×200	320×270	320×270	320×530
Number of gas gaps	10	10	8	8	8
Gap size [µm]	140	140	220	220	220
Glass thickness [mm]	0.7	0.7	0.7	0.5	0.5
Number of glass plates	12	12	9	9	9
Structure	2-stack	2-stack	1-stack	1-stack	1-stack
Glass type	low res.	low res.	low res.	float	float

Table 3.1: The MRPC modules in CBM experiment [17].

3.1.3.1.2 Low resistivity glass MRPCs: different prototypes of MRPCs with low resistivity glass are tested with beams from different facilities [49, 50, 51]. Despite the differences of experimental conditions and setups which can lead to a variation in performance, the acquired efficiency ranges from about 96% to 98%, and time resolution is from 40 ps to 80 ps. The results have satisfied the requirements of CBM.

3.1.3.2 RPCs for the Beam Fragmentation T_0 Counter (BFTC)

The Beam Fragmentation T_0 Counter (BFTC) will provide the information of start time of particles. As the BFTC is placed close to the beam-tube, it requirement for high rate capability in the order of $200 \, \mathrm{kHz/cm^2}$ [52]. The BFTC will cover the region of about 20 cm to 60 cm from the beam line in CBM, as shown in figure 2.8. For the detectors in the BFTC, Si_3N_4/SiC ceramic RPC [53, 30] has been chosen, due to its high performance of rate capability and radiation hardness. The area of the ceramic RPC modules will be $24 \, \mathrm{mm} \times 24 \, \mathrm{mm}$. Each module will contain three cells, and each cell has two gas gaps, as shown in Figure 3.6.

(i) RPC cell   (ii) RPC module.   (iii) A picture of the module.
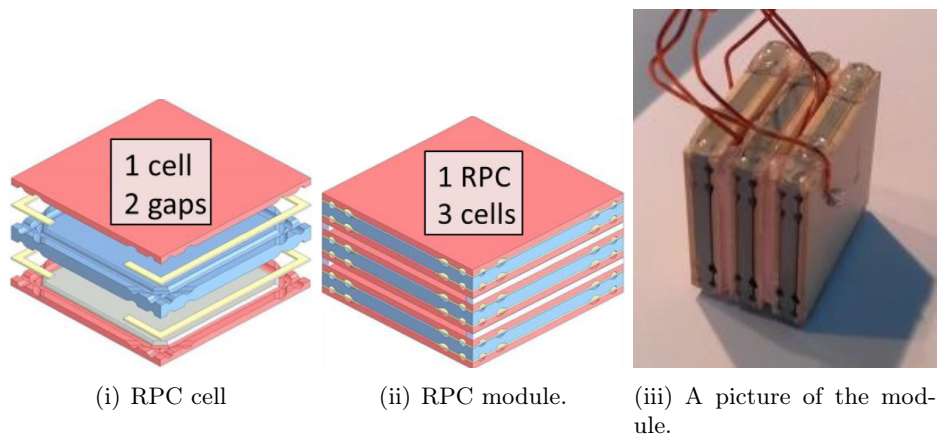
Figure 3.6: Schematic view of the ceramic RPC module for BFTC. Each RPC cell contains two gas gaps, and each module contains three cells. The BFTC wall shown in Figure 2.8 will be composted of about 4000 modules.

Performance tests have been operated for RPC prototypes with ceramic electrodes. The efficiency is beyond 98% and the time resolution is below 60 ps.

3.1.4   The challenge of eco-gas

3.1.4.1   Review of a similar issue in the past

During the early development of streamer RPCs, the experimental gas mixtures usually contained certain percentage of Argon, iso-Butane (i-C_4H_{10}) and Freon (CF_3Br, Bromotrifluoromethane): different from the currently used 'Freon'(R134a, C2H2F4, 1,1,1,2-Tetrafluorethan) in RPCs.It is found that Freon gases can reduce the size of discharges [54], meanwhile absorb UV photons to prevent streamers.

However, CF_3Br is highly harmful to the environment, and was prohibited. Afterwards, great efforts were taken into the researches for replacement of CF_3Br gas [55]. As a result, the R134a has become an option of gas mixture component.

The replacement of Freon was more than successful. Timing RPC technology was developed and applied widely, and due to the high requirements of the electronegativity and photon absorption of gas, R134a has become the main component of standard gas mixtures for timing RPC detectors [1].

At the present time, gas mixtures of RPC with R134a, SF_6 and iso-Butane is usually applied in all kinds of RPC detectors. The name 'Freon' refers to R134a in other sections of this thesis.

3.1.4.2   The issue of eco-gas at present

The common gas mixtures of timing RPCs contain Freon ($C_2H_2F_4$) and SF_6, which are greenhouse gases with the Global Warming Potential[4] (GWP) of 1430 and 23900, respectively. As the RPC technology was experiencing a very rapid development in the past years, the usage of R134a and SF_6 gas have increased. According to estimations, RPC detectors are responsible for about 80% of the total CO_2 equivalent emission of the experiments in LHC [57].

The use of gas mixtures with GWP above 150, will be restricted by EU [58]. Starting from year 2015 to year 2030, the use of fluorinated gases will be reduced to 21% compared to present amount of usage. The regulation will have a significant effect on the price and allowance of the current RPC gas that contains high ratio of R134a and SF_6.

At present, there have been efforts for recycling the gas with closed loops for reducing the gas emission in many experiments [59]. However, considering the cost and unavoidable leak of gas, recycling is only a temporary solution. The issue of timing RPC working gas therefore arises: within few years, it will become a challenge of RPC application and development.

To overcome the issue, searching for an alternative gas mixture is an important approach. Currently, a number of tests have been operated for testing the possible substitute gases. Among all the potential candidates [60], the HFO-1234ze (1,3,3,3-Tetrafluorpropen) is most promising for achieving the need for future applications [61, 62].

However, the alternative gas research is incomplete and requires more efforts. A dedicated research has shown that the time resolution of and MRPC module with eco-friendly gas is about 120 ps, which is worse than with usual gas of about 90 ps [63].

The research of alternative gas requires a fast method for measuring the gas parameters. In

---

[4]The Global Warming Potential (GWP) was developed to allow comparisons of the global warming impacts of different gases. It measures how much heat a greenhouse gas traps in the atmosphere to a specific time, relative to CO_2 [56].

(i) Double stack MRPC. (ii) Single stack MRPC.
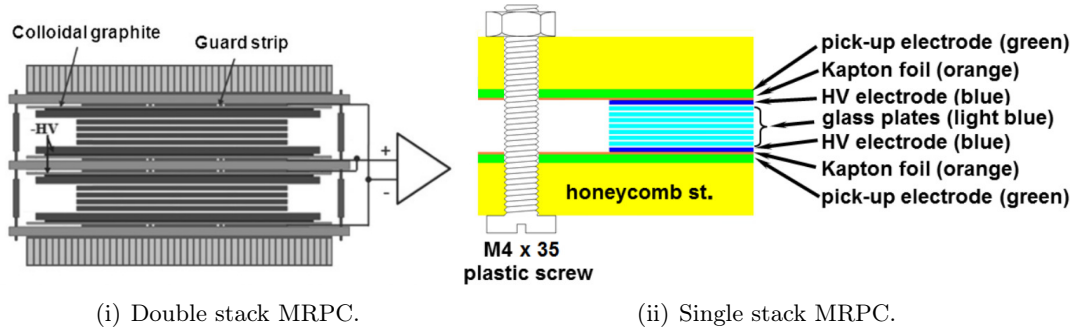
Figure 3.7: Examples of a real RPC and a simplified model. The real RPCs
are for CBM experimental designs.

this thesis, the development of methods for precise measurements of gas parameters in a realistic situation will be described. The test facility and methods will contribute to the research of future eco-friendly gas mixtures.

3.2 Characteristics and detector physics

3.2.1 Simplified model

There are many kinds of RPCs in different experiments. RPC is very flexible in some aspects, such as the readout layouts, shapes, materials and working gas. As an example of differences in shapes and materials, the MRPCs in CBM TOF [17] are shown in Figure 3.7.

However, RPCs are not flexible in other aspects: for all trigger RPCs, their gap widths and single-gap geometries are similar; for all timing RPCs, their gap width, multi-gap geometries and gas mixtures are similar. The current geometries and gas mixtures have been proved to be the most sufficient by practical experiences. As a conclusion, a simplified model of RPC can represent any kind of RPC detectors.

For understanding the detector physics of RPC, consider that there are no primary ionizations inside the gas gap. The supplied high voltage is U, and the field strength inside the electrode and inside the gas gap are $E_{electrode}$ and E_{gap}, respectively; the volume resistivity of the electrode is ρ, the resistivity of the working gas is ρ_{gas}; b is the thickness of electrodes and d is the gap width, as shown in Figure 3.1(i). Then:

$$2\,b\,E_{electrode} + d\,E_{gap} = U \ , \tag{3.1}$$

$$\frac{E_{electrode}}{\rho} = \frac{E_{gap}}{\rho_{gas}} \ . \tag{3.2}$$

Because that the resistivity of gas ρ_{gas} is much larger than resistivity of electrodes ρ, therefore:

$$E_{electrode} = 0 \ , \tag{3.3}$$

$$E_{gap} = \frac{U}{d} \ . \tag{3.4}$$

The above discussions describe the static behaviour of RPC performance.

When a high-energy charged particle travels through the gas gap of a RPC, the collisions between the high energy charged particle and the RPC working gas molecules, will result in the energy loss on the high energy particle and ionizations of the gas molecules. As the particles for detection by RPC detectors usually have much larger energy than ionization potentials of gas molecules, its energy lose inside the gas gap is negligible.

According to the simulation results in [64], it can be concluded that: for a typical RPC gas, the average number of clusters is around $10 \, \text{clusters} \cdot \text{mm}^{-1}$ and the average number of electrons per cluster is about two to three.

3.2.2 Gas parameters

The gas parameters will influence the characteristics in every aspects in a gaseous detector. The performance of RPC detectors is also determined by the gas mixture in the gas gaps.

The important gas parameters that are related to this thesis are the followings:

- **The Townsend coefficient α.** The first Townsend coefficient α is a fundamental parameter which determines the gas gain and have a direct influence on the overall performance. In a homogeneous electric field, regardless of electron attachment, if the initial number of electrons is n_0, after the drift length of x, the number of electrons becomes $n_x = n_0 \, e^{\alpha \, x}$.

- **The attachment coefficient η.** The attachment coefficient η represents the electron absorption of electronegative gas. If the initial number of electrons is n_0 and there would be no amplification in the gas, after the drift length of x, the number of electrons becomes $n_x = n_0 \, e^{-\eta \, x}$.

- **The effective Townsend coefficient α_{eff}.** It is the difference between the first Townsend coefficient α and the attachment coefficient η:

$$\alpha_{eff} = \alpha - \eta \, . \tag{3.5}$$

  For a specific RPC gas mixture, α_{eff} is the value that directly affects the RPC performance.

- **The electron drift velocity v_{drift}.** It represents the average drift velocity of electron swarms.

In our experiment, only the effective Townsend coefficient α_{eff} and electron drift velocity v_{drift} can be obtained. Both α_{eff} and v_{drift} are important parameters in the performance of RPC detectors.

In an ordinary test of RPC detectors with accelerators or cosmic ray test systems, the gas parameters cannot be measured directly because the direction of the particles in the beam of accelerators or the muons in cosmic ray will pass through the RPC detector, and the position of primary ionizations will have random distances to the electrodes. On the other hand, these parameters are important, as all the measured characteristics of a RPC detector, such as efficiency, time resolution, and charge distribution, depend on them.

The direct measurement of gas parameters of trigger RPC has been operated [5, 6]. The experimental results are in agreement with simulation results. In this thesis, the method for direct measurement of parameters of timing RPC will be presented.

Further discussions of the simulation and measurements of these gas parameters will be discussed in Section 3.3.

3.2.3 The process of detection using RPC

3.2.3.1 Primary ionization

For RPC irradiated with ionizing particles, the primary electrons are ionized along the track of particle, the number of cluster and the distance to cluster will have an influence on the time over threshold before the avalanche process. According to the calculations in Figures 3.8(i) and 3.8(ii) in [64], a very typical value of cluster per distance is $10/mm$, and 80% to 90% clusters only contains one electron. If there is a RPC or MRPC with total gap width of $1\,\mathrm{mm}$ to $2\,\mathrm{mm}$, the most probable number of primary electrons will be in the order of 10 to 100
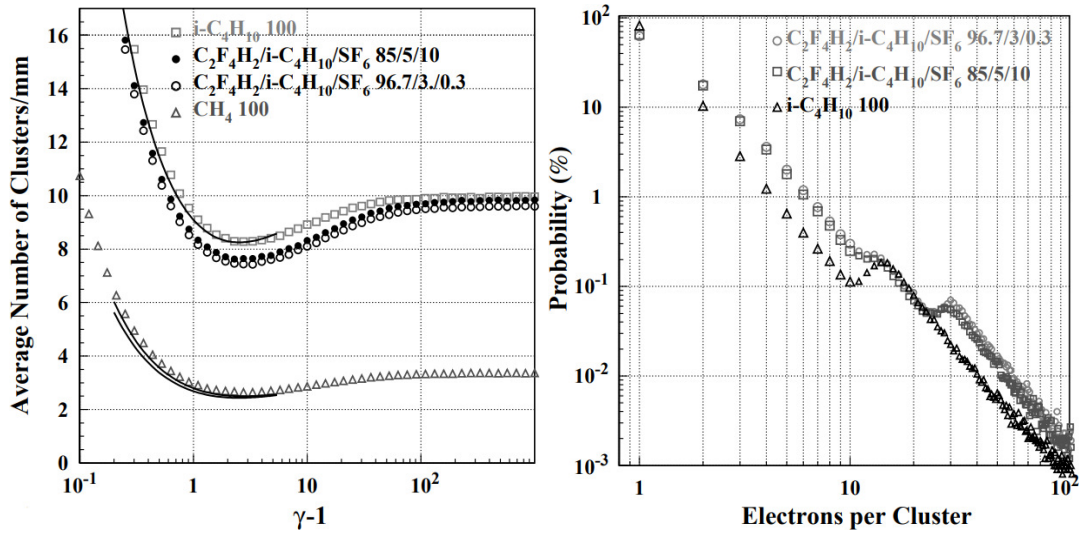
(i) The average number of clusters.   (ii) The cluster size distribution.

Figure 3.8: The average number of clusters and cluster size distribution calculated in [64].

3.2.3.2 Electron avalanches

After primary electrons are produced by ionizations in the gas gap of RPCs, the electrons will be accelerated by the strong electric field. As the accelerated electrons moves towards the anode, collisions between accelerated electrons and gas molecules will occur. If the energy of electrons exceed the ionization potential of the molecules, there is a possibility that the molecule is ionized and secondary electrons are generated. The secondary electrons are again accelerated and collides with other molecules. Therefore, an electron avalanche is formed. The minimum field strength for avalanche generation is around $40\,\mathrm{kV/cm}$ for trigger RPC gas, and around $70\,\mathrm{kV/cm}$ for timing RPC gas, as will be presented in Section 6.

Assume that the field strength is not affected by the charge of electrons and ions, the number of electrons in an avalanche follows exponential growth:

$$N_e(x) = N_0 \, e^{(\alpha - \eta) \, x} \, , \tag{3.6}$$

where x is the drift length, $N_e(x)$ is the number of electrons at the drift length of x, N_0 is the number of primary electrons, α and η are the Townsend coefficient and the attachment coefficient, respectively.

3.2.3.3   Induced charge

If the induced charge on the readout strips is $Q(x)$, then:

$$Q(x) = N_e(x) \frac{-e \, \triangle \, x_e + e \, \triangle \, x_{ion}}{d} \, , \tag{3.7}$$

where e is the unit charge of an electron, $|e| = 1.60 \times 10^{-19} C$; $\triangle x_e$ and $\triangle x_{ion}$ are the drift lengths of electrons and ions within the small time interval $\triangle t$, d is the gap width.

Consider that the ions are much heavier than electrons, during the development process of electron avalanches, we have $\triangle x_{ion} \ll \triangle x_e$, then

$$Q(x) = |N_e(x) \frac{e \, \triangle \, x_e}{d}| \, . \tag{3.8}$$

As the drift velocity v_{drift} is a constant value during the avalanche process, we find that

$$x = v_{drift} \, t \, , \tag{3.9}$$

where t is the time starting from the initial charge, then:

$$N_e(t) = N_0 \, e^{(\alpha - \eta) \, v_{drift} \, t} \, , \tag{3.10}$$

$$Q(t) = N_e(t) \frac{e \, v_{drift} \, t}{d} \, , \tag{3.11}$$

where $N_e(t)$ and $Q(t)$ are the number of electrons and the induced charge as a function of time t, respectively. If the time interval $\triangle t$ tends to dt, it can be calculated that the induced current is

$$I_{induced}(t) = \frac{d}{dt} Q(t) = N_e(t) \frac{e \, v_{drift}}{d} \tag{3.12}$$

where $N_e(t)$ is the number of electrons at time t, e is the unit charge of an electron, v_{drift} is the drift velocity, d is the gap width. Equation (3.12) is in agreement with the calculation given in [64].

If we assume that the signal starts from the cathode where the total drift length equals the gap width d, and the total duration is t_{max}, the total induced charge $Q_{induced}$ is

$$
\begin{aligned}
Q_{induced} &= \int_0^{t_{max}} I_{induced}(t)\, dt \\
&= \int_0^{t_{max}} \frac{v_{drift}}{d} e\, N_e(t)\, dt \\
&= \frac{v_{drift}\, e}{d} \int_0^{t_{max}} N_0\, e^{(\alpha-\eta)\, v_{drift}\, t}\, dt \\
&= \frac{v_{drift}\, e}{d}\, N_0\, \frac{e^{(\alpha-\eta)\, v_{drift}\, t_{max}}}{(\alpha-\eta)\, v_{drift}} \\
&= \frac{e\, N_0}{(\alpha-\eta)d}\, e^{(\alpha-\eta)l} \\
&= \frac{Q_{total}}{(\alpha-\eta)\, d}\ ,
\end{aligned}
\tag{3.13}
$$

where Q_{total} is the total charge, t_{max} is the total duration of the signal. It can be seen from Equation (3.13) that the induced charge collected on the readout system of RPC is only $1/((\alpha-\eta)d)$ of the total charge.

3.2.3.4 Charge distribution

Charge distribution of RPC detector differs by the experimental setup. The geometry of detector, gas, ionization process and electron avalanche process have very high influence on the charge distribution of a RPC or MRPC.

Despite the differences, charge distribution usually follows gamma distribution. The deviation of charge distribution highly depend on the primary number and the spatial distribution of electrons.

3.2.4 Time resolution

The time resolution is one of the most important characteristics of a RPC detector. The time resolution represents the accuracy of the measured time, when a high energy particle passes through the RPC detector. As is introduced in previous section, the time resolution of trigger RPC and timing RPC is in the order of nanoseconds and sub-hundred picoseconds, respectively. In this chapter, a discussion of the RPC time resolution will be presented.

The time resolution is defined as the statistic standard deviation of the difference between the reference time t_0 and the signal time t_{signal}. In a measurement, t_0 is provided by the reference time coming from other detectors or, from the time reference of accelerators, etc. t_{signal} is the time acquired by the data acquisition system that reads the signal from RPC. The corresponding time of signal T is defined as:

$$
T = t_{signal} - t_0\ .
\tag{3.14}
$$

A large number of T data is acquired during an experiment. The data is put into a histogram, then fitted by Gaussian distribution to acquire the sigma time distribution σ_t According to the calculation of [64], the time resolution of a RPC detector is given by:

$$\sigma = \frac{1.28}{(\alpha - \eta)\, v_{drift}} = \frac{1.28}{\alpha_{eff}\, v_{drift}} \ , \qquad\qquad (3.15)$$

where α is the first Townsend coefficient, η is the attachment coefficient, α_{eff} is the effective Townsend coefficient, v_{drift} is the electron drift velocity.

However, this formula is based on the assumption concluded from experimental data that the amplitude of signal follows a function similar to gamma function, which is different from the case of primary electrons by laser ionization. The time resolution obtained from laser test system should be better than predicted in Equation (3.15). A detailed discussion will be provided in Section 8.1.1.

3.2.5   Rate capability

3.2.5.1   Experimental understandings about rate capability

The material of electrodes is of high importance for the rate capability of RPCs. The float glass and Bakelite material was first used for RPC detectors. For the application in high rate experiments, RPCs with low resistivity float glass electrodes, and low resistive ceramic electrodes, are assembled.

It is generally accepted that the rate capability depends mainly on the resistivity of the RPC electrodes. Using an electrode with low bulk resistivity will increase the rate capability. An example of dependence of rate capability on the material of electrodes is shown in Figure 3.9.

3.2.5.2   Field reduction process

Consider an avalanche signal inside the timing RPC gas gap, the process of reducing the field strength and recharge of signal happens in different time scales. The avalanche and signal process develop in three different time scales [3] considering the RPC geometry shown in Figure 3.1(ii). In the situation of the HZDR laser test facility, however, as the geometry of RPC is similar to Figure 3.1(i), the process can be simplified into two time scales:

- **Fast signal process.** The avalanche happens within 1 to 10 ns, in such small time scale, the electrodes are transparent to electric field. The avalanche is started, developed, and ended within the time scale. In the end, the electrons and ions are collected on the anode and cathode surface. Shown in Figure 3.10.

- **Slow field recovery.** Charge on the electrodes from electrons and ions will reduce the field strength on the position of the previous avalanche. After a recovery time related to the time constant of RPC, the field strength will be fully recovered if there is no other ionization in this volume. If the next ionization comes when the field strength is not fully recovered, the signal will be smaller than expected, as the field is reduced.
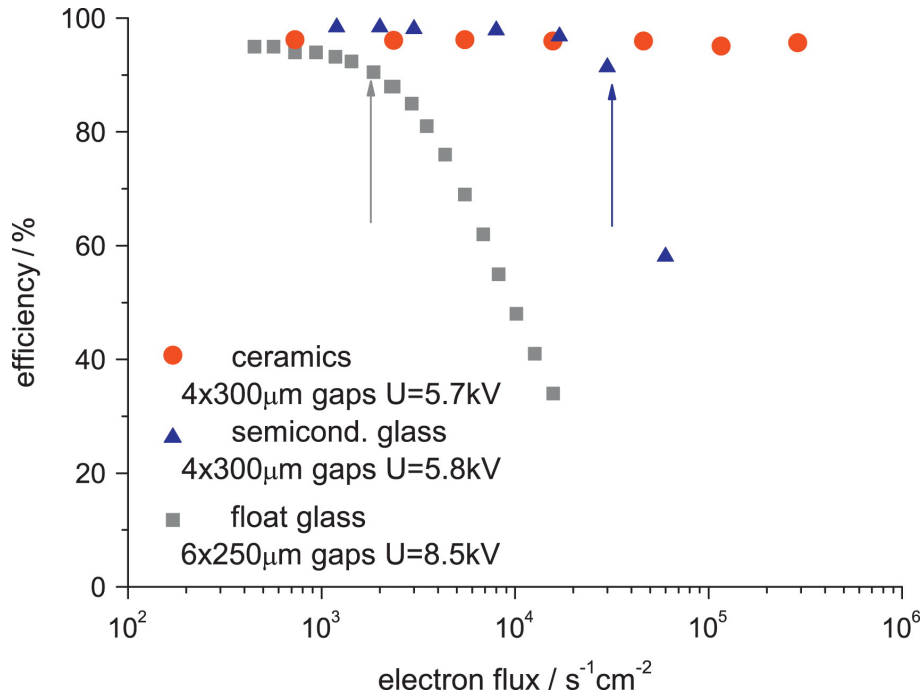
Figure 3.9: Efficiency as a function of flux tested with RPCs with different materials taken from [30]. The resistance of the three materials are: $\rho_{floatglass} > \rho_{semiconductiveglass} > \rho_{ceramics}$. From this figure, it can be seen that the rate capability is increased when a material with low volume resistivity is used for the electrodes. The arrows represent the rate capability of a certain RPC module.

The RPCs presented in this figure are originally designed for specific uses respectively, so that the geometries and materials are different. It may confuse the reader that why RPCs with different designs can be put into comparison. This is because: according to experimental facts, the performance of a RPC mainly depends on the volume resistivity of electrode material, and has low dependence on other parameters. Although the three RPC geometries are very different, when the rate capability is concerned, only the volume resistivity is of highest dependence.

(i) The avalanche is developing.

(ii) The avalanche develops to the maximum value. Ions keep drifting.

(iii) The avalanche is ended, electrons and ions are on the surface of electrodes.
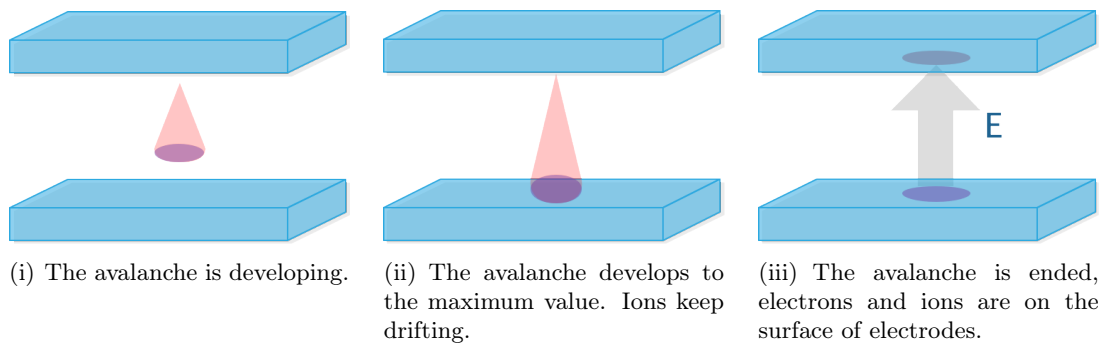
Figure 3.10: The development of electron avalanche and the reduction of electric field.

3.2.5.3   The time constant

Consider our RPC shown in Figure 3.11(i), the gap width is d and the thickness of electrodes is b, the volume resistivity of electrode is ρ. To determine the the time constant of a RPC detector, there are two different ways to consider the time constant of a signal.

(i) A schematic drawing of RPC to calculate the time constant.

(ii) The time constant of detector without considering the volume outside the signal area.

(iii) The time constant of signal if considered as point charge on the surface of electrode
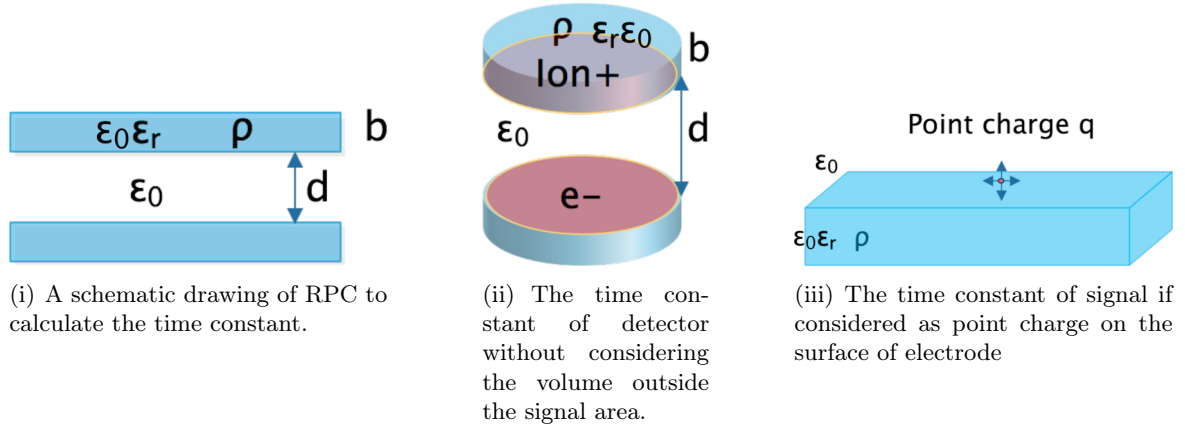
Figure 3.11: The determination of time constant.

In the first way, consider that the signal is evenly distributed in an area S, and the distribution area of signal is large or S is small, then assume that the recharge only comes from cylindrical volume of electrodes under or above the area S (Figure 3.11(ii)). In this way, the time constant will be the same as the RC time constant of the detector as a capacitor. Then the time constant τ in this situation is:

$$\tau_1 = R\,C = 2\rho\,\frac{b}{s}\left(\frac{2\,\varepsilon_0\,\varepsilon_r\,S}{b} + \frac{\varepsilon_0}{d}\right) = 2\rho\,\varepsilon_0\left(2\,\varepsilon_r + \frac{b}{d}\right), \qquad (3.16)$$

where ε_r is the relative permittivity, ε_0 is the absolute permittivity, ρ is the volume resistivity. The time constant τ is then:

$$\tau_1 = 4\,\rho\,\varepsilon_0\,\varepsilon_r + 2\,\rho\,\varepsilon_0\,\frac{b}{d}\,. \qquad (3.17)$$

In the second condition, consider that the charge is a point charge on the surface of the electrode. Consider the electric strength $E(r)$ on the distance r from the point charge, the flux on the upper medium(gas) or lower medium(electrode) from the sphere surface surrounding the point charge is then:

$$2\pi r^2\,E\,. \qquad (3.18)$$

Consider the point charge in the center q, then:

$$q = \varepsilon_0\,\phi_{upper} + \varepsilon_r\,\phi_{lower}\,, \qquad (3.19)$$

so the field strength at position $E(r)$ is:

$$E(r) = \frac{q}{2\,\pi\,(\varepsilon_0 + \varepsilon_r)r^2}\,. \qquad (3.20)$$

The current to the charge is then:

$$I = \oint \sigma E dS = (\sigma_1 + \sigma_2) \frac{2\pi r^2}{2\pi(\varepsilon_0 + \varepsilon_r) r^2} Q = \frac{\sigma_1 + \sigma_2}{\varepsilon_0 + \varepsilon_r} Q \ , \tag{3.21}$$

where ε_0 and ε_r is the electric permittivity of the gas and electrodes respectively, and σ_1 and σ_2 is the conductivity of gas and electrodes respectively.

Knowing that:

$$\frac{dq}{dt} = I = \frac{\sigma_1 + \sigma_2}{\varepsilon_0 + \varepsilon_r} q \ , \tag{3.22}$$

then the charge on the surface q_t and the time constant τ_2 are:

$$q(t) = q_0 \, e^{-\frac{t}{\tau_2}}, \tau = \frac{\varepsilon_0 + \varepsilon_r}{\sigma_1 + \sigma_2} \ . \tag{3.23}$$

As the gas has very few conductivity, the time constant in Equation (3.23) is:

$$\tau_2 = \frac{\varepsilon_r \, \varepsilon_0}{\sigma_2} = \rho \, \varepsilon_r \, \varepsilon_0 \ , \tag{3.24}$$

where ρ is the volume resistivity and $\rho = \frac{1}{\sigma}$.

The detector time constant is $\tau_1 = 4\rho \, \varepsilon_r \varepsilon_0$, and the time constant of point charge is $\tau_2 = \rho \, \varepsilon_r \, \varepsilon_0$. In a real detector, as the charge covers an area of an avalanche, it can be concluded that the time constant τ_{real} follows:

$$\tau_2 < \tau_{real} < \tau_1 \ . \tag{3.25}$$

As they are on the same order of magnitude, it can be also roughly concluded that:

$$\tau_{real} = \rho \, \varepsilon_r \, \varepsilon_0 \ . \tag{3.26}$$

This calculation is in agreement of the calculation in [65] obtained from a different method.

3.2.5.4 Improving the rate capability

In our calculations in Equation (3.16), it has been obtained that the rate capability is determined by the time constant, the area of field reduction and the signal charge. In practical, the following methods can be found in the development of RPC.

- Reducing the resistivity of electrodes. This method reduces the time constant greatly of several order of magnitude, such as using a low resistivity material to build the electrode [30, 66, 67, 68].

- Reduce the gap width. This will limit the charge and size of avalanche. Although it increases the time constant, as the capacity is higher and the signal is limited, the reduction of gap width increases the rate capability greatly. We can consider MRPC as a kind of RPC with narrower gas gap.

- Changing the parameters of material, for example by heating. If the temperature is changed, the parameters of electrodes will also be changed. It is observed that heating the electrodes improves the rate capability of RPC, the change is usually within one order of magnitude [69, 70].

Although increasing the gap width will also make the time constant smaller, signal size will also be increased and as the capacitance of detector becomes smaller, the field is easier to recover and easier to reduce.

3.2.6   Streamers in avalanche mode

As is introduced in Section 3.1.2.1, streamer mode RPCs are developed first. As the streamers contain a large number of electrons, the rate capability for streamer RPC is limited. Also, as a streamer process contains the contribution of sencondary photons [40], the performance of time resolution is worse compared with avalanche process.

An avalanche signal in usually has signal charge of about several pC (after amplification) and pulse length in the order of around 10 ns. As a comparison, a streamer signal has charge in the order of several hundred pC (after amplification), resulting in a lower rate capability.

However, streamers still occurs in avalanche mode RPCs. The streamer ratio is the percentage of streamer signals within a certain amount of signals. A typical value of streamer ratio is below 10%. The streamer ratio is an important performance parameter for an avalanche RPC detector, as streamer signals reduce the performance of RPC. In order to limit the streamer ratio, SF_6 is added into the gas mixture due to its strong electronegativity [71].

3.3   Understanding of gas parameters

The aim of this section is to provide a discussion to explain the connection between the measurement of gas parameters in reduced field and in atmospheric pressure.

3.3.1   The basic principles to measure gas parameters in reduced fields

The gas parameters play a very important role in the performance of a RPC. The gas parameters are usually measured in reduced fields and pressured, to avoid extreme signals, streamers, and space charge effect.

The Townsend coefficient for the same gas in different pressures and electric fields, can be determined by the equation [72]:

$$\alpha_{eff}/p = A\,e^{-B/(E/p)} \,, \tag{3.27}$$

where p is the gas pressure, E is the electric field strength, A is a parameter related to the saturation ionization in the gas at a certain E/p, B is a parameter related to excitation and ionization energies of gas molecules. A and B are usually determined in experimental research.

Equation (3.27) is the basic principle of the experimental studies of gas parameters in a reduced pressure and electric field. The experimental results will be introduced in Section 4.2.2. This equation is also connected to Paschen's law about electron breakdown. A brief discussion of the connection between the two equations will be given in Appendix A.

With the assumption that Paschen's law and Equation (3.27) are valid, the gas parameters related to RPCs are measured with reduced field strength and reduced gas pressure, as the breakdown voltage U_b depends on the product of the gas pressure p and gap width d, then the breakdown voltage should be the same when p is reduced but pd is fixed.

3.3.2 Compared to real RPC: agreements and disagreement

As RPCs are working at atmospheric pressure, the direct test of gas parameters in realistic situation is also necessary. The comparison of parameters measured from trigger RPC at atmospheric pressure, and the simulation results from Monte Carlo tool Magboltz which implements the gas parameters measured at reduced electric field and reduced pressure, has shown agreement in experiments [5, 6] and our results (presented in Section 6.1). The comparison which will be further discussed in Section 4.2.3.

However, there are no systematic measurement results of timing RPCs as far as we know. The measurement of gas parameters of timing RPC at atmospheric pressure is difficult, not only because of the risks of damaging the devices, but also because of the very high amplification of up to approximately $100\,\mathrm{mm}^{-1}$ [64], so that the requirements in experimental precision are high.

Despite the success in the agreement of trigger RPC, there is a gap between simulations and experimental results for timing RPCs: according to the experimental results in reduced fields and simulations of Magboltz, the total charge obtained from experiment is much smaller than the simulation value [73, 64]. For the trigger RPC, the difference is only a factor of five, while for the timing RPC the difference is in the order of 10^5.

It is assumed that there is a strong space charge effect. Space charge effect occurs when the number of electrons and ions in an avalanche is very large, and the field strength is influence by the additional electric field. There are multiple models to estimate and simulate the effect of space charge [3], and they are quite equivalent, as is described in [1]. The space charge effect is mostly calculated, but is not observed directly.

With the laser test facility described in this work, the space charge effect can be observed and investigated. A detailed discussion will be given in Section 8.2.

3.4 Objectives of research

As a conclusion of this chapter, a clear objective with multiple application can be determined.

- Our main objective is to perform a precise measurement of the gas parameters of a real RPC detector at atmospheric pressure.

- To be able to perform a precise measurement, the investigation of several processes related to gas physics and detector physics are required.

- To develop high precision methods for RPC detector tests. It will contribute to the future application, for both fundamental understanding of performances, and alternative eco-friendly gas researches.

- To make a direct measurement of the gas parameters in the field strength of timing RPC to investigate the physical models of RPCs.

Considering our experiences in RPC design and operation, and that the Laser Particle Acceleration Division in HZDR can support the laser system, our objectives and the related experimental works are:

- Assemble a laser test facility, which is capable for generating stable laser pulses (Chapter 4.).

- Assemble the detector samples of RPCs and drift tube (Chapter 4.).

- Confirm that the laser can ionize gas particles to generate a certain number of primary electrons in a controlled position with high accuracy (Chapter 5.).

- Develop methods to make sure that the detectors work properly with laser as the ionization source (Chapter 5.).

- Confirm that we can obtain the gas parameters properly in known field strength of trigger RPC (Chapter 6.).

- Develop the methods to make measurements in higher fields, from trigger RPCs, up to timing RPCs or higher (Chapter 6.);

- Obtain the gas parameters in trigger RPCs and timing RPCs (Chapter 6 and Chapter 8.).

Chapter 4

The laser test facility

Pulsed-laser technology has been widely used for calibration of gaseous detectors and measurement of gas parameters. In order to produce a signal in a gaseous detector, primary electrons should be first produced in the active region inside the detector. The technology provides a possibility of producing primary ionizations in a well-defined spatial position and well-controlled number of electrons.

An UV-laser test facility is assembled in HZDR. The facility contains a laser generation system with micrometer accuracy, different detector samples designed for laser input, an automatic control software and other necessary devices. Based on existing works, we have made developments in several aspects, and brought new designs, to achieve the high accuracy required by our research. In this chapter, the laser test facility will be introduced in detail.

4.1   Methods of producing primary ionizations

A signal output from gaseous detectors starts from primary ionizations. For a specific detector, the procedure of secondary ionizations is only determined by the detector itself, while independent from how primary ionizations are generated.

There are several methods for creating primary electrons inside the gaseous detector. In the calibrations or performance tests of RPC detectors, the common methods are as follows:

- Testing with an accelerator, where the primary ionizations are from charged particles that travel through the RPC. The RPC detector is mounted in the beam line or at the location where the particle passes. In such experiments, RPCs are tested in the realistic usage scenario, so that the overall performance of a full RPC detector can be investigated. However, the fundamental mechanism of RPC performance can only be obtained by analysis and derivation indirectly.

- Testing with cosmic rays, where the primary ionizations are caused by cosmic ray muons with random spatial distribution. A cosmic ray system contains multiple detectors that allows one cosmic ray muon passing through all the detectors, while the trigger is provided by the coincidence of signals. A cosmic ray test system provides the information of all performance characteristics of a RPC detector except for rate capability. While similar to accelerator test, a fundamental research of signal process cannot be revealed by the test.

- Testing with X-ray source, where primary ionizations are caused by X-ray photons. The X-ray source is either from an X-ray generator or a radioactive source. When the energy of emitted X-rays is beyond the ionization potential of gas atoms or molecules, ionization will be produced in the gas gap of RPC by the photoelectric effect. In the case that the ionizations are from X-rays, the positions of primary ionizations is related to the X-ray intensity distribution. Testing with X-ray provides fewer information compared to other methods. It is usually applied for availability test or ageing test.

- Testing with pulsed-laser, where primary ionizations are caused by multi-photon ionization effect (MPI). A laser facility provides photons with less energy compared to X-rays where MPI occurs. Electrons ionized by the laser will be distributed only in the region of the focus of the laser beam, the positions of primary ionizations are precisely controlled. As the RPC sample will be different from on-site RPCs in experiments, the method is not suitable for overall performance tests. It is the ideal way to investigate the RPC performance in a more fundamental scenario.

The most suitable option for the purpose of this thesis is to assemble a laser test facility and apply fundamental researches.

4.2   Application of laser in gas detector experiments: a review

The development of laser technology has brought the experimental discovery of multi-photon ionization (MPI). Since the year 1979, laser calibration method using MPI effect has found applications in various gaseous detectors. In such an experiment, a laser beam is focused into the available region of a detector. Because of its unique mechanism that provides a possibility to define the position and time of primary ionizations, early experiments have proved that laser is a stable and powerful tool for the purpose of research and calibration.

The laser test technology has also been applied in the tests of RPC detectors in several works. In this section, we will make a short review on the laser calibration methods.

4.2.1   Early applications of UV laser in gaseous detectors

Laser calibration for detectors was first applied for proportional chambers (wire chambers) in 1979 in [74, 75, 76]. These works are independent from one another, using different laser test systems for different drift chamber detectors and gases. Their success in generating laser ionization signals has proven that using UV laser as an electron source is a very useful experimental method, acceptable for different common gases of gaseous detectors.

Yet at that time the lacking of proper understanding of the main ionization processes in ionization has led to conflicting results. The reason of the differences was then clarified in [77]: when the laser intensity is below a certain value, number of ionizations is proportional to square of laser intensity; when it is beyond a threshold value, saturation effect appears and the dependence of number of electrons and laser intensity become linearly related. It was later reported in [78] that a focused laser beam can generate ionization within limited region of the beam focal spot. The position of the laser focus is moved in the gas by changing the position of the detector, and the signal distribution on different wires changed. In [79, 80], it is reported

that when the wavelength of laser is changed, the number of ionization changes rapidly. The ionization cross section becomes too small when the wavelength of the laser becomes long.

Most of the researchers agreed that the ionizations are mainly contributed from impurities in gas. It is reported that, by removing the very small fraction of impurities, the ionization number is greatly reduced, and the main contribution of electrons is still from double photon absorption. A gas system with special design for removing impurities is designed in [81] and has shown that the fraction of impurities is very small but very stable.

A review and conclusion of the above experiments is presented in [82]. The main process of laser ionization in detector gases and the methods of laser tests in gaseous detectors have been established. Laser test systems then became widely used in calibration of gas detectors [83, 84, 85], mainly drift detectors, time projection chambers and streamer chambers.

The detectors have different structures, but they are similar under laser calibration. There are drift regions and avalanche regions in the working gas, and the laser is always applied in the drift zone so that the signal time is sensitive to the position of laser, while the signal charge is independent from the position, except in avalanche or streamer regions.

4.2.2 Measuring gas parameters with reduced pressure

The tests of gas parameters in high electric fields with parallel plate detectors are usually performed at reduced pressure. As is introduced in Section 3.3, the Townsend coefficient of a gas or gas mixture can be experimentally determined at reduced pressure following Equation (3.27), supposed to be valid in the full range of electric field strength of RPCs.

From Equation (3.27) it can be concluded that we can take α_{eff}/p and E/p as parameters instead of α_{eff}, E and p. And more importantly, the Townsend coefficient at high field can be measured under reduced field at reduced pressure, where the measurement is not possible at atmospheric pressure because of streamers, sparks or huge discharges at atmospheric pressure.

The method to obtain gas parameters in reduced electric fields has been widely used. In such experiments , one uses the unit Townsend (Td). The ratio of Td is E/N, where E is the electric field strength and N is the volume density of gas particles. The definition of $1\,\text{Td}$ is accordingly:

$$1Td = 10^{-17} V\,cm^2 \; . \tag{4.1}$$

The density of gas particles at normal atmospheric pressure of $1\,\text{atm}$ and room temperature is about $2.5 \times 10^{19}\,\text{cm}^{-3}$.

For a RPC operating at atmospheric pressure and at the field strength of x kV/cm (where x is an arbitrary value), the reduced electric field is then:

$$\frac{x}{N} = \frac{x\,10^4 V/cm}{2.5 \times 10^{19}/cm^2} = 40\,x\,Td \; . \tag{4.2}$$

Though the measurements are not specialized for RPC detector, there are works that is of importance to the gas parameters: The Townsend coefficient and electron drift velocity of Freon are measured precisely in [4]. The device for measuring the gas parameters is a pulsed Townsend test facility described in [86]. The detector component is placed in a vessel ($50\,\text{cm}$ diameter, $60\,\text{cm}$ height), and the pressure inside the vessel can be tuned.

The detector consists of two parallel electrodes: The upper anode is a $12\,\text{cm}$ diameter steel

plate with a 1.5 cm diameter hole with thin mesh in the center for input of UV laser, the lower cathode is an aluminium plate the same size and without hole. The distance between the electrodes can be adjusted with maximum range of 3.5 cm. In general, it is constructed similar to a parallel plate chamber detector.

The pressure in experiments are set in the range from 530 Pa to 4000 Pa, while the reduced electric field ranges from 0.2 to 1000 Td. The equivalent reduced field strength of a timing RPC detector of 100 kV/cm is 400 Td, i.e. the tests have covered the full working range of RPC detectors. The obtained values are applied in the Monte Carlo simulation program Magboltz. The values are of high importance to the calculations with RPC detector. The experimental results of the work in this thesis will also be compared to the work in [4].

4.2.3   Measuring gas parameters at atmospheric pressure in RPCs

As RPC technologies have become widely used in high-energy physic experiments, the measurement of gas parameters for RPC detectors is operated in many works with different methods. Although a RPC has basically very simple structure, understanding of RPC is still incomplete. Also, the experimental data are needed as the database of Monte Carlo simulations.

The difficulties for a comprehensive study of the RPC detectors, can be briefly listed below:

- No drift region. A RPC detector has only avalanche or streamer regions in the gas gap. Without a drift region, the signals of RPCs are very sensitive to the initial position of primary ionizations. The positions of primary electrons are usually randomly distributed in most of test methods.

- Very high electric field and amplification. The high electric field has brought difficulties in measuring the gas parameters. As the parameters are very high, the development of amplification process is very fast, including the development of avalanches, and the transformation from avalanche signal to streamer signal.

These characteristics have result in a requirement of very high sensitivity. In some of the works, a test method with UV laser is developed and be proved efficient, as the experimental results are comparable with the measurement results at reduced pressure and reduced field in [4].

4.2.3.1   Method of producing primary electrons on the gas molecules

In [5], a specially designed RPC is placed in a box that allows laser input through a quartz window. The drift velocity and effective Townsend coefficient was measured with 97% Freon+3% iso-Butane gas. The measurement was performed under the voltage concerning the RPC working conditions at LHC experiments, around 8.6 to 9.4 kV. Considering the width of gas gap is 2 mm, the field strength is 43 to 47 kV/cm. This is within the range of trigger RPCs.

Another measurement of RPC gas parameters is described in [87] and [6]. An ATLAS-like RPC prototype was designed with Bakelite electrodes for the purpose to study the gas parameters of ATLAS RPC. Electron drift velocity and effective Townsend coefficient were measured for field strength of 45 to 55 kV/cm for the RPC gas containing 94.7% Freon + 5% iso-Butane + 0.3% SF_6. The test was also operated within the trigger RPC range.

The ionization source is N_2 laser with $337\,$nm wavelength. The laser is focused by a lens, the repetition rate is $20\,$Hz, FWHM pulse duration is $\leq 700\,$ps, energy $100\,\mu$J/pulse. The reference time is taken from laser source. The dimensions of the electrodes are 10×20 cm^2 and the gas gap is $2\,$mm. The volume resistivity of electrodes is about 1.4×10^{11} or 1.7×10^{10} Ωcm depending on the use of different materials. In the experiment, the time of signal and charge spectrum are recorded. For the repetition rate below $1\,$Hz and volume resistivity of electrodes of 1.7×10^{10} Ωcm, the signal spectrum of single ionizations can be observed, otherwise the system cannot reach a stable condition.

The electron drift velocity and effective Townsend coefficient are obtained for different field strengths and compared to a value from Magboltz simulation. The numbers are in satisfactory agreement of measurement and simulation. The details of the data will be discussed and compared in Section 6.1.

4.2.3.2   Method of producing primary electrons on the surface of electrodes

Except for using lasers to ionize gas particles by multi-photon ionization, other methods are also possible. A facility for the measurement of gas parameters at atmospheric pressure is presented in [88]. This system uses a RPC sample in order to reach high electric field without risks of sparks. This work is not specialized for the gas in RPC but aiming at an universal method for gas physics research.

The cathode of the detector sample is an aluminium plate. A $3\,$mm thick float glass electrode with bulk resistivity of 2×10^{12} Ωcm is mounted as anode on a linear motion stage with accuracy of $2\,\mu$m. The width of gas gap can be modified by changing the position of the linear motion stage. A N_2 laser UV beam is applied on the aluminium plate to generate primary electrons by photoelectric emission.

The repetition rate of the experiment is up to $20\,$Hz, and in the experiment it was set to $5\,$Hz. The gas in the measurement is Nitrogen and the data acquired from experiment is compared to other works and found to be in agreement for Nitrogen gas but disagreement for iso-Butane gas. The experimental results are obtained in the range of field strength is up to $200\,$Td, comparable to the field strength up to $50\,$kV/cm at atmospheric pressure.

4.2.4   Conclusions

From the experiments described in Section 4.2, it can be concluded that:

- measurement method at reduced pressure has been well developed that the reduced electric field is much beyond the field strength of Timing RPC. The gas parameters of RPC working gas components are studied.

- measurement method at atmospheric pressure is successful in the field range of trigger RPC. No measurement of gas parameters with field strength of above $50\,$kV/cm at atmospheric pressure has been performed yet.

4.3   HZDR laser test facility: objectives and conceptional design

An early version of the test facility was assembled [89] successfully. Gas parameters are measured with different RPC samples, the effective Townsend coefficient and the electron drift velocity are measured. The results of the measurement has showed a disagreement of the effective Townsend coefficient and agreement in electron drift velocity, respectively, between experimental values and simulations. The disagreement need to be further investigated and explained by more experiments. However, as it was an early version without control system, there was no effective way for a comparative systematic experiment.

For the upgrade of the laser test facility, great efforts were taken. Nowadays, by dealing with various issues in the approach to the experimental experiments, the main characteristics of the laser test facility have fulfilled the experimental objectives. The improvements are achieved by upgrades of devices and implementation of automatic control system.

An introduction of the automatic system will be presented in Appendix C.

The conceptional design of the laser test facility depends on the other experiments described in Section 4.2.3 and the early setup of our test facility. Except for existing experiences, some specific difficulties need to be overcome. The measurement of gas parameters of timing RPC has several difficulties, including the development of a system from laser generator to detector, the accuracy of position, the development of data acquisition, etc. For the objective of measuring the gas parameters at atmospheric pressure in high and homogeneous electric fields of $100\,\mathrm{kV/cm}$, new methods need to be developed.

A calibration test system should concern the following main aspects: primary electrons, detectors and signal readout layouts.

For a laser calibration facility, there are two different ways to generate primary ionization by laser: photoelectrons on the cathode surface material or multi-photon-ionization electrons of the gas molecules in the gas gap. Considering the RPC detector, as we want to measure the gas parameters at atmospheric pressure, except for the risk of sparks, the main challenge for such condition is that the effective Townsend coefficient is very high. In a timing RPC, the width of gas gap is usually around $0.3\,\mathrm{mm}$, otherwise the signal is very likely to develop into a huge charge and then a breakthrough happens. Based on the practical experiences, we can assume that our test scale is also within the range of around $0.3\,\mathrm{mm}$.

The accuracy of position should be at least one or two orders of magnitude smaller than the scale of RPC gas gap, to provide measurements of electron drift velocity and charge amplification in high accuracy. This means that, the shape of laser beam should allow a position shift of more than $0.1\,\mathrm{mm}$ along the field direction without streaking the electrodes. As the laser system and the detector system are independent, and the main requirement for the laser system is the stability of the intensity, the movement stage should be mounted with the detector box.

The challenges in accuracy are due to the very high Townsend coefficient and too small scale. They can be solved by the increase of accuracy, and the improvement of the methods of position calibration. The laser test facility and the automatic control system has provide us the possibility to overcome the difficulties.

To measure the gas parameters at atmospheric pressure without a too large signal, one can also consider that to reduce the gap width to limit the avalanche. Unfortunately, this approach is not possible, due to practical reasons: it is not possible to reduce the gas gap to be very small but the sample still acts as a RPC detector. According to experimental experience, when the gas gap is too narrow (for example $0.1\,\mathrm{mm}$), the performance becomes very different since Paschen's

law fails [90] and becomes a situation different from the RPC involved detector physics.[1] The gas gap of MRPC is already reaching the limit of a detector where the reduction of gap width is difficult.

So another way must be found. As a result, the following experimental method is proposed: as is already discussed in Section 4, making an ionization in the gas gap by MPI from a laser pulse. With this method, we can control the position of the laser inside the gas gap (although we cannot put it in any position because of shape of laser beam) the available range for testing is still large enough to perform a measurement.

4.4 Laser generation and focusing

The first setup of the HZDR laser test facility and the obtained results were reported in 2014 [89]. The UV laser generation system was first established. Afterwards, two kinds of gas detector samples were assembled: a drift tube for calibrating the electron generation, and a RPC to measure the gas parameters. After the publication, we keep on updating and adjusting the system.

4.4.1 Environment

The laser test facility is implemented in a clean room with stable temperature. A full time air filter system is installed in the room to reduce dust in the air. The room temperature is controlled by an air conditioner working 24 hours a day and 365 days a year. The temperature in the room is $20.0 \pm 0.4\,°C$. Gas bottles are placed outdoor. As the metallic gas pipe is crossing the whole room with low gas flux, the temperature of gas is the same as room temperature. The full laser test facility system is mounted on an optical table.

4.4.2 Laser pulse generation

The laser generation system is assembled by the Laser Particle Acceleration Division of HZDR. Laser pulses from oscillators are fed into the laser amplifier. The Yb:Yag gain medium in the amplifier is excited by the pumping source from another laser. On the gain medium, spontaneous and stimulated emissions of photons occurs, photons of wavelength $1030\,nm$ is generated. The wavelength is reduced by a factor of two, two times by two beta barium borate crystals (BBOs). As a result, our system has the final output laser beam wavelength of $257\,nm$, i.e. the photon energy is $4.8\,eV$.

The possible repetition rate is up to $100\,kHz$, and the energy per pulse can be tuned between 0 to $100\,J/pulse$. The fluctuation of laser energy is controlled to be less than 3%. The pulse duration is $2\,ps$ (FWHM).

---

[1]It should be noted that, although in this thesis, a difference between measurement results and calculation appears (will be discussed in Section 6 and Section 8); as far as we have understood now, it does not seem to be the same phenomenon described as the 'failure of Paschen's law' in [90] and other works devoted to this subjects. The reason is that the scale of gap width of RPC detector we use, is one or two magnitude larger than the scale which 'failure of Paschen's law' appears in the quoted researches. A further discussion will be beyond the detector physics, and has little connection to the work in this thesis.

(i) Manual attenuation.   (ii) Automatic attenuation.
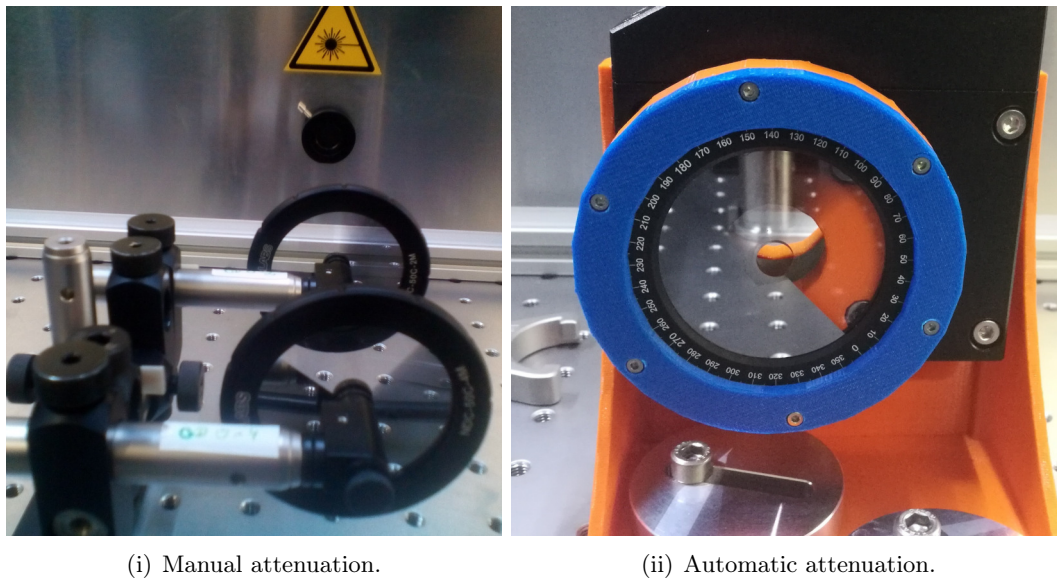
Figure 4.1: A photo of laser energy attenuators. One or two 'round continuous
variable neutral density filters' are used for automatic or manual
adjustment.

The laser generation system is similar to the facility described in [91, 92].

4.4.3   Attenuation

The intensity of the laser is controlled by attenuators installed in the beam line between the
laser generation system and the optic system. Two different methods of attenuation are applied:
manual attenuation and automatic attenuation, as presented in Figure 4.1. The rotation stage
for automatic attenuation is controlled by software. The accuracy of the automatic attenuation
system is in the order of $0.01\,\mathrm{dB}$, while the accuracy of adjustment by hand is in the order of
$0.1\,\mathrm{dB}$

4.4.4   High precision focusing
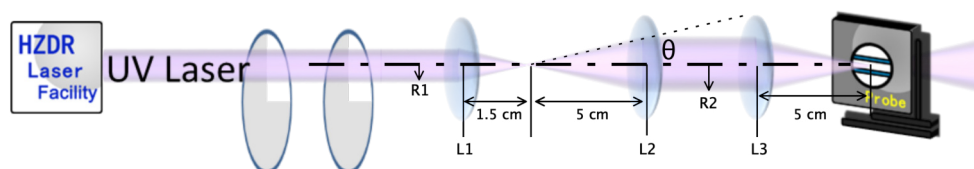
Figure 4.2: The optical focusing system for laser pulses.

In order to focus the laser pulses into the detectors, the laser beam is focused by lenses. As
shown in Figure 4.2, three UV lenses (L_1, L_2 and L_3) are placed in the center of the beam line
between the laser generator and detector. The focal lengths of the three lenses are $L_1 = 1.5\,\mathrm{cm}$,
$L_2 = L_3 = 3\,\mathrm{cm}$.

The laser beam is first focused by L_1. As the beam angle of the primary laser beam out of the laser generator is small, we can assume that the output is an almost parallel beam with beam radius of R_1. The beam angle θ is then $\theta = \frac{R_1}{L_1}$. L_2 is placed on the position that the focus of L_2 is on the beam focus after L_1, so that the laser beam is a parallel beam after L_2. The beam radius R_2 is $R_2 = \theta L_2 = \frac{R_1 L_2}{L_1}$. The position of L_3 is placed in front of the detector. All lenses are fixed on the optical table to guarantee a precision of the positioning in all three dimensions better than $1\,\mu m$.

4.4.5 Moving stage for detectors

The measurement of gas parameters requires high accuracy of position control. A three axes moving stage[2] is chosen for the experiments as the calibration requires high precision in three dimensions.

Each individual axis has a moving range of $8\,mm$, the minimum step length is $4.4\,nm$. Considering that the scale of gas gap of RPC is sub-millimeter, which is five orders of magnitude larger than the minimum step, we can set the experimental step length to be $1\,\mu m$, so that one experimental step length contains more than 200 built-in steps of the driving motor. The accuracy of position is better than 1%.

On the other hand, the step length of $1\,\mu m$ is two orders of magnitude smaller than the scale of gas gap of the used RPC samples, and much smaller than wire detectors, so that the accuracy is enough for our experiments. The step length is currently the suitable choice to satisfy the experimental requirements with reasonable difficulty in programming. If we need higher accuracy in the future, it is also easy to define a smaller experimental step length.

The moving stage is controlled together with other devices by Labview programs [93] in a PC. In an experiment, the number of measuring points can be up to several thousands. Such experiments can only be operated with the assistance of the automatic program. Our long-term test has shown that the step-driver device is very stable and reliable with proper maintenance.

However, the absolute accuracy of laser position is not only depending on the accuracy of the moving stage, but the alignment of the full system. The overall absolute accuracy of laser focus in the gas gap is in the order of tens of several μm, where the accuracy is not high enough compared to the requirements; however, the relative position accuracy of position is two or three orders of magnitude better. The relative position accuracy has satisfied the experimental requirements.

4.5 Detectors for laser test

4.5.1 Introduction

The detectors are independent from the laser generation system. The considerations of the detector box are:

- Two windows should be assembled so that the laser beam can go through for the purpose of alignment of laser position, and measurement of laser pulse energy.

---

[2]The step driver device we use is OWIS Motorized XYZ Stage KTM 65.
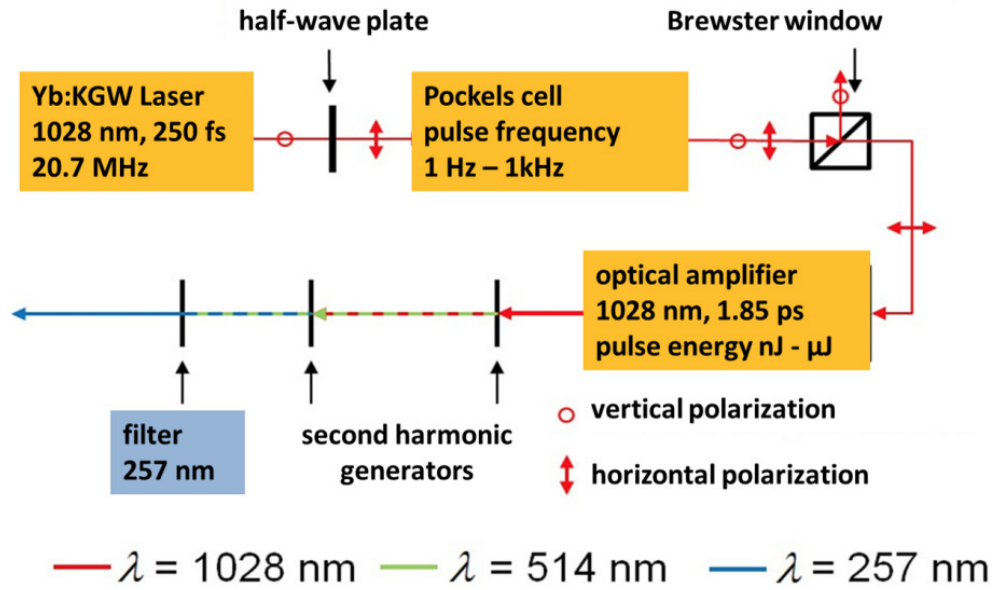
Figure 4.3: Schematic drawing of the setup for the laser-plasma generation
in [89]. The laser is amplified and its output wavelength changes
from 1030 nm to 257 nm by two second harmonic generators. The
output 257 nm laser beam is used as the ionization source in our
experiments.

- The box should be metallic. The first objective is to avoid electric noise from outside, the second is to make sure the gas box is stiff so that no significant mechanical deformation will appear.

- It must be light so that it can be mounted on the moving stage. The maximum load of the moving stage is about 500 g.

- It should include gas input/output pipes and insure gas tightness.

- It should include high voltage supply and signal output.

- It should have the possibility to implement an optional window for tests with the X-rays from ^{55}Fe radioactive source.

- It will be used for the calibration of laser, especially for the number of primary electrons generated in a pulse and the spatial distribution of beam intensity near the focus.

- The gap width of the RPC sample should be adjustable or several RPC samples with different gap widths should be prepared, so that we can test and compare the gas parameters in different sample geometries.

Finally, a drift tube sample for laser calibration, different RPC cells are assembled for experiments.

4.5.2   Drift tube detector

The drift tube detector is an aluminium box with a drift tube inside. The drift tube is a general kind of gaseous detector with two main components: a wire as the anode and a tube as the cathode. When high voltage is applied between the wire and the tube, non homogeneous

(i) Schematic drawing of a drfit tube.

(ii) Regions in a drift tube.
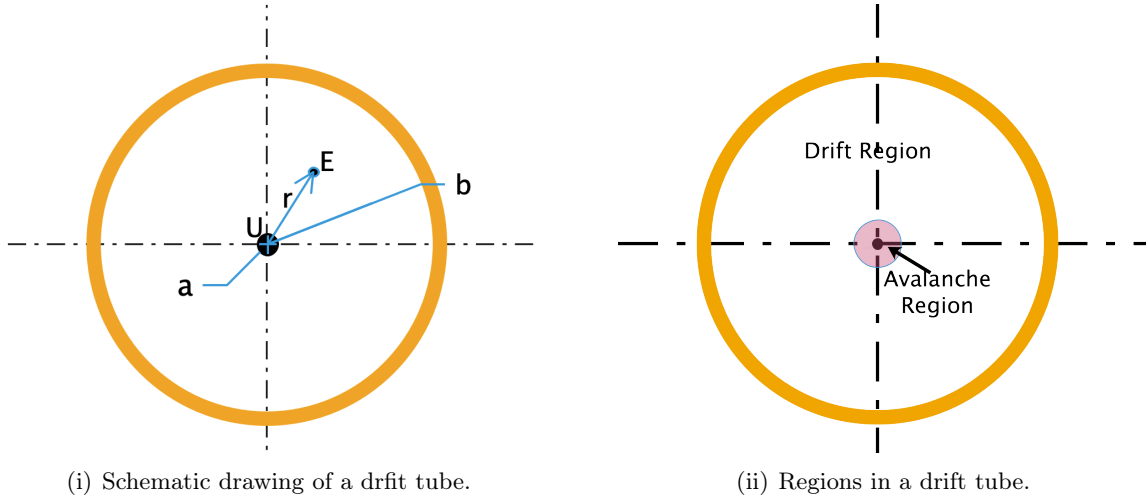
Figure 4.4: Schematic drawing of a drift tube. a and b are the radius of anode wire and the inner radius of the tube, respectively; U is the potential of the anode; E is the field strength at the position where the distance to anode is r. A drift tube has a large drift region and relatively small avalanche region.

electric field is generated in the tube. The electric field inside the tube can be subdivided into two different regions: the drift region and amplification region.

As shown in Figure 4.4(i), if r is the distance from an inner point to the anode, U is the applied voltage between the anode and cathode, the radius of the wire is a, and the inner radius of the tube is b, then the electric field E at the position where the distance to anode is r is written as:

$$E(r) = \frac{U}{r\, ln\left(\frac{b}{a}\right)} \ . \tag{4.3}$$

The field strength closer to the wire is stronger. In most positions where r is not very small, the electric field is not high enough to amplify the electrons, so that the number of electrons is constant regardless of attachments. When r is so small, the field strength is high so that electron avalanches will occur to amplify the signal, see figure 4.4(ii). The boundary of the two regions depends on the relative voltage applied on the anode.

The assembled drift tube is shown in Figure 4.5. The radius of the wire is $6\,\mu m$, and inner radius of the tube is $6\,mm$.

4.5.3 RPC detectors

4.5.3.1 Glass and ceramic RPC(I) samples

The RPCs were assembled for the early test with the early version of laser test facility. The conceptional design is exhibited in Figure 3.1(i). Precision of the gap width should be guaranteed, and we also want to have an easy way to adjust the gap width of the RPC.

As a result, the detector box and the RPCs are designed as individual components. RPC
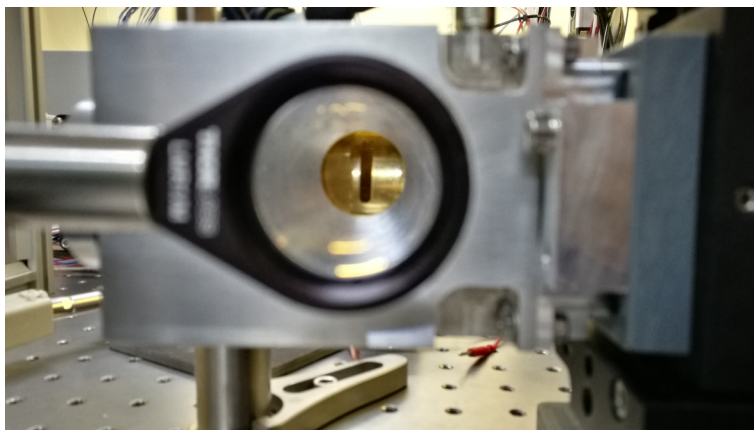
Figure 4.5: The drift tube detector with a slit for laser input.
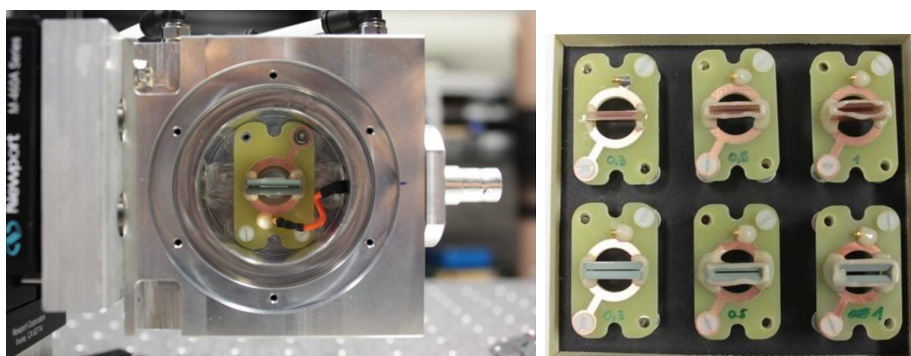
(i) A picture of RPC sample in the box.

(ii) The six RPC samples.   The upper samples are with glass electrodes, bottom samples are with ceramic electrodes.

Figure 4.6: RPC(I) samples for laser test.

samples are made in the form of a 'chip' assembled inside the gas box, so that it is easy to change the materials and gap width by exchanging the RPC samples. Six RPC samples are presently assembled. The electrode materials are glass and ceramic [30], respectively, and the gap widths are 0.3, 0.5 and 1 mm for both materials. The thickness of the glass electrodes and ceramic electrodes is 1 and 2 mm, respectively. Their length is 15 mm, and the width of the electrodes is set as eight times the gap width along the beam direction to guarantee the electric field to be homogeneous in the center.

The signal is readout from a RC-splitter box from the high voltage to simplify the design of the RPC detector sample and reduce the number of connectors.

The cross sections of glass electrodes and ceramic electrodes are rectangular and trapezoidal, respectively. A picture of the RPC gas box and the RPC samples is shown in Figure 4.6.

In order to be distinguished from a later design, the ceramic RPC samples in this section is called 'ceramic RPC(I)'
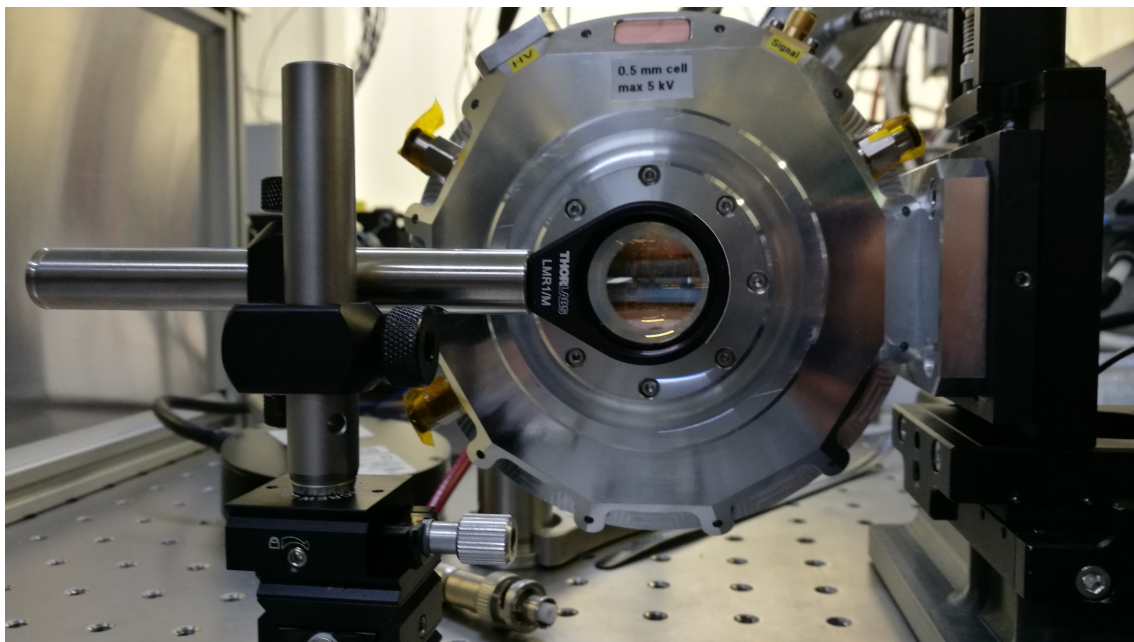
Figure 4.7: The ceramic RPC(II) in the gas box.

4.5.3.2   Ceramic RPC(II)

After the experiments with the float glass electrode RPC sample are finished (described in
Sections 6.1, 6.2 and 6.3.1), many upgrades are taken including the detectors, experimental
methods and software. This section introduces the upgrades from namely 'RPC(I)' to 'RPC(II)'.

The ceramic RPC(II) is assembled with a different design compared to the RPCs in Section
4.5.3.1. The upgrades are listed in the following:

- The signal is separated from the high voltage to avoid reflections caused by the issue
  of impedance matching around the splitter box, which is impossible to prevent for the
  electronic layout of RPC(I).

- The electrodes are ceramic with volume resistivity three orders of magnitude smaller than
  float glass, decreasing the time constant of several seconds to several milliseconds.

- The edges of the electrodes are rounded to avoid discharges.

Two other changes are made:

- A new design of gas box is applied to reduce the weight for the upgrade of three-dimension
  moving stage.

- The gap width is designed adjustable; although in our experiments it is fixed to 0.5 mm.

A picture of the ceramic RPC(II) is shown in Figure 4.7. After all experiments are finished,
we have concluded that ceramic RPC(II) is the most suitable device for the test of gas parameters
with acceptable high rate and excellent waveform recording. Further discussions will be presented
in Section 6.3.2.

Chapter 5

Experimental study on laser ionization

UV laser is the ionization source for our HZDR laser test facility. It should be regarded as one of the most important part in the test facility. A dedicated investigation of the properties of multi-photon ionization is necessary.

This chapter will be devoted into two main objectives:

- Investigation of the characteristics of laser focus;

- Investigation of the properties of multi-photon ionization process.

The spatial distribution of the laser intensity is measured by mounting a sharp edge on the three-dimension moving stage. With the combined operation of experimental devices and the control system, detailed figure of the spacial distribution of laser intensity at the focus position is acquired. With the wire chamber as the calibration detector for laser test system, the characteristics of multi-photon ionization is studied. The experimental results are compared to calculations, and good agreement is found.

This section contains the method to accumulate a detailed intensity map of the laser focus with the laser test facility, the result of tests and calculations of the size of laser focus and the number of primary electrons. With the results obtained in this chapter, the ionization process in RPC detector can be inferred.

5.1 Spatial intensity distribution of laser focus

As the accuracy of measurement has a significant dependence on the size of the laser beam spot inside the detector, the size of the focus and the beam flux need to be characterized in detail.

5.1.1 Brief introduction of Gaussian beam distribution

The laser focus at a small scale is in the form of a Gaussian beam. The laser intensity is described by the formula:

$$I(r,z) = \frac{P}{\pi\,w(z)^2} e^{\left(-2\frac{r^2}{w(z)^2}\right)} \ , \tag{5.1}$$

$$w(z) = w_0\sqrt{1 + \left(\frac{z}{Z_R}\right)^2} \ , \tag{5.2}$$

$$Z_R = \frac{\pi\,w_0^2}{\lambda} \ , \tag{5.3}$$

$$w_0 = \frac{\lambda}{\pi\,\theta} \ , \tag{5.4}$$

where r and z are polar coordinates of a certain point in space, $I(r,z)$ is the laser intensity at the position, P is the power of laser, $w(z)$ is the beam radius, w_0 is the beam waist, Z_R is the Rayleigh length[1], λ is the wavelength of photons and θ is the beam angle.

The beam radius $w(z)$ is the distance to the beam center, where the intensity drops to $1/e^2$ of the central intensity. From Equation (5.3) and (5.4), it could be concluded that the minimum beam waist is determined by the beam angle θ. The dimensions of the laser focus can be controlled by setting up a value of θ. As the focal length of a lens is fixed, θ is then determined by the radius of input laser r_{in}. An example of Gaussian beam is shown in Figure 5.1.
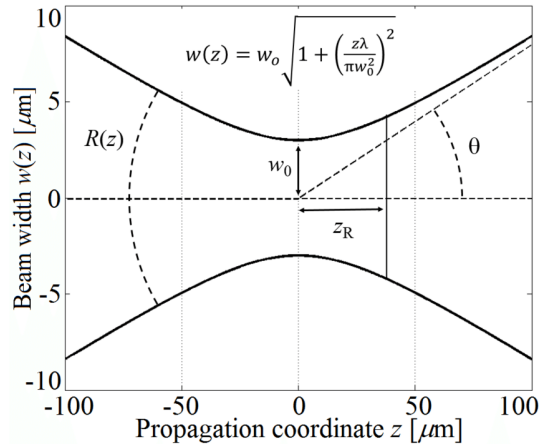
Figure 5.1: A figure of Gaussian beam from [94]. In this figure, $w(z)$ is the beam radius, w_0 is the beam waist, Z_R is the Rayleigh length, λ is the wavelength of photons, θ is the beam angle, z is the position on the propagation coordinate. The figure is an example obtained with different parameters with our experiment. The main purpose of this example is for explaining the shape of Gaussian beam. Experimental scans of Gaussian beam with HZDR laser test facility will be presented in figure 5.5.

---

[1]The Rayleigh length is defined as the distance along the beam direction, where the area of the cross section is doubled compared to the area of the cross section at the center of focus.

5.1.2 Calculation of laser intensity distribution

In order to make a simulation of the laser intensity distribution, we established a Labview calculation program for finite element analysis. In this program, the input parameters are the range of space, the position and intensity of the Gaussian beam and the number of divisions on three dimensions. The output is the intensity distribution from 1-dimension to 3-dimensions.

In this thesis, X and Y axes are perpendicular to the laser beam, in the horizontal and vertical direction, respectively; Z axis is along the beam direction, pointing to the outgoing direction of laser.

For each element, the laser intensity I_{xyz} is calculated by Equation (5.1) at the middle point and be taken as the energy within the whole element. The wavelength of laser is $257\,\mathrm{nm}$. The 'power' within this cell is then $I_{xyz}dxdydz$. If the intensity map is the projection of the laser beam on XZ plane, then it can be calculated by:

$$I_{xz} = \sum_y I_{xyz} \ .$$

(5.5)

The program can generate a map of intensity. We set the center of the laser focus at $(0,0)$, and the input beam radius $r_{in} = 1\,\mathrm{mm}$. The beam waist and Rayleigh length are:

$$w_0 = \frac{\lambda}{\pi\,\theta} = 4.09\,\mathrm{\mu m} \ ,$$

(5.6)

$$Z_R = \frac{\pi\,w_0^2}{\lambda} = 204.5\,\mathrm{\mu m} \ .$$

(5.7)

The intensity map with maximum value normalized to 100 is shown in Figure 5.2.
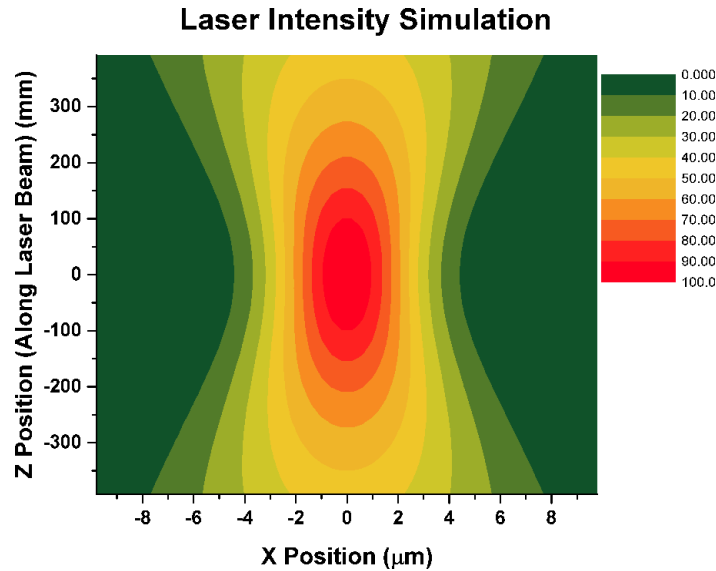
Figure 5.2: Result of a calculation of intensity map of the laser beam in our HZDR laser test facility by finite element analysis. The maximum value is normalized to 100. It is in agreement with the experimental measurement data with the same parameters shown in Figure 5.5.

5.2   Measurement of beam radius

5.2.1   Experimental setup and obtained intensity map

The above mentioned intensity map can be measured with the step-driver system. We designed and assembled a special edge consists of two blades, along with their associated support components. The edge is used to block the laser. When the edge is placed on different positions in a section perpendicular to the laser beam direction, and a laser energy sensor is placed after the edge, laser beam intensity from zero to maximum will be acquired, depending on how much of the laser beam intensity is blocked by the blade. In the experiment, the laser pulse energy was set to 50 nJ, and the frequency was set to 10 Hz. An adjustable diaphragm is placed between the 2nd and 3rd lenses (see Figure 4.4), and the radius of the hole is set to 1 mm.

As shown in Figure 5.3, if the edge is placed at the positions of X_1 and X_2, the difference of the laser energy e is the energy within X_1 and X_2.

$$X_1 \hspace{8em} X_2$$
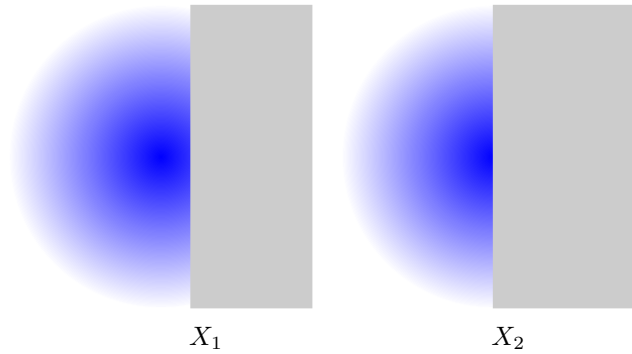
Figure 5.3: The method of measuring the laser intensity by a sharp edge at different positions. This figure shows two different horizontal positions X of the edge at the same cross section with the same position of Z.

In the automatic systems, for a certain section, the positions of the edge are set to $x_i, i = (1, 2, 3, .., n)$, and the distances between neighbouring points are the same. The position x_i and laser energy e_i at a point can be defined by:

$$x_i = \frac{X_i + X_{i+1}}{2} \ , \tag{5.8}$$

$$e_i = E_{i+1} - E_i \ , \tag{5.9}$$

where X_i and X_{i+1} are two neighbouring positions, E_i and E_{i+1} are the laser intensities measured at X_i and X_{i+1}, respectively.

For a certain section perpendicular to the laser beam, the distribution of laser energy will be Gaussian-like, and the FWHM is smaller at the focus position than other regions along the beam line. The energy distribution acquired at different Z positions along laser beam line are shown in Figure 5.4.

In our experiment, the automatic program is used to make a three-dimension scan along the beam direction (Z axis) at $z_i, i = (1, 2, 3, .., n)$. At each value of z_i, there is an energy distribution
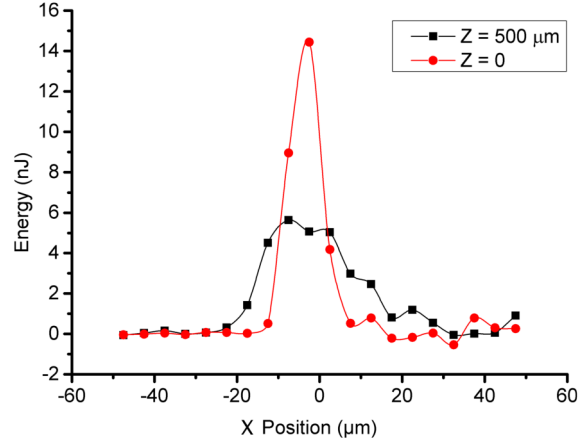
Figure 5.4: The energy distribution of two different cross sections displaced
along the beam direction Z. The zero point is defined at the center
of the laser focus. The measurement is operated in the horizontal
direction.

scanned for different x_i. The laser energy is recorded for each position. The energy distribution
histogram is then combined into one two-dimension map to present the intensity distribution of
the Gaussian beam. Figure 5.5(iii) exhibits a Z-X cut of the energy distribution and the shape
of the envelops. The beam radius is $5\,\mu$m and the Rayleigh length of the focus is about $200\,\mu$m.
This is in agreement with Equation (5.6).

Figure 5.5 displays the shape of the laser focus. Compared to other figures with larger
scale, Figure 5.5(iii) shows larger fluctuations. This can be explained by the very small distance
between steps so that the fluctuations cannot be ignored. The laser energy was set to $80\,$nJ : a
value close to upper limit of the system, and frequency was set to a value that would not harm
the blade, which is $10\,$Hz.

In the previous tests, we damaged the blade with $100\,$Hz laser frequency (Figure 5.6), and
after that we reduce the frequency to $10\,$Hz, the blade was not damaged again.

5.2.2   Error estimation on each pixel of intensity map

As the full energy of the laser pulse is $E = 50\,$nJ, the energy measured from each position X_i is
E_i, we can know that when Z position is at beam waist ($r \approx 5\,\mu$m), the average value measured
within the beam waist is $\frac{E\,\triangle x}{10\,\mu\mathrm{m}}$. For the value acquired by the laser sensor, the error comes from
the fluctuation of laser

$$\sigma_1 = 3\%\,E_i \ , \tag{5.10}$$

and the uncertainty of measurement of laser sensor, which is approximately

$$\sigma_2 = 1\,\mathrm{nJ} + 10\%\,E_i \ . \tag{5.11}$$

In the experiment, the value of energy is calculated by the average of 10 points. The error of
energy is

$$\sigma_i = \frac{1\,\mathrm{nJ} + 10\%\,E_i}{\sqrt{10}} \ . \tag{5.12}$$
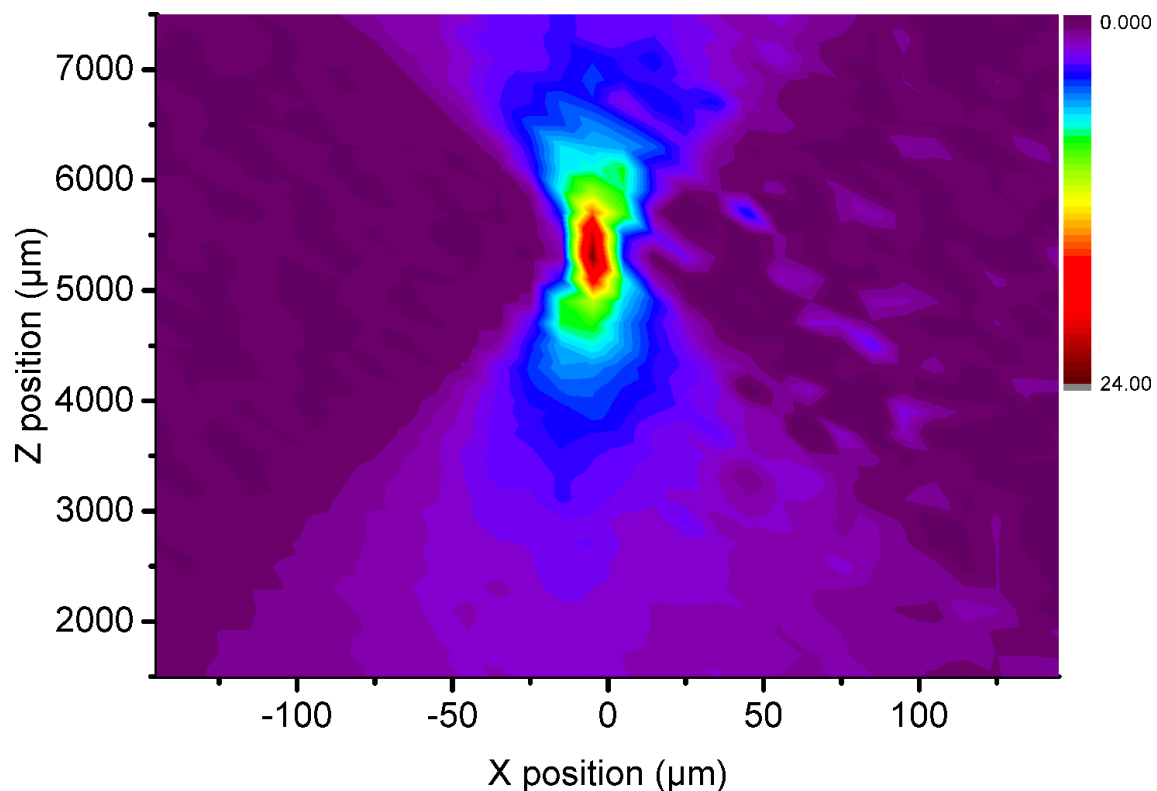
(i) Intensity map in large scale (x width = 10 μm)
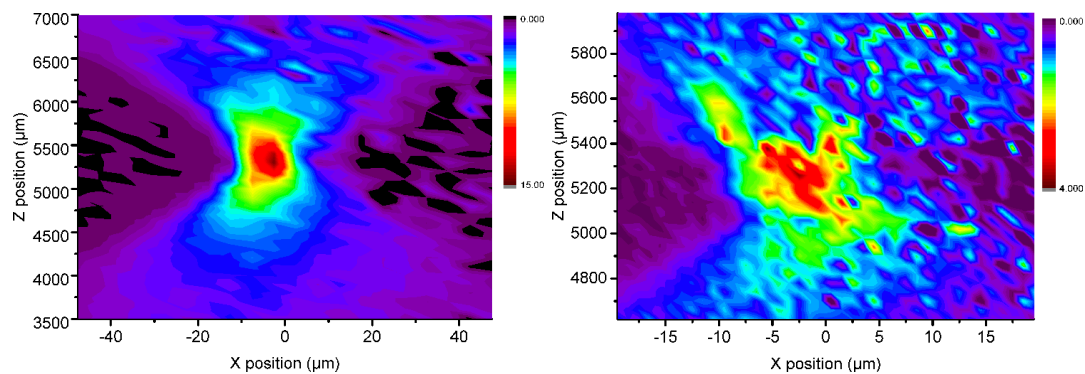
(ii) Intensity map in middle scale (x width = (iii) Intensity map in small scale (x width = 1 μm)
5 μm)

Figure 5.5: The laser intensity map combined from results of the energy scan
on different sections. The three intensity distributions are from the
same measurement with different pixel sizes, in order to accumulate
the figure of Gaussian beam in different resolution.

The error of the measured value E is:

$$\sigma_E = \sqrt{\sigma_1^2 + \sigma_2^2} \approx 4.35\% \, E + 0.23 \, \text{nJ} \, . \tag{5.13}$$

If the blade is placed at position X_i and X_{i+1}, and the measured value of energy is E_i and E_{i+1}, $e = \triangle E = E_{i+1} - E_i$, then:

$$\sigma_e = \sqrt{\sigma_{E_i}{}^2 + \sigma_{E_{i+1}}{}^2} \approx \sqrt{2\sigma_{E_{max}}{}^2} = \sqrt{2\left(\sigma_1^2 + \sigma_2^2\right)} \, . \tag{5.14}$$

where $\triangle E_{max}{}^2$ is the maximum value of $\triangle E_1{}^2$ and $\triangle E_2{}^2$.

Apply Equations (5.13), (5.11) and (5.12) for Equation (5.14), we have

$$\sigma_e = \sqrt{2} \, \sigma_E \approx 6.2\% \, E + 0.33 \, \text{nJ} \, . \tag{5.15}$$

If the edge is placed at the central position where $E_i = 25 \, \text{nJ}$, according to Equation (5.15), we obtain $\sigma_e = 1.88 \, \text{nJ}$, if we set the distance to be $1 \, \mu\text{m}$, around the beam waist, $e_i \approx 5 \, \text{nJ}$, which is only about three times more than the error. But on the other sections where e_i is not so high, the error is too large compared to the measurement value. This is the explanation of the very high fluctuations of laser energy in Figure 5.5(iii), and the main reason why it is not necessary to measure it with smaller steps.

It should be noted that, although the laser is very close to ideal uniform laser, there is still non-uniformity of spacial energy distribution. The non-uniformity will also contribute to the error in experimental results.

5.3   Characteristics of laser-ionization

5.3.1   Multi-photon process in ionization

As the laser pulse is focused into the gas medium, although the energy of a single photon is not above the ionization potential of the medium, there is a chance in dependence of the laser beam intensity, that a particle of the medium absorbs multiple number of photons and becomes ionized. During the ionization, the particle will be excited to different states until fully ionized. This is the multiphoton ionization effect (MPI) [95, 96, 97], which appears at the laser intensity in the order of $10 \times 10^{10} \, \text{W/cm}^2$. If the laser intensity is in the order of about $10 \times 10^{14} \, \text{W/cm}^2$, there is another effect called 'tunnel ionization' [98]. MPI physics is a wide field of laser and atom physics [99]. In this work, we work with the laser intensity of about $10 \times 10^{10} \, \text{W cm}^{-2}$. Therefore, we only need to consider the simple situation with only MPI.

The energy of a photon from the laser test facility is $E = h\nu = 4.82 \, \text{eV}$. The ionization energy of gases we use in all of our experiments are listed in Table 5.1. It can be seen that if the photons are absorbed by these gases for ionization, the number of photons required is three or four. The cross section σ_{MPI} of a MPI process absorbing $< n >$ photons can be described as:
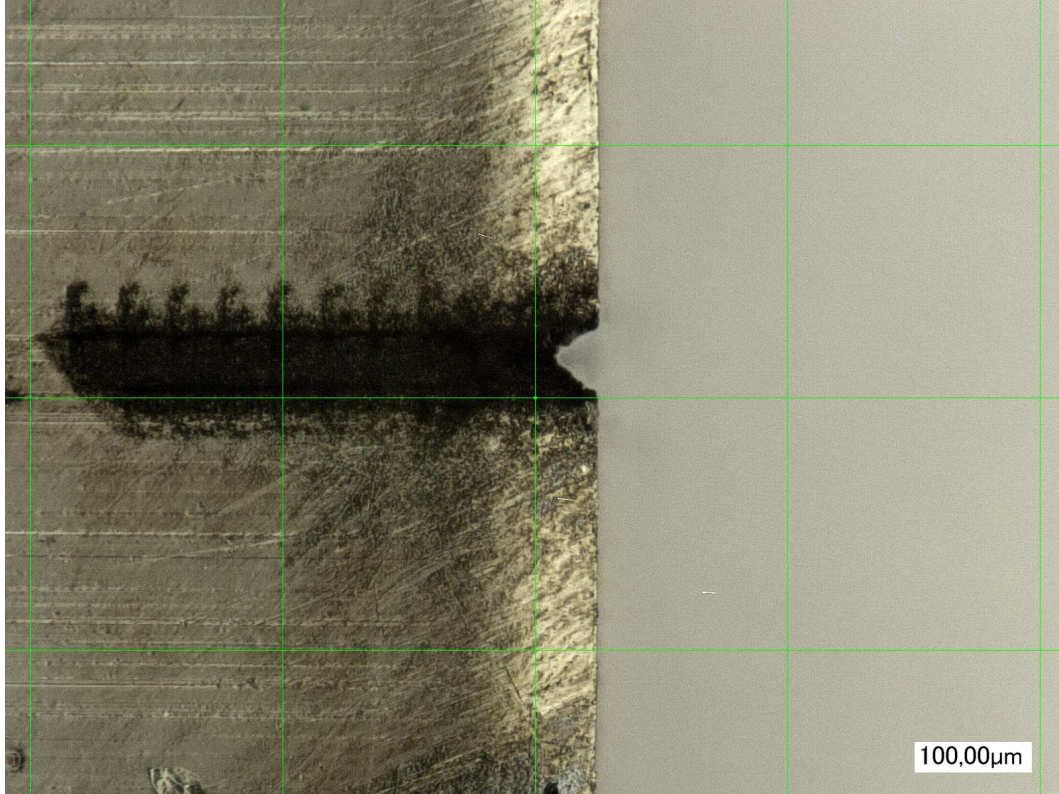
Figure 5.6: The picture of laser caused damage on a blade. The height and width of a cell are both $100\,\mu$m, plotted by green lines.

$$\sigma_{MPI} = \sigma_{0to1} \cdot \sigma_{1to2} \ldots \sigma_{<n-1>to<n>} \; . \tag{5.16}$$

The number of electrons in an ionization is:

$$N_e = \sigma_{0to1} \cdot I \cdot \sigma_{1to2} \cdot I \ldots \sigma_{<n-1>to<n>} \cdot I \; , \tag{5.17}$$

where I is the laser intensity. Because each σ is very small, the number of ionization should be very little if $<n>$ is three or four. It can be concluded that:

$$N_e \propto I^{<n>} \; . \tag{5.18}$$

The number of $<n>$ can be calculated by measuring the relation between laser energy per pulse and signal charge.

In other works, it has been discovered that in the gas of RPC detectors or wire detectors, the ionization does not come from the working gases, but from impurities with lower ionization potentials, like phenol and toluene [81, 82, 100]. We assume that in our experiment, the ionization also could be caused due to impurities instead of the detector gas, as we did not take special efforts to remove the very little residual content of the impurities.

Table 5.1: Ionization potentials

Detector	Gas	Ionization Potential eV	$<n>$ of MPI	$<n>$ Measurement
RPC	R134a	12.2	2.5	
	iso-butane	10.7	2.2	2.08 - 2.31
	SF_6	15.3	3.2	
Drift Tube	Ar	15.7	3.3	2.007
	CO_2	14.4	3.0	

5.3.2   Experimental tests

5.3.2.1   Experiment with drift tube

The drift tube is filled with 70% Ar + 30% CO_2. After careful calibration of laser position (the method is described in Section 5.3), the focus is placed on the position of $1000\,\mu m$ above the wire. The frequency of laser is set to $10\,Hz$ to avoid the influence of discharges. Behind the output window of the laser generator, an attenuator, namely 'round continuously variable neutral density filter', is mounted on a rotation stage. The attenuator is used to adjust the laser energy. The rotation stage is programmed so that it can rotate with $0.1\,deg$ which corresponds to an attenuation of $-53\,dB$, i.e. 0.2%. The decreasing factor of a specific angle of the round continuously density filter, the intensity is therefore controlled.

The voltage applied to the anode wire of the drift tube is set to normal working voltage of $1700\,V$. The pre-amplifier gain amounts to $20\,dB$. The signal charge is averaged over 1000 events.
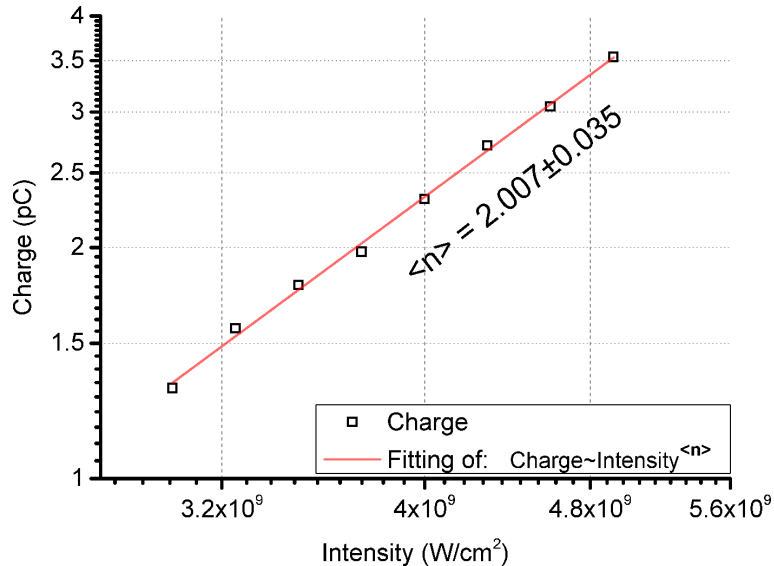
Figure 5.7: The average signal charge of the drift tube in dependence on the laser intensity in double log scale. The slope of linear fit represents the number of photons $< n >$ absorbed for an ionization of the residual gas molecules in the gas mixture according to Equation (5.19).

The signal is recorded by the data acquisition system, and the charge of the signal is proportional to the number of electrons. Results are plotted in double logarithmic scale in Figure 5.7. Because of the very high accuracy of laser energy control and signal analysis, the result of multi-photon ionization is $< n >= 2.007 \pm 0.035$. It is a proof that the ionization occurs at the impurities of large molecules in gas and not on CO_2 or Ar, since due to the values listed in Table 5.1 about the number of photons need to ionize different molecules in these gases.

5.3.2.2 Experiments with RPC

The charge-intensity experiment is also operated with the RPC detectors. The RPC sample in this experiment is assembled with glass electrode of $0.5\,mm$ gap width. The pre-amplifier gain amounts to $100\,dB$. The electric field is $50\,kV/cm$. The laser is focused into the gas gap of RPC, where the distance from laser focus to electrode is $100\,\mu m$ and the frequency of laser pulses is selected to 1.25, 2.5 and $5\,Hz$. In our experiments, the signal charge and frequency is far away from saturation point because the electric field is not very high. The signal charge is the average charge of 1000 signals.
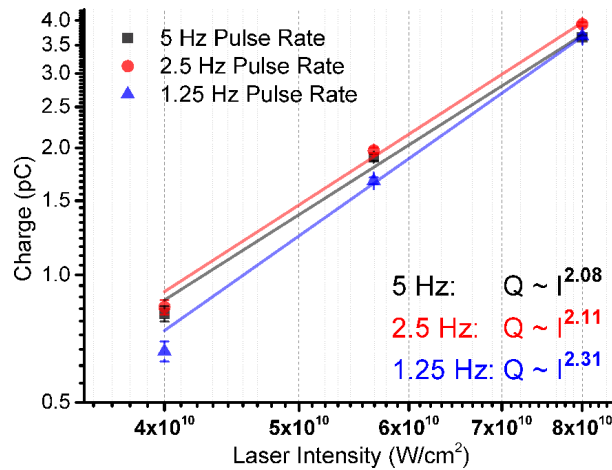
Figure 5.8: The average signal charge of RPC for different laser pulse intensities in double log scale. The slope of a linear fit will be the number of photons $< n >$ absorbed for an ionization process.

With different repetition rates of the laser, the number of photons absorbed in an ionization process is between 2.08 and 2.31, according to Figure 5.8.

As iso-butane with ionization potential of $10.7\,eV$ is in the gas component, it is also possible that the ionizations occurs not only on impurities, but also on iso-Butane molecules, as the ratio of iso-Butane is several orders of magnitude larger than impurities.

5.3.2.3 Stability test

In order to check the stability, a long-time measurement of signals is made. The system is set so that there are continuous stable waveforms in the detector. The time-scan function of automatic system is applied to record the time and charge of the signals within 24 hours. No ageing effect or fluctuations of waveforms are observed.

5.3.3 Conclusions

Tests on both drift tube and RPC detector are made for cross-checks. The experimental result shows that for both detectors, the number of photons absorbed in an ionization is around two, in agreement with [82].

A precise measurement of <n> is operated with the drift tube, and the results show that for the Ar-CO_2 gas mixture in the drift tube, the ionization occurs on the impurities. However, the results from RPC sample has shown a difference in the MPI power.

From the experimental results, it can be concluded that ionization occurs on the impurities with two-photon ionization. However, for iso-Butane, the required number of photons for ionization just exceeds two; and the concentration of iso-butane is much larger than impurities. So that it is also possible that iso-butane contributes to the ionization.

For the RPC detector, the situation is not fully clear. However, for the requirement of laser tests, there are no difference if the MPI factor is two or three. Having clarified that the photon absorption number is equal or larger than two is satisfactory

Despite that the ionization process is not fully understood, the objectives of stability of laser ionization is achieved. The experiments have shown that the two-photon ionization is the main process in both RPC and drift tube.

Clarifications of whether the ionizations can occur on the iso-Butane can also be operated, and the experiment could be arranged in the future.

5.4 Investigation of primary electron distribution

In Sections 5.1 and 5.3, the profile of Gaussian beam and two-photon ionization has been discussed. In this section, we will discuss how to calculate the experimental research result of the laser focus.

5.4.1 Calculation of electron spatial distribution

We use Equations (5.1) and (5.18) to calculate the number of electrons induced by a Gaussian beam in a multi-photon process:

$$N_e(z,r) = \sigma_{MPI}I^{<n>} = \sigma_{MPI}\left(\frac{2P}{\pi\, w(z)^2}\right)^{<n>} e^{\left(-\frac{2r^2<n>}{w(z)^2}\right)} , \qquad (5.19)$$

where z is the position of the point along laser beam Z axis, I is the laser intensity, σ_{MPI} is a constant of cross section, $<n>= 1, 2, 3\ldots$ is the number of photons required for an ionization, P is the total laser power and $w(z)$ is the beam radius. We combine this expression with Equation (5.2) to obtain:

$$N_e(z,r) = \sigma_{MPI}\left(\frac{P}{\pi}\right)^{<n>}\left(\frac{2}{w_0{}^2\left(1+\left(\frac{z}{Z_R}\right)^2\right)}\right)^{<n>} e^{-\frac{2r^2<n>}{w_0{}^2\left(1+\left(\frac{z}{Z_R}\right)^2\right)}} . \qquad (5.20)$$

As the beam radius is small compared to the scale of detectors, we can also simplify the 3D spatial distribution of electrons to a one-dimension distribution along the laser beam axis Z. Then, the number of electrons along laser beam axis Z is

$$
\begin{aligned}
N_e(z) &= \int_{\theta=0}^{\theta=2\pi} \int_{r=0}^{r=\infty} N_e(z,r) r \, dr \, d\theta = 2\pi \int_{r=0}^{r=\infty} N_e(z,r) r \, dr \\[2mm]
&= 2\pi \sigma_{MPI} \left(\frac{P}{\pi}\right)^{<n>} \left(\frac{2}{w_0{}^2\left(1+\left(\frac{z}{Z_R}\right)^2\right)}\right)^{<n>} \frac{w_0{}^2\left(1+\left(\frac{z}{Z_R}\right)^2\right)}{4<n>} \\[2mm]
&= \frac{\pi \sigma_{MPI}}{2<n>} \left(\frac{2P}{\pi}\right)^{<n>} \left(\frac{1}{w_0{}^2}\right)^{<n>-1} \left(\frac{1}{1+\left(\frac{z}{Z_R}\right)^2}\right)^{<n>-1} \\[2mm]
&= C(P, w_0, <n>) \left(\frac{1}{1+\left(\frac{z}{Z_R}\right)^2}\right)^{<n>-1} ,
\end{aligned}
\tag{5.21}
$$

where $C(P, w_0, <n>)$ is a constant related to P, w_0 and $<n>$. Then the FWHM of the one-dimension electron distribution can be calculated as:

$$
N_e(Z_{half}) = C(P, w_0, <n>) \left(\frac{1}{1+\left(\frac{Z_{half}}{Z_R}\right)^2}\right)^{<n>-1} = \frac{1}{2} N_{emax} ,
\tag{5.22}
$$

$$
\left(\frac{1}{1+\left(\frac{Z_{half}}{Z_R}\right)^2}\right)^{<n>-1} = \frac{1}{2} ,
\tag{5.23}
$$

$$
Z_{half} = Z_R \sqrt{\sqrt[<n>-1]{2} - 1} .
\tag{5.24}
$$

Considering Equations (5.21) and (5.24), we can further understand the ionization in our experimental setup. When <n> =1, N_e becomes a constant. If this is the case for a laser test system, the system will not be suitable for measuring the gas parameters in the gaps of a RPC detector, as electrons are generated all along the beam path. When <n> =2, the electron distribution becomes a Lorentz function (Cauchy function), and the FWHM of the electron Z distribution is equal to twice the Rayleigh length Z_R.

As we have proved that <n>=2 in the experiments in Section 5.3, we only need to focus on this value. As described in Equations (5.3) and (5.4):

$$
Z_R = \frac{\pi w_0^2}{\lambda} = \frac{\lambda}{\pi \theta^2} ,
\tag{5.25}
$$

$$w_0 = \frac{\lambda}{\pi \, \theta} \; . \tag{5.26}$$

From the Equations (5.25) and (5.26), it can be deduced that the width and length of the ionization area depends on the beam angle θ. For the test, we have limited the input beam radius to be $1\,\mathrm{mm}$. In detector test experiments, the adjustable diaphragm should be opened wider in order to reduce the volume of laser focus; on the other hand it cannot be opened too wide, as the laser beam has non-uniformities.

The calculation program described in Section 5.1 is further developed to calculate the spatial distribution of electrons. As we have already calculated the 'energy intensity'[2] in every element, and because of Equation (5.18), we can easily square or cube or power it by $<n>$, according to the number of photons in an ionization step. As it is already clarified that we are working with two-photon ionization in the drift tube, and all the parameters are taken from the parameters in calculations in Section 5.1, then the calculation of number of electrons E_{xyz} in an element is

$$N_{e_{xyz}} = \sigma I_{xyz}{}^2 \propto I_{xyz}{}^2 \; . \tag{5.27}$$

The two-dimension map of electron numbers is the projection of spatial electron distribution in XZ-plane, it can be calculated as

$$N_{e_{xz}} = \sum_y N_{e_{xyz}} \; . \tag{5.28}$$

Because we are interested in the one-dimension electron distribution on the Z axis, the number of electrons in an element is further summed as

$$N_{e_z} = \sum_x N_{e_{xz}} \; . \tag{5.29}$$

All these calculation are operated with the program code, and the two output files are data calculated for two-dimension map distribution and one-dimension distribution. The calculated data is plotted in Figure 5.9 It can be seen in 5.9(i) that the electrons are distributed in small region. Considering that the beam waist is about $4\,\mathrm{\mu m}$, the width of multi-photon ionization volume is only about 2 to $3\,\mathrm{\mu m}$. Also, the Lorentz fit in Figure 5.9(ii) is in agreement with our calculation: when $<n>= 2$, the FWHM of ionization distribution on Z axis is equal to $2Z_R$.

5.4.2   Experimental analysis

The experiment to investigate the size of laser focus is operated with the drift tube. In the previous tests in Section 5.3, we have proved the possibility of laser ionization and two-photon ionization. If we want to prove that the ionization is limited within a very small volume around the laser focus, we should change the position of laser focus and check whether the drift time is changed while the drift length is different.

In the experiment, the intensity of laser is kept constant. The drift tube sample is assembled on the step-driver support, the three-dimension scanning is provided by remote control. When we change the position of detector, the relative position of laser focus is changed inside the gas. As the drift length is changed, the drift time is therefore changed, so that we can observe a shift

---

[2]It represents the laser intensity at a position, but has no actual physical significance.

(i) Electron distribution in 2D map

(ii) Electron distribution along the beam
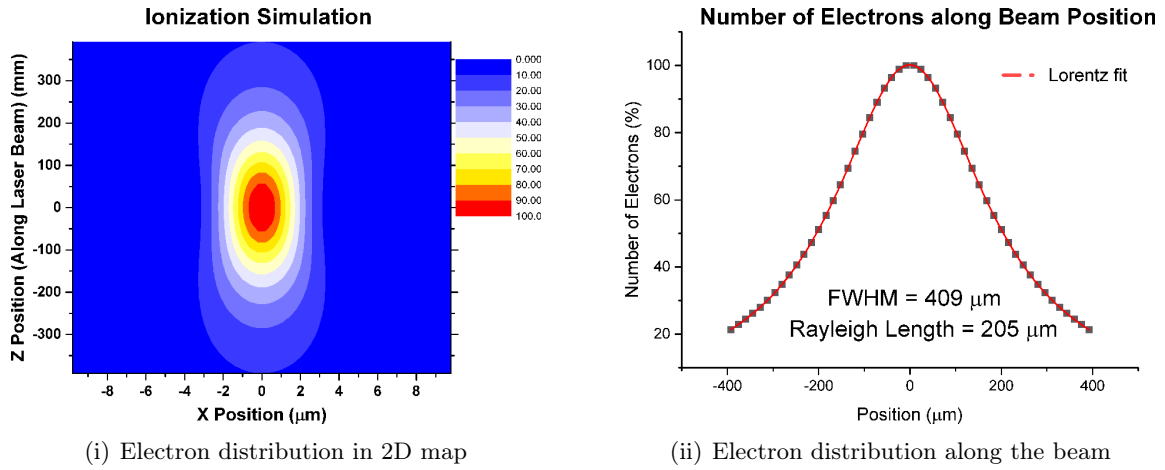
Figure 5.9: 2D and 1D distribution of electron emitted from ionization calculated by finite element analysis. The 1D figure is fitted with Lorentz Function.

of time of the signal. The laser repetition rate is 10 Hz, working gas is 70% Ar + 30% CO_2 and high voltage of the drift tube is 1700 V.

The experiment is based on multiple tests. First we need to operate calibration tests to understand and adjust the working condition of detector and facility, and the approximate value of parameters. After the pre-works, the position of laser focus is obtained, and the main test can begin.
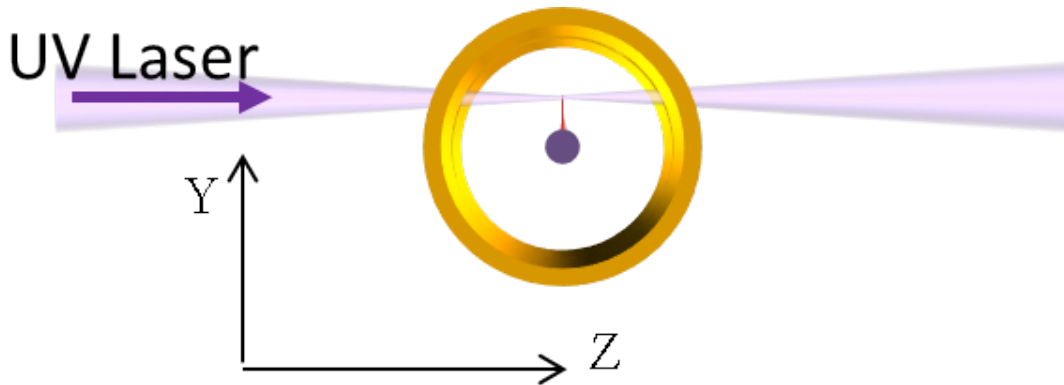
Figure 5.10: The definition of axes in test: Z is the direction along laser beam line, Y is the vertical direction along the slit and perpendicular to the anode wire.

The calibration test is operated in this way:

- First, adjustment of X, Y and Z positions are taken, so that the laser focus is placed inside the slit of the cathode cylinder, and meanwhile the laser is detected by the laser sensor placed behind the detector box. It is then adjusted in a more precise way to make sure laser does not touch the edges of tube.

- Second, the high voltage of the drift tube is applied to the anode wire and the readout electronics are turned on. The position of laser focus is adjusted slightly until signal waveforms appears on the oscilloscope. With the fine adjustments in step.1, the signal is usually easy to find, and the most important work in this process is to adjust the laser, the detector and the associated electronic sto reach a stable working condition.

(i) Scan of Z axis when $Y = Y_0 + 1000\mu m$

(ii) Scan of Y axis when $Z = Z_0$
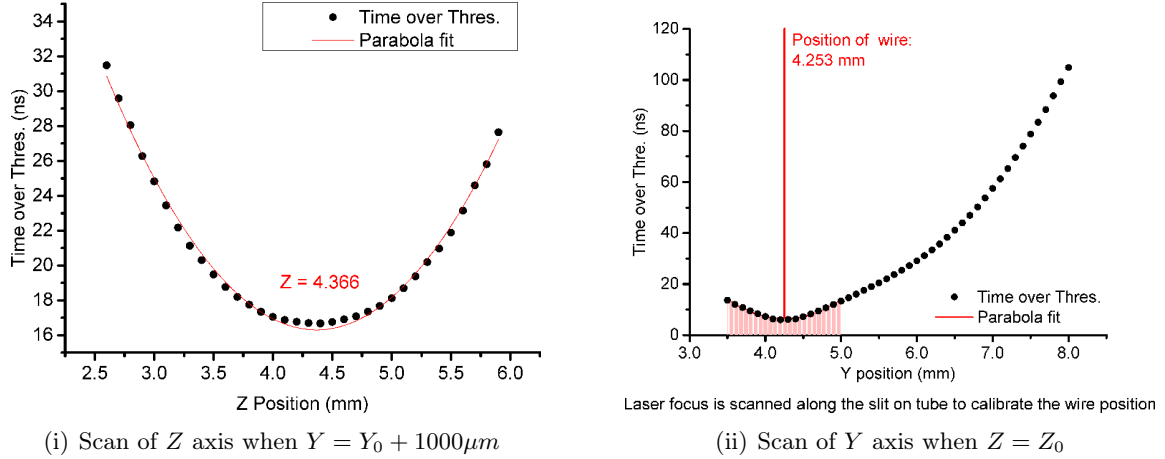
Figure 5.11: Time over threshold in dependence of the focus position tested with the drift tube. The position of the detector box is changed with the 3D-step driver to calibrate the focus position in relation to the anode wire. Figure 5.11(i) is along the Z axis, Figure 5.11(ii) is along the Y axis. The layout of axes are shown in Figure 5.10. The error of the measurement value is in the order of picoseconds.

- Third, the automatic program is called to make a scan on Z axis. The drift time in dependence of the position is acquired. If it is plotted in a figure, a parabola shape will be shown, see Figure 5.11(i). The value of Z where the drift time is at minimum of the parabola shape is the rough Z position of the focus, recorded as Z_0. In order to save time, the step length is usually set 1000 µm, and the scan range is full range of the step driver, from 0 to 8000 µm.

- Last step, the automatic program is called to make a scan on Y axis when $Z = Z_0$, and the drift time will also provide a parabola shape as the wire is exposed to the slit, but this parabola shape is cut when the laser beam is outside the slit. The distance from laser beam to the anode wire Y_0 is therefore obtained, where Y is the minimum value.

After calibration, the focus is placed in specific positions for different tests. Similar as the calibration test of Z position, the focus is now placed at $Y = Y_0 + 1000\mu m$, and the program is called to scan with small steps of 100 µm on Z direction. The position of Z_0 obtained from this test can be more accurate than that from the calibration test. With the same method, Y_0 is also updated by placing the focus at $Z = Z_0$ and scan over Y axis with small steps of 1000 µm. The results obtained in these experiments are plotted in Figure 5.11. The values of drift time is the average time difference between time over threshold of signal and reference time from laser of 1000 events.

The time resolution of reference time from the laser is around 1 to 2 ps, it is about two orders of magnitude less than the FWHM time resolution of the measured signal, so that the time resolution of reference signal can be ignored.

In order to investigate the properties of the test system, histograms of time and charge distribution are obtained at the point where $(Y = Y_0 + 2000\mu m, Z = Z_0)$ for 10000 events. The histograms are shown in Figure 5.12. FWHM time resolution is 220 ps while the relative deviation of charge is 5.8%. Considering that the fluctuation of laser intensity is about 3%, it can be concluded that the number of electrons from ionization is also stable. The variance of the number of electrons should also be between 3% and 5.8%, according to experimental results.

(i) Time resolution.

(ii) Charge distribution.
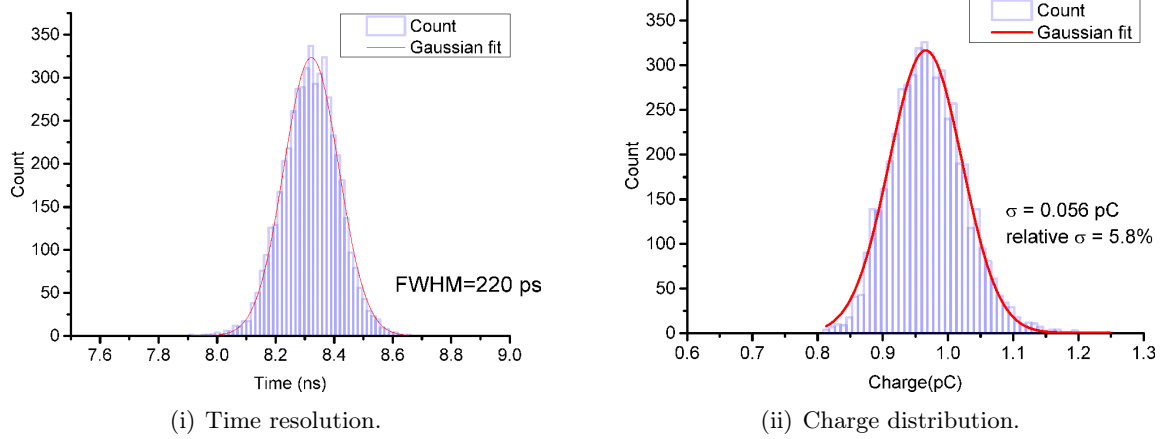
Figure 5.12: The time and charge distribution of signals in laser tests with the drift tube detector at normal working condition. The figures are taken where $Y = Y_0 + 1000\mu m$ and $Z = Z_0$.

(i) Scan of Z axis when $Y = Y_0 + 1000\mu m$

(ii) Scan of Y axis when $Z = Z_0$
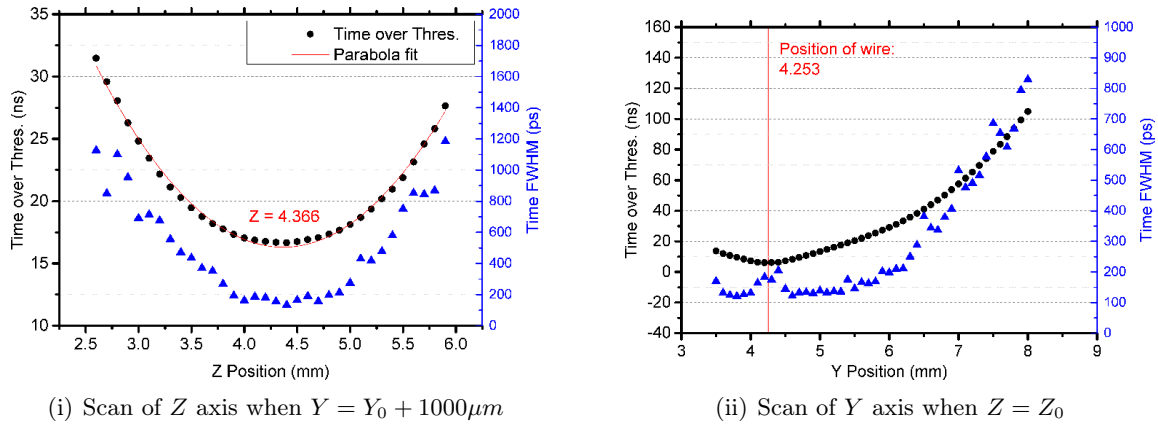
Figure 5.13: The scan of time (Difference between the time over threshold and the reference time from laser) and FWHM time resolution of the drift tube. The error of the measurement value is in the order of picoseconds.

For each measurement point in Figure 5.11, the time resolution has been obtained The results are plotted in Figure 5.13.

It can be seen that when the focus is placed closer to the anode wire, FWHM of time becomes smaller. This can be explained that when the electrons are drifting towards the wire, there is a time shift, the longer the drift distance, the larger the time shift. The minimum FWHM time resolution is around 120 to 150 ps, and the maximum FWHM is around 1 ns. It should be noted that the time resolution of a general drift tube is in the order of $\sim$ns, which is worse than the drift tube sample operated in laser test facility.

If the Y positions are Y_i, $(i = 0, 1, 2, \ldots, n)$, the time measured on position Y_i is t_i, then the drift velocity $v_{i.5}$ around position $\frac{Y_i + Y_{i+1}}{2}$ is calculated by:

$$v_{i.5} = \left| \frac{Y_{i+1} - Y_i}{T_{i+1} - T_i} \right| . \tag{5.30}$$

The electron drift velocity v in dependence of the distance to wire is shown in Figure 5.14 and be compared by a Magboltz simulation. From the figure we can see that the measurement value of
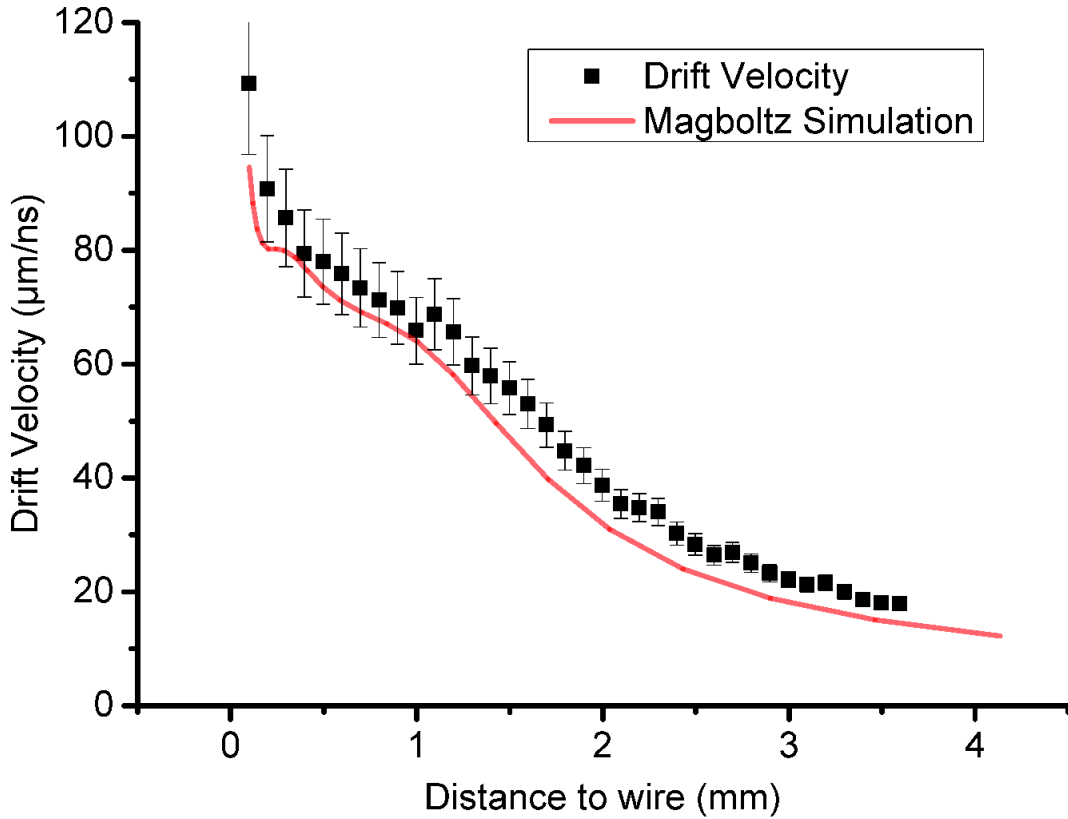
Figure 5.14: Drift velocity and its comparison to the Magboltz simulation on
different distances to anode wire.

drift velocity is within 10% difference compare to Magboltz simulation. Yet when the position is
getting closer to the wire, the error becomes larger because the time difference becomes too small.
If we are working with smaller steps, the error would be extended because of the systematic error
from time shift.

As a conclusion, the experiment has proved that the laser ionization is limited to a small
volume at the laser focus, an the number of electrons are stable.

5.5   Number of ionization in a laser pulse

The initial number of primary electrons is observed with drift tube and be compared to an ^{55}Fe
source.

The characteristic energy of X-rays from an ^{55}Fe source is $5.9\,\text{keV}$ with the activity of approx-
imately $4 \times 10^5\,\text{Bq}$. The X-ray ionizes the gas molecules, and the electron generated by photon
absorption will keep losing energy and ionize other molecules. The effective average ionization
energy to produce one electron-ion pair is $26\,\text{eV}$ for Argon and $33\,\text{eV}$ for CO_2, respectively. A
photon from ^{55}Fe will ionize total number of approximately 200 electrons with primary and
secondary ionizations.

As a proportional detector, a drift tube has very long drifting path. Except for the electron
amplification area, the signal charge is proportional to the number of primary electrons where

the electrons are located. The detector is filled with 70% Ar + 30% CO_2. Output signals are amplified by a 10 dB pre-amplifier. High voltage of the drift tube detector is taken as a variable with step of 50 V.

The first experiment is operated with the ^{55}Fe source. A thin Kapton foil (polymide) is assembled on the window of the drift tube to allow X-rays to pass though the detector box window instead of the 1 mm thickness quartz glass window. The ^{55}Fe source is placed directly on the window to achieve a maximum counting rate. During the experiments, the average counting rate of signal is about 1 to 2 Hz. The average signal charge is measured at different high voltages.

Then the polymide foil is removed from the detector window and the 1 mm thickness UV-anti reflection film quartz glass is assembled. Then focus position is calibrated with the same procedure as in Section 5.4. The laser focus is placed above the wire, with the distance of 1500 µm. While the laser intensity changes, the average charge of signal is recorded. For each value of high voltage in the experiment of ^{55}Fe source, the signal charge is measured for eight different intensities.
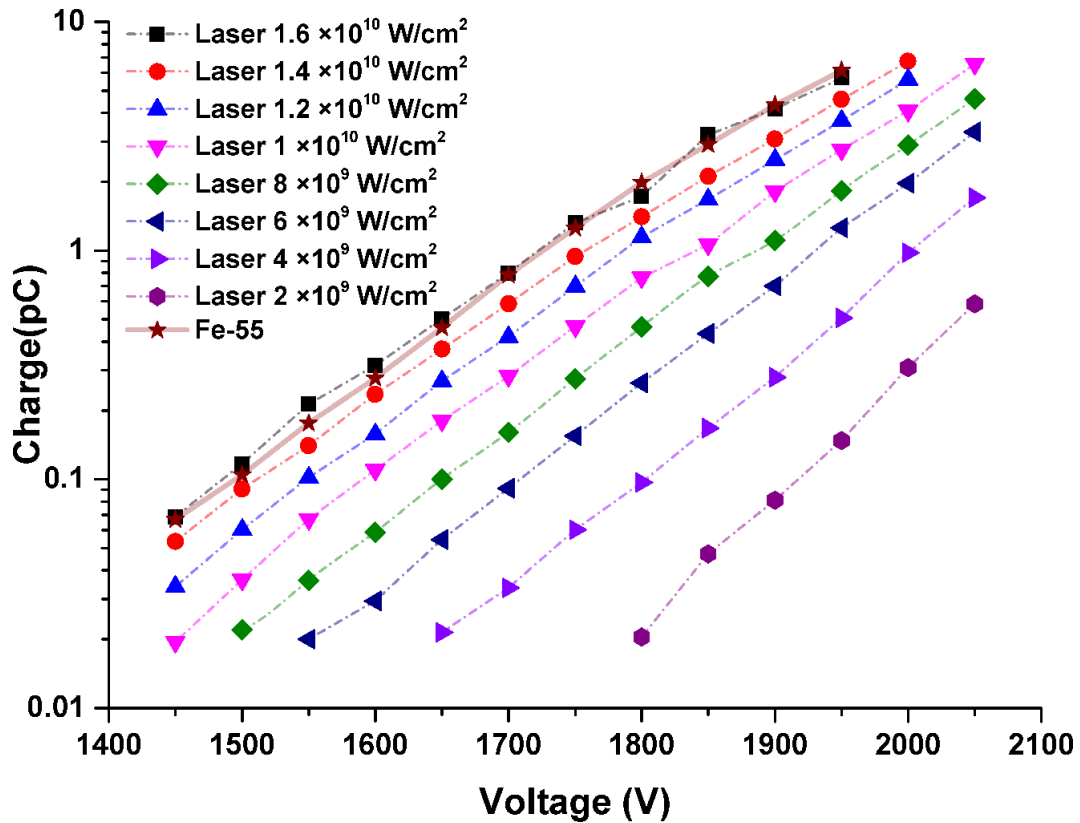
Figure 5.15: The charges of signals generated by laser and by ^{55}Fe source in the drift chamber detector in dependence on the anode voltage in a wide range of laser intensity. The laser intensity is the average laser intensity at the section of beam waist.

The experimental data is plotted in Figure 5.15. It can be observed that the number of electron emitted from ionization by X-rays from ^{55}Fe source and by 1.6×10^{10} W/cm^2 laser is comparable in the specific experimental condition of the calibration test. The high voltage of detector does not make a difference between the experimental results from two kinds of ionization sources. 1.6×10^{10} W/cm^2 intensity is about 40 nJ/pulse. In the experiments, most of the time the energy of laser is below 20 nJ/pulse.

Yet there are no certain relations between average signal charge and laser energy with dif-

ferent experiments. The laser system requires alignment from time to time, and as is described in Section 5.4, the number of electrons is extremely sensitive to the parameters of laser focus. On the other hand, although it is not possible to directly compare the different experiments, the performance of the whole laser test facility is very stable within one or more experiments in about two weeks.

5.6   Conceptions about number of electrons

The number of primary electrons generated from a laser pulse near focus should be carefully controlled, as it will influence the signal development and final result in two different ways:

- All detectors have a saturation effect if the signal charge is too large. In all of our experiments, the saturation effect should be observed with every different experimental setups, and the results must be taken in the range where saturation effect does not exist.

- On the other hand, if the number of primary electrons is too small, relative deviation of charge will be larger as the number of electrons follows Gamma distribution. The Gamma distribution is found in [6, 5], because the measurement are made with very small number of primary electrons.

In the experiments of this thesis, the primary number of electrons is usually very small. The number is controlled between 10 and 100, in order to reduce the statistic fraction of signal charge. As is described in Section 5.4.2, although the exact number of primary electrons cannot be measured, the experimental requirement of stability has been satisfied.

Chapter 6

Experimental study on gas parameters with RPC

In this chapter, we will present the experimental methods, process and results of gas parameter test with RPC detector on the laser test facility.

The laser test facility is a very unique device because it is the only device as far as we know at present, that is able to acquire the waveforms on different positions inside the RPC and have them compared. The challenges are from different aspects:

- A very high precision is needed so that the position of ionization can be controlled within the sub-millimeter gas gap of RPCs.

- Diameter of the ionization volume must be at least one order of magnitude smaller than the scale of a RPC gap which is sub-millimeter.

- The whole system must be controlled by program, as the workload will be too high for manpower. The requirements are all satisfied in the situation of HZDR laser test facility.

The series of experiments starts from a well measured and well calculated working mode of RPC: trigger RPC, to check whether our system and methods are well implemented and are able to acquire experimental results. The feasibility test is successful: in the trigger RPC region, the experimental results are in agreements with the experimental results by other groups.

Then our own discovery starts: with the increased field strength beyond trigger RPC and below timing RPC, the gas parameters in a wide range are measured. In this region, measurement of the gas parameters is successful, but the parameters begin to separate from the calculation values.

Finally, the measurement in the field strength of timing RPC is performed. The effective Townsend coefficients are measured on two different RPC detectors respectively. The obtained effective Townsend coefficients are much smaller than predicted from calculations, but the drift velocity is in good agreement.

6.1   On the field strength of trigger RPC

Our experiment starts from the trigger RPC. The field strength of trigger RPC is usually set to a value, which is not too much higher than the field strength that the avalanches begin to appear. If the field strength is below this value, the attachment coefficient will be higher than the first Townsend coefficient and there will be no charge amplification.

For example, in the calculation results in Figure 6.1 [2], it can be seen that the field strength where avalanche starts is about $41\,\mathrm{kV/cm}$ for the gas mixture of 96.7% Freon + 3% iso-Butane + 0.3% SF_6. The working field strength for trigger RPC is usually around $50\,\mathrm{kV/cm}$.

The RPCs in ATLAS trigger system [35] has about $45\,\mathrm{kV/cm}$ field strength, and RPCs in ALICE Muon Trigger System has $50\,\mathrm{kV/cm}$ to $52\,\mathrm{kV/cm}$ [101]. The width of gas gap of trigger RPC is about 1 to $2\,\mathrm{mm}$, in order to have enough signal charge and efficiency. For example in ALICE Muon Trigger System the gas gap is $2\,\mathrm{mm}$, and the efficiency is beyond 95% when the field strength is beyond $50\,\mathrm{kV/cm}$. Although the gas mixtures differs in the experiments, the value of field strengths are similar because small difference in the fraction of Freon or iso-butane does not influence the gas performance too much.
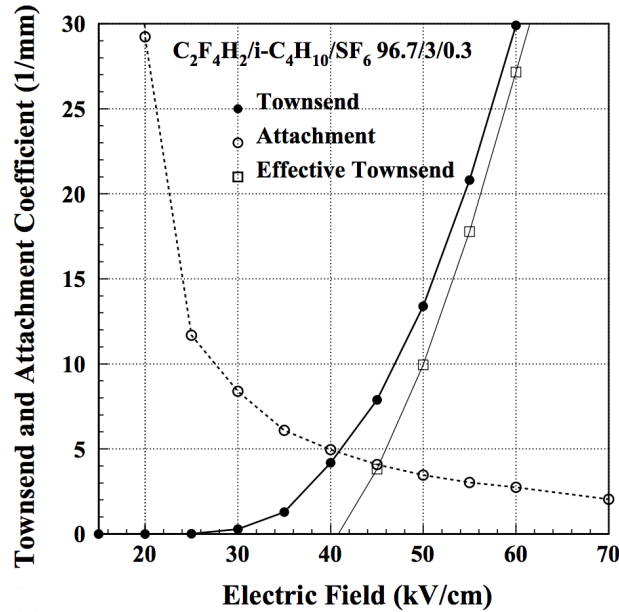
Figure 6.1: The simulation results of Townsend coefficient, attachment cofficient and effective Townsend result for trigger RPC gas mixtures and field strengths. Figure from [2].

As is introduced in Section 4.2.3, there are existing measurement of gas parameters in the field strength of trigger RPC at atmospheric pressure. Because of such experiments, the gas parameters in this environment can be regarded as known value. In order to test the performance of HZDR laser test facility, the gas parameters for trigger RPC should also be measured and compared to existing results to check the validity of methods and setups.

6.1.1   Experimental setup and methods

In the first experiment, the glass RPC samples are taken because RPC detectors with glass electrodes are widely used, so that the signals and rate performance can be compared to well know parameters of RPCs.

RPC samples with $1\,\mathrm{mm}$ gas gap and $0.5\,\mathrm{mm}$ gas gap are mounted in different terms of tests respectively. To set the field strength inside the gas gap at $50\,\mathrm{kV/cm}$, the high voltage supply for the RPCs should be 5.0 and $2.5\,\mathrm{kV}$, respectively.

The gas mixture in the tests of trigger RPC is 94.7% Freon + 5% iso-Butane + 0.3% SF_6, the same gas as reported in [6]. The flow rate of gas is $20\,\mathrm{mL/min}$. The rate of laser pulses is $2.5\,\mathrm{Hz}$, and the laser intensity is tuned to $2 \times 10^8\,\mathrm{W/cm^2}$. The other parameters are introduced in Section 4.4.

The laser system is aligned until we have a stable and sharp laser focus, which usually does not require any more alignment if there are no shaking or hitting within two to three weeks. Then the detector is implemented, and the automatic process to calibrate the position of laser focus inside the detector is applied. After the position is precisely calibrated, the laser focus is placed in a certain position of the gas gap, depending on the experimental objectives.

Then the laser is blocked and the high voltage of detector is increased carefully to make sure there is no breakdown of voltage. If the dark current is low enough, the next step is to increase the laser energy by turning the attenuation wheel until obvious signals are shown in the oscilloscope.

With the preparation, the test can be started. Scan range and step number are input parameters of the auto scan system, and despite the checking process, the system can be left running until the completion of data taking.

Finally, the experiment data is analysed to accumulate the gas parameters.

6.1.2   Data analysis and discussion

Very close experimental results for the RPCs with different gap width on several positions are obtained. Considering that the wider gap contains wider range of positions, all experiments are operated with the glass RPC with $1\,\mathrm{mm}$ gas gap.

This measurement is operated with different voltages around $50\,\mathrm{kV/cm}$ to make a scan of gas parameters.

6.1.2.1   Waveforms and determination of time

An example of measurement and analysis method is presented in this section.

For the $50\,\mathrm{kV/cm}$ measurement, the distances from the laser focus to anode is from $50\,\mathrm{\mu m}$ to $550\,\mathrm{\mu m}$, with the step length of $10\,\mathrm{\mu m}$. On every measured positions, 300 waveforms are acquired. The waveforms are averaged and then be plotted in Figure 6.2.

From the figure it can be seen that the averaged signal waveforms are regularly distributed. Because that the stability of laser intensity is very high, the variation of number of primary electrons is also very small. As the random noise is well reduced, the waveforms have clear layers even the distance between each point is only $10\,\mathrm{\mu m}$.
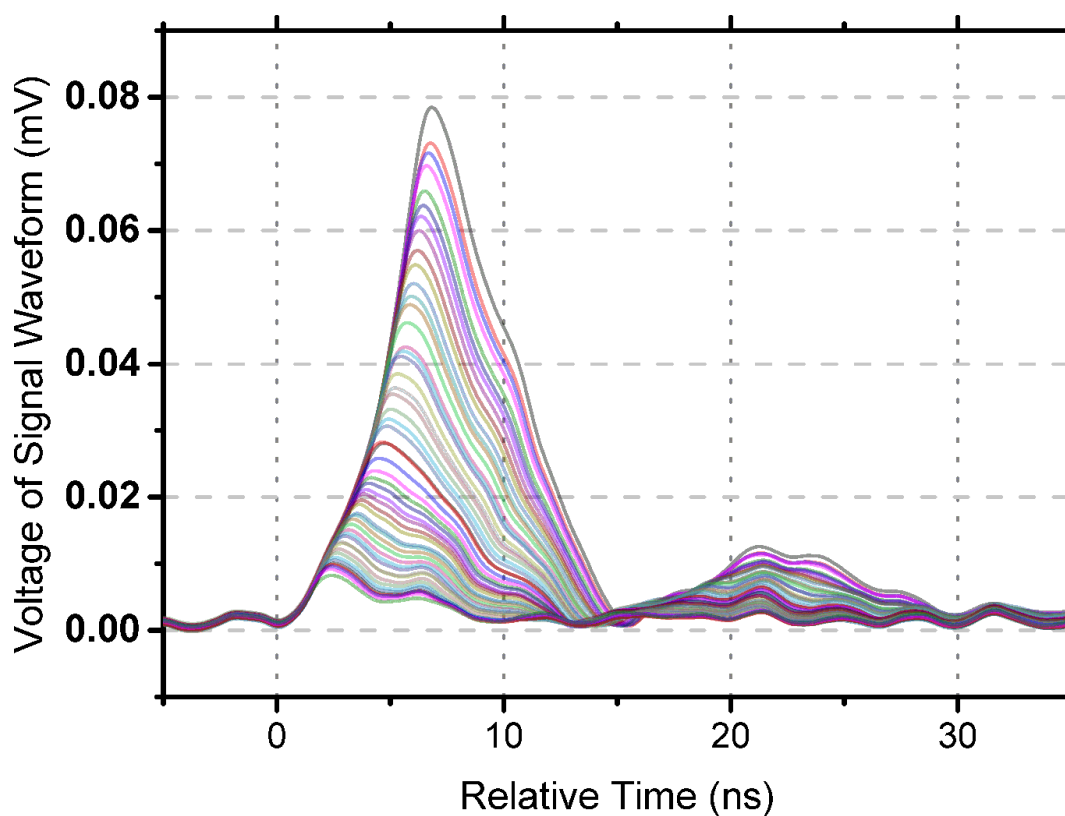
Figure 6.2: The time dependence of signal amplitude of all drift lengths in the step length of $10\,\mu m$ from $50\,\mu m$ to $550\,\mu m$ for a constant laser energy. Each waveforms are averaged from 1000 waveforms of a certain drift length. The RPC sample is glass electrode RPC with $0.5\,mm$ gas gap. The field strength is $50\,kV/cm$.

(i) Time distribution and resolution of RPC   (ii) Charge distribution of RPC
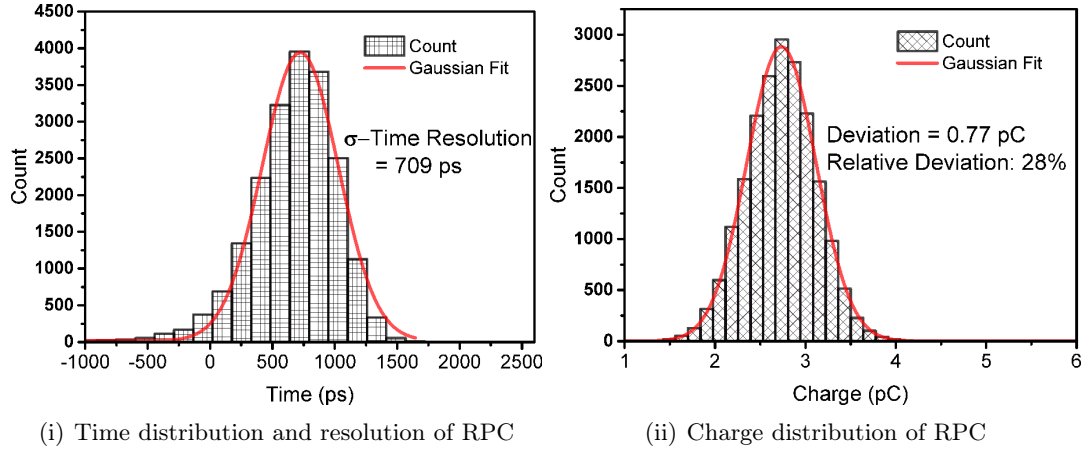
Figure 6.3: The time and charge histogram of RPC with $1\,\mathrm{mm}$ gas gap and $50\,\mathrm{kV/cm}$ field strength. The electrodes are float glass. Laser is fixed on the position where the drift length is $300\,\mathrm{\mu m}$.

The waveforms follows a clear pattern: rising part of all waveforms are overlapped, which means if a researcher sets an absolute threshold to measure the time, there will not be possibility to see the difference as the rising slope are overlapped. On the other hand, if a threshold that is relative to the amplitude of the signal is set, difference of time over threshold will appear.

Finally, in the analysis program, when calculating the time over threshold, the threshold mode is chosen to be relative threshold. For the calculation of signal charge, as the peaks of signals are well limited in a time window that is visible on the figure, the time window is manually set to contain the whole signal pulse.

6.1.2.2 Time and charge distribution

As is discussed in Section 4.4.2, Section 5.4 and Section 5.4.2, the laser energy has a very stable pulse energy with fluctuation less than 3%, and the experimental results from drift tube has shown that the fluctuation of primary ionization is around 5.8%. It can be inferred that the number of primary electrons in a RPC detector sample is also stable, with fluctuation on the same order of the result measured by drift tube.

The time resolution and charge distribution is shown in Figure 6.3(i) and Figure 6.3(ii). The time resolution is around $700\,\mathrm{ps}$, which is comparable to the real trigger RPC with time resolution of around $1\,\mathrm{ns}$. The relative charge variation is 28%.

The variance of 28% is larger than the variance of 3% to 5.8% obtained from drift tube. The possible explanation of the difference is that the laser intensity for RPC test is much smaller than for drift tube test. As the number of primary electrons becomes less, the statistics variance of number of electrons in RPC test, is much larger than in drift tube test.

6.1.2.3 Relation of amplitude and charge

For this experiment, it has been observed that the amplitude and signal charge are in proportional relation, shown in Figure 6.4. This can lead to a conclusion that for the tests of RPC charge, it is likely that the total charge has a linear relation to the amplitude. In this case the

total charge will be the only concern in the experiments of trigger RPC.
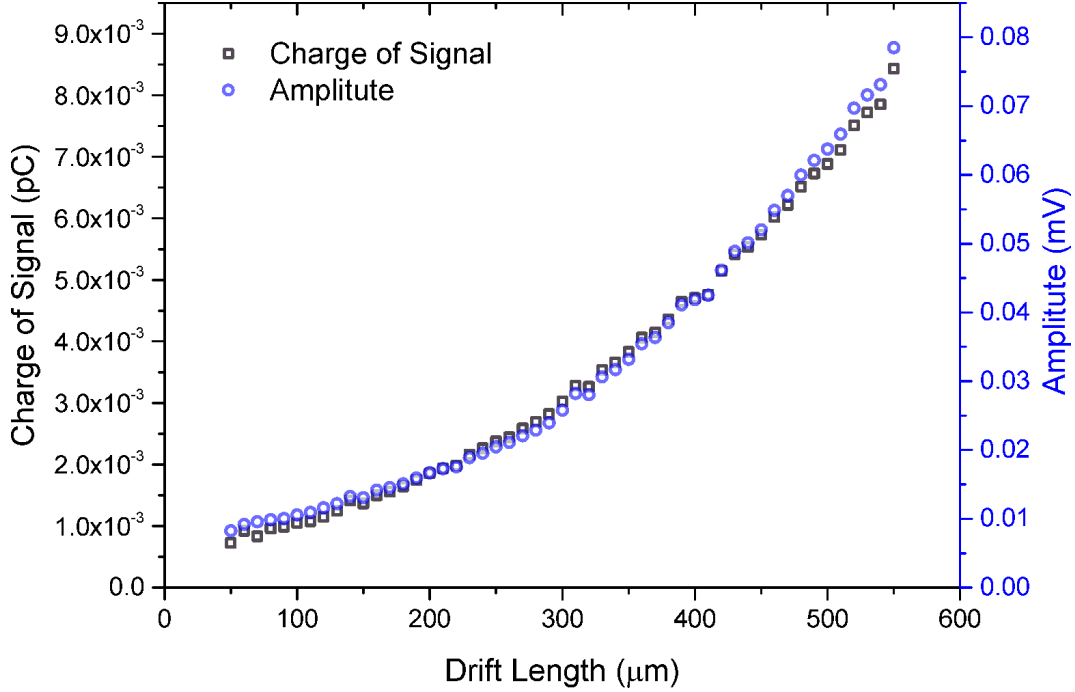
Figure 6.4: Amplitude and charge in dependence on the electron drift length in trigger RPC. This figure has shown that the charge and the amplitude is equivalent when calculating the effective Townsend coefficient in the RPC detector. The field strength is $50\,\mathrm{kV/cm}$ for this figure, the gas mixture is normal trigger RPC gas mixture of 94.7% Freon $+ 5\%$ iso-Butane $+ 0.3\%$ $\mathrm{SF_6}$, the laser beam intensity amounts $2 \times 10^8\,\mathrm{W/cm^2}$.

6.1.2.4   Data selection

The measurement is operated in a very wide range of distances of laser focus to anode. Because of the very high amplification with an effective Townsend coefficient of approximately $100\,\mathrm{cm^{-1}}$, the difference between maximum and minimum charge acquired from avalanche signal can vary by two to three orders of magnitude.

The lower limit of charge measurement is mainly determined by the background noise in the waveform. In the test, the signal waveforms on the oscilloscope has shown approximately $\pm 4\,\mathrm{mV}$ when the amplification factor of the pre-amplifier is $40\,\mathrm{dB}$. If the height of the peak is comparable to the noise, then the accuracy of the measurement will be decreased. In the data analysis, the time resolution of signal is greatly influenced by the noise when the amplitude of peak becomes lower than about $10\,\mathrm{mV}$. As a conclusion, for accumulation of the gas parameters, the charge data when the reduction of time resolution appears should no be taken into analysis.

The upper limit of the measurement is much easier to observe because of saturation effect. The saturation effect can be either from electronic system or from the detector. From our waveforms, it is impossible to distinguish the cause of the saturation effect. However, even saturation effect appears, the time resolution accumulated from absolute set of threshold is not influenced.

6.1.2.5 Measurement of gas parameters

The effective Townsend coefficient and electron drift velocity in trigger RPC with gas mixture of 94.7% Freon + 5% iso-Butane + 0.3% SF_6 is accumulated by experimental data on varies field strengths near 50 kV/cm on the laser test facility.

The experimental results are shown in Figure 6.5 and Figure 6.6. The figure has shown that the effective Townsend coefficient and drift velocity increase as the field strength becomes higher. When setting the relative threshold, the intention is to measure the time where the waveform has reached the maximum value, however, because of the possible fluctuations of signal which will result in a variation of the time of maximum voltage, setting the relative threshold to be 99% is the solution. With the 99% threshold, the result of time is very close to the time of maximum value and with smaller variation.
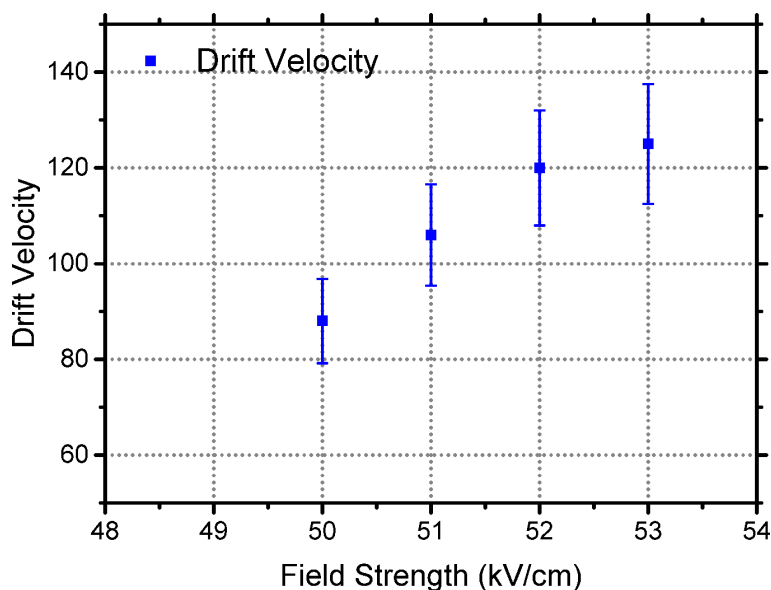

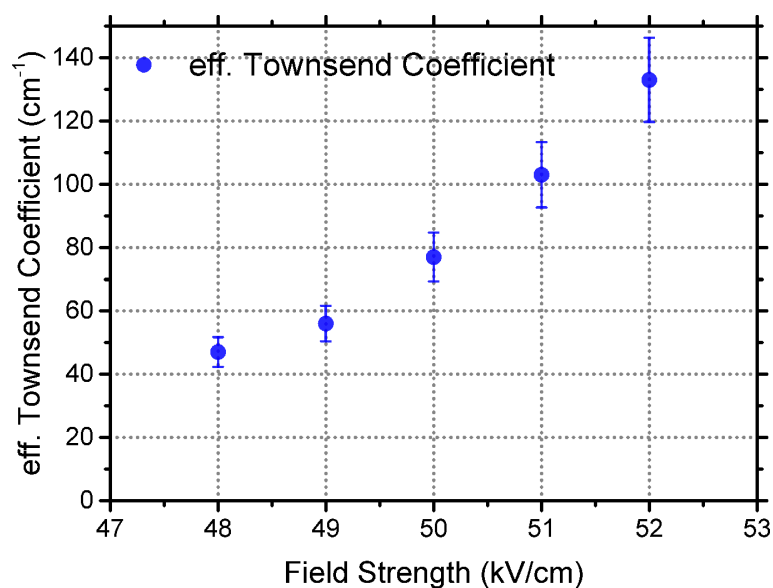Figure 6.5: Electron drift velocity as a function of field strength. The threshold is set to 99% of signal height.

Figure 6.6: Townsend coefficient as a function of field strength.

6.1.3   Comparison to existing results

A comparison of the gas parameters measured by HZDR and from other works is necessary to investigate the validity of the system and methods. The simulation and experimental results in [2, 5, 6] are of high correlation of the measurement operated by us, so that it is necessary to make a careful comparison between different works.

6.1.3.1   Difference in experimental setup

Consider the UV laser test of RPC detector in trigger RPC mode described in [5, 6] and HZDR experiment, the common components of the test systems are similar.

On the other hand, it is very important to investigate the difference of experimental devices between different works. The influence of characteristics of laser and components of gas mixture on the ionization process and experimental results should be investigated for a more comprehensive comparison.

A detailed comparison of HZDR experiments to the former results in [6, 5] is shown in Table 6.1. The main difference of laser characteristic from HZDR measurement and the other two measurements is that the wavelength of HZDR laser test facility is smaller so that the photon energy is higher. And the beam angle of HZDR test is one order of magnitude larger. As discussed in Chapter 4, larger beam angle will result in larger central laser intensity. The pulse duration of HZDR test is two orders of magnitude less than the other experiments; also, consider that the pulse duration of a signal is around 10 ps, they are all much less than the pulse duration of signals.

The deviation of charge distribution in HZDR test and [5] are in the same order, and differs from [6]. Although the main reason is the beam angle, there are several possibilities to explain the differences, such as differences in photon-absorption-section for different energies, or concentration of gas impurities. As a conclusion, the performance of laser test for RPC can differ as the experimental setup is different. For the case in this thesis, the number of primary electrons should be on the same order of [5], and larger than [6].

6.1.3.2   Comparison of results

The measurement results of gas parameters with HZDR laser test facility are compared to [64, 6] for investigation of validation.

In [64], the detector physics of RPC detector is described in detail, and the gas parameters of different RPC working gas, which is 96.7% Freon + 3% iso-Butane + 0.3% SF_6 for trigger RPC and 85% Freon + 5% iso-Butane + 10% SF_6 for timing RPC are calculated respectively. The simulation is operated with Magboltz program.

In [6], the component of gas mixture is 94.7% Freon + 5% iso-Butane + 0.3% SF_6, and this is also the gas mixture in HZDR test. As is already discussed in Section 6.1.3.1, the differences in photon energy, pulse duration and beam angle result in a difference of charge distribution, but their influence on measurement of gas parameters is small.

The data from [6, 64] and HZDR data are presented in Figure 6.7.

			Chiodini et al. [6]	Colucci et al. [5]	HZDR data
Laser	Wavelength	nm	337	337	257
	Photon energy	eV	3.8	3.8	4.8
	Pulse duration	ps	≤ 700	300	2
	Beam angle	mrad × mrad	1.2 × 1.7	2 × 3	30 × 30
	Energy per pulse	J	$\geq 100\,\mu J$	$40\,\mu J$	$\leq 1\,\mu J$
RPC	Gap width	mm	2	2	1
	Dimensions	cm²	10 × 20	6 × 22	0.8 × 2.4
	Gas mixture (Freon+iso-Butane+ SF$_6$)	%	94.7 + 5 + 0.3	90 + 10 + 0 and 97 + 3 + 0	94.7 + 5 + 0.3
	Electric field strength	kV/cm	46 − 55	43 − 47	48 − 53
Experimental performances	Charge distribution		Gamma	Gaussian	Gaussian
	Relative charge variation	%	not given	20	28
	σ Time resolution	ns	not given	sub-ns	0.7

Table 6.1: The comparison of experimental setups and performances of different experiments. HZDR data is compared to the data from [5, 6].
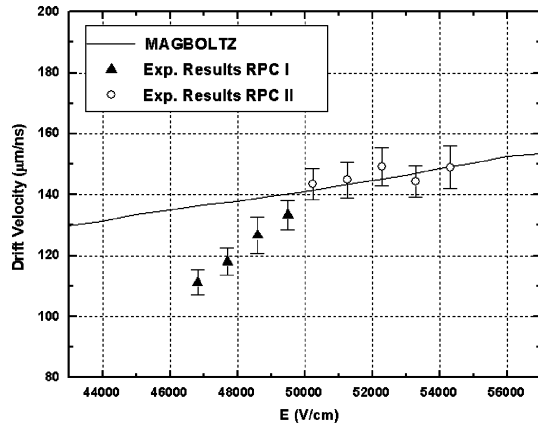
(i) Drift velocity measured by Chiodini compared to simulation. RPC I and RPC II are RPCs used in the experiment by Chiodini, with same geometry and different volume resistivity [6].
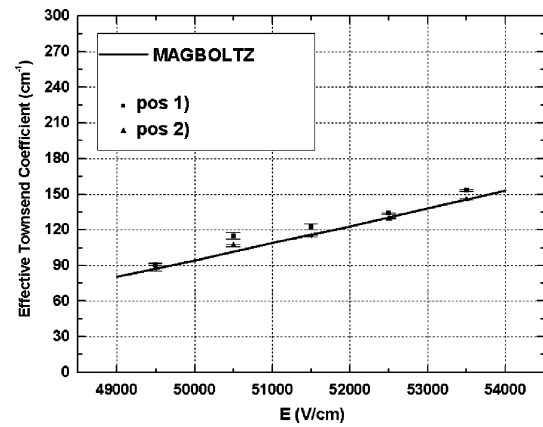
(ii) Effective Townsend coefficient measured by Chiodini compared to simulation. Pos 1) and 2) are different positions where exponential-like spectrum is observed. [6]
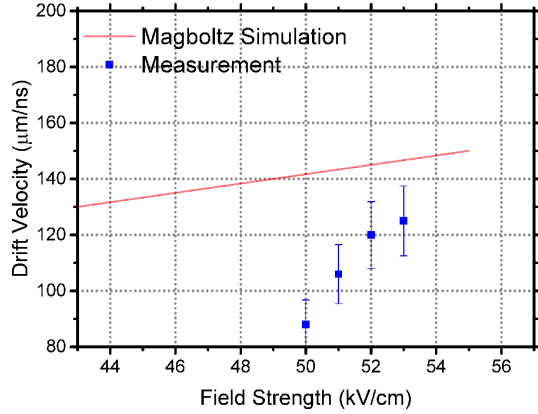
(iii) Drift velocity measured in HZDR compared to simulation.
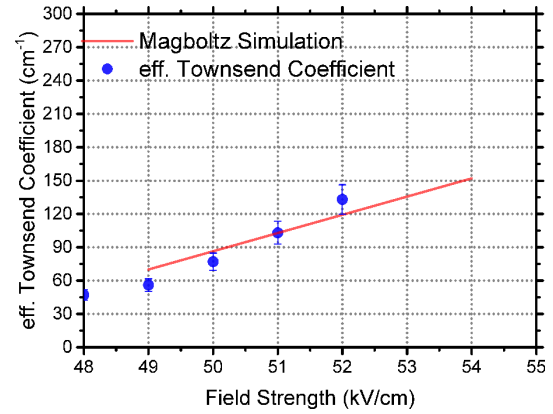
(iv) Effective Townsend coefficient measured in HZDR compared to simulation.

Figure 6.7: The comparison of simulation result by W. Riegler [64], experimental result by G. Chiodini [6] and HZDR test result.

6.1.3.2.1 Effective Townsend coefficient measurement The comparison of effective Townsend coefficient, presented in Figure 6.7(ii) and Figure 6.7(iv), has shown that the difference between measured value of HZDR and the data from other two works is approximately $\pm 10\%$.

The results of comparison has shown the validation of HZDR test facility and the methods in measurement of effective Townsend coefficient in trigger RPC.

6.1.3.2.2 Drift velocity measurement By comparing Figure 6.7(i) and Figure 6.7(iii), it can be seen that the measurement value of electron drift velocity of HZDR is less than the simulation value by W. Riegler and measurement value by G. Chiodini. A slope of fast increase of measurement value has appeared for both measurement value, before the electric field of $50\,\text{kV/cm}$ in Chiodini's measurement and $52\,\text{kV/cm}$ in HZDR result.

The difference is significant and should be well investigated.

First assumption is that the drift velocity is sensitive to concentration of SF_6 gas. Consider that there are only 0.3% of SF_6 in the gas mixture and difference of concentration of SF_6 will result in change of electron attachment, there is a possibility that the measurement is therefore very sensitive to concentration SF_6.

By comparing the data presented in [6] and HZDR data, another assumption can be made. Although rate effect (full discussion in Section 8.1.2.) is not observed in the HZDR experiments with trigger RPC field strength, the experimental result of rate effect of trigger RPC is observed and investigated by Chiodini [6], presented in Figure 6.8. The figure has shown that while 'rate effect' reduces the measured value of charge, it increases the value of electron drift velocity. If this is the case, in a situation where rate effect is not observed in HZDR experiment, the measured value will be smaller than the experiments by Chiodini where rate effect exists.

The third assumption is that the pulse duration has a influence on the measurement of gas parameters.

It is generally accepted that the drift velocity value can be obtained by analysing the time over threshold measurement results. However, from the experimental results of HZDR and from Chiodini's, there is a possibility that the measured value is influence by the repetition rate, which suggests that this method may have a possibility for further improvement.

6.2 Towards the higher field

After the experiments and comparison in trigger RPC, it is accepted that the effective Townsend Coefficient data can be obtained by HZDR laser test facility in trigger RPC mode, and the measurement of electron drift velocity may be related to some more fundamental knowledges which is beyond the thesis. The exploration in trigger RPC field strength is concluded and further steps can be taken.

Before the voltage is increased to timing RPC range, the field strength should be increased gradually. Also, the trigger RPC gas is different from timing RPC gas as timing RPC gas contains larger fractions of SF_6(10% in our experiments).

If trigger RPC parameters are tested with trigger RPC gas, and timing RPC parameters are tested with timing RPC gas, the connection between the experiments is not very strong as both
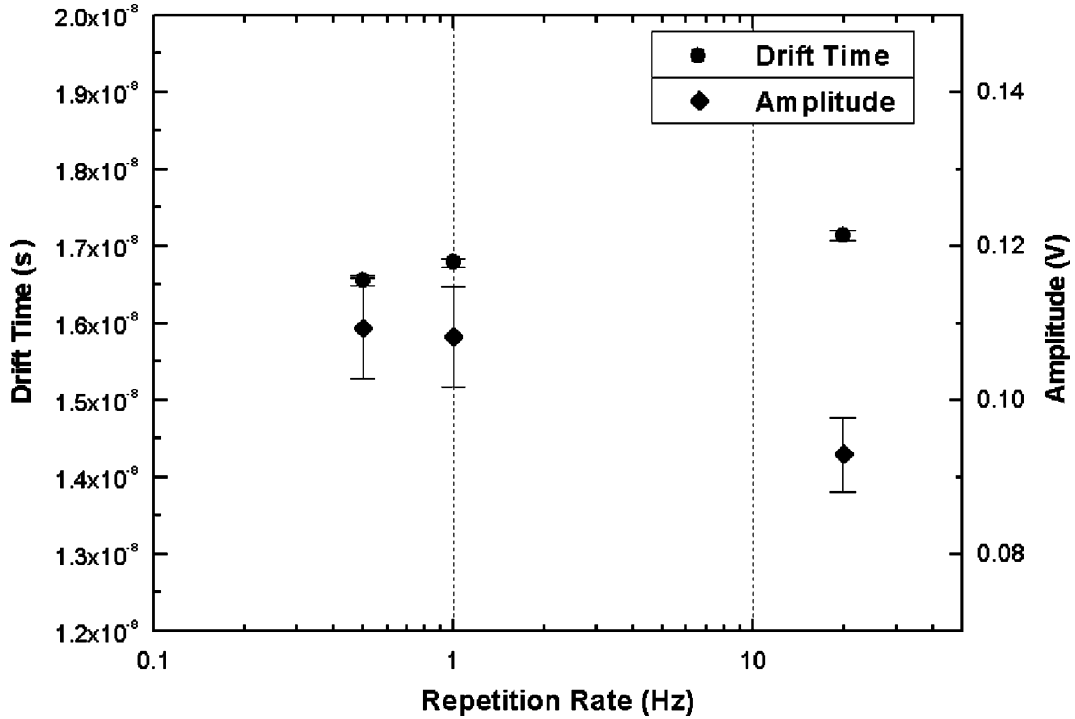
Figure 6.8: Drift time and average pulse height versus laser repetition rate measured by Chiodini [6]. As the repetition rate is increased, the signal amplitude decreased, which can be fully understood and described by rate effects in Section 8.1.2. However, the measurement value of drift velocity rises when rate effects becomes significant.

the gas mixtures and field strength are different. To make a better connection between the two experiments, a bridge experiment was operated and presented in this section.

In the first experiment, trigger RPC gas is used. The voltage of detector is increased eventually to measure the change of gas parameters until the dark current, breakdown or streamer becomes significant observed from oscilloscope. Gas parameters of several data points beyond 50 kV/cm are measured, no breakthrough, huge dark current or huge streamer signal appears up to our second highest measurement point around 85 kV/cm. When the field strength is beyond this value, the effects of over voltage begin to appear.

In the second experiment within same field strength region, the gas parameters of timing RPC gas are also tested, which is in the range of lower electric field than working condition. This measurement will not be introduced too much as it is very similar to the experiments introduced in Section 6.3.1. Only the value will be presented.

6.2.1   Results and the influence of laser pulse rate

Before the experiment is operated, the laser pulse rate should be considered first. As the field strength is beyond the range of trigger RPC, the charge of signal will become larger, which will result in a more significant rate effect.

In the experiment of 6.1, the measurement is operated in different laser repetition rate. Except the experimental setup of 2.5 Hz, the signal performance of 10 Hz is also checked, no significant difference is found. But if it is high than the order of 10 Hz, charge and amplitude of

signal will be much smaller observed from the oscilloscope.

In the measurement of trigger RPC, if an acceptable value of the upper limit of the laser rate is $10\,\mathrm{Hz}$, and the measurement is operated with $2.5\,\mathrm{Hz}$ which is one fourth of the limit, the reduction of high rate should be well reduced. In the final experiments, two different rates are chosen: 1 and $5\,\mathrm{Hz}$.

When the value from two measurement begin to separate, the reduction effect begin to happen on the higher rate. The test result is shown in Figure 6.9. It can be seen that when the laser rate is $5\,\mathrm{Hz}$, the reduction effect becomes significant from a value around $75\,\mathrm{kV/cm}$.

A test with laser rate of $2\,\mathrm{Hz}$ is also operated in the field strength same as the last measurement value, the effective Townsend coefficient is similar to that of $1\,\mathrm{Hz}$, so that it proves that there is no reduction from laser rate of below $5\,\mathrm{Hz}$ in this measurement.
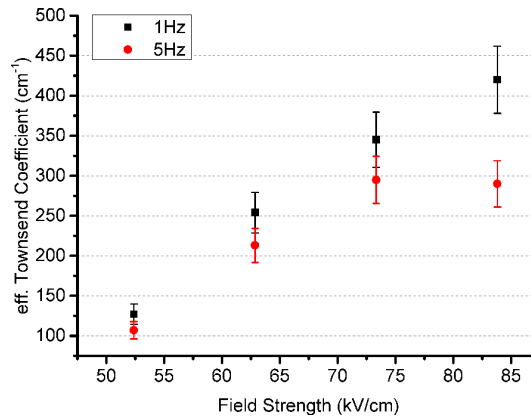
Figure 6.9: The effective Townsend coefficient measured with trigger RPC gas at higher field strength with different laser repetition rates with laser intensity of $2 \times 10^8\,\mathrm{W/cm^2}$.

The comparison between the measurement results and the simulation result will be further discussed in Chapter 8.

As an approach towards the higher electric field, this measurement is successful and the preparation to proceed to the measurement of gas parameters in field strength of timing RPC is ready.

6.3 On the field strength of timing RPC

Compare to the trigger RPC, timing RPC has much higher electric field (up to $100\,\mathrm{kV/cm}$), much thinner gas gap (the gap width of timing MRPC is usually less than $0.3\,\mathrm{mm}$). Timing RPCs have very good time resolution, usually around $50\,\mathrm{ps}$.

There has never been a measurement of the gas parameters of Timing RPC at atmospheric pressure, because of the following challenges:

- The field strength is too high, breakdowns and sparks are very harmful to instruments.

- The effective Townsend coefficient is too high. If the electron is started from the cathode, and the amplification length is $0.2\,\mathrm{mm}$ or $0.3\,\mathrm{mm}$, the amplification will be at least two or

three orders of magnitude larger and reach the Raether Limit[1] [102] so that the avalanche develops into a streamer signal.

- The scale is too small. if the effective Townsend coefficient is $100\,\mathrm{mm}^{-1}$, then a number of electrons N_e at position d will develop into $100N_e$ after only $\frac{\ln 100}{100 mm^{-1}} = 0.046 mm$. Although our measurement results have shown that the amplification is only in the order of $50\,\mathrm{mm}^{-1}$, the scale is still very small and requires high precision measurements.

For the difficulty of breakdown, no significant problems with glass RPC is found. Difficulty only appears with the first design of ceramics RPC(I) electrodes: the dark current is one or two magnitude larger than glass RPC sample and cannot be reduced by time. It is believed that the dark current is due to the trapezoid shape of cross section of the ceramic RPC(I). Because that the volume resistivity of ceramic is about three orders of magnitude lower compared to glass, there is a discharge on the sharp edge. In order to overcome the problem, make two measurement are made one after another: on glass RPC, then on the 2nd design of ceramics RPC (called ceramic RPC(II)) whose sharp edge is rounded off.

6.3.1   Measurement with glass RPC

6.3.1.1   Experimental setup

The first test is operated with glass RPC. The detector and electronics are implemented similar to that already described in Section 6.1. The working gas in this experiment is a typical timing RPC gas: 85% Freon + 5% iso-Butane + 10% SF_6. The pre-amplifier gain amounts to 10 dB.

The field strength in gas gap is increased slowly towards $100\,\mathrm{kV/cm}$. When the current and voltage value shown on the high voltage supply has reached a stable condition, the dark current is below the minimum value of $0.0001\,\mathrm{\mu A}$ that the high voltage source can measure.

The low voltage supply of pre-amplifier is then switched on. On the oscilloscope, the trigger source is set on the waveform of detector readout, and only random noise with frequency of about 1 Hz and the amplitude of less than 0.1 mV is observed. This is a normal noise behaviour for RPC detector, and has no influence on the field strength of gas gap and the performance of detector.

The trigger source is then set to the photo diode, no noise signal is observed. The background noise is around 0.02 mV. It has no influence on the signal when the peak of signal is beyond the noise. In normal operation condition, the amplitude is in the order of 0.5 mV on the oscilloscope which is one order beyond the noise.

Because of the very high field strength, the gap widths we can choose for RPC samples are 0.3 and 0.5 mm. In the previous experiments, we have observed that the ceramic RPC(I) samples have high dark current, so that we have decided not to take the ceramic RPC(I) samples for experiments in this test.

The measurement takes very long time. The reason is that although it is already known that there is a reduction of charge by repetition rate and it will take some recovery time as long as several seconds, however, in the experiment, the necessary repetition rate is so low: 0.05 Hz, or 20 seconds per one pulse. Even we reduce our expectation of statistics and acquire less waveforms, an experiment will still take decades of hours. It has very high requirement for

---

[1]Avalanches approaching approximately10^8 electrons will develop into a streamer signal, the number of 10^8 is Raether's Limit.

the stability of laser and the reliability of automatic programs. Fortunately the requirements are achieved and the gas parameters are successfully measured.

6.3.1.1.1 Comparison of different gap widths RPC samples with gap width of 0.3 and 0.5 mm are tested to compare.

The first measurement is operated with 0.3 mm RPC sample, because the width of gas gap is close to a real timing RPC or MRPC. Some difficulties arise in the experiments. The first difficulty is that the gas gap is narrow so that the region for laser input is narrow and requires more efforts for alignment. The second, also the most important is that the time constant of 0.3 mm RPC is longer than 0.5 mm RPC, a larger time constant will result in a longer time for experiment, the detail is described in Section 6.3.1.2.2 and Section 8.1.2.

Then the 0.5 mm RPC is tested. At the beginning, there is a worry that the gas gap is too wide to represent a real RPC, however, by comparing the performance and measurement result of RPC sample with gap width of 0.3 and 0.5 mm, it is observed that the experimental results obtained from the two RPCs are same if the length of drift paths are same. A primary conclusion is drawn that the width of gas gap have no influence on the signal development on a given position of ionization.

The 0.5 mm RPC is then taken for experiments.

6.3.1.2 Waveforms and data analysis

The signal is averaged in the same method presented in Section 6.1.2.1, and plotted in Figure 6.10.

Compare to the waveforms of trigger RPC presented in Figure 6.2, some differences can be seen: the rising slope of signals are not overlapped, and the shapes of signals looks complicated perhaps due to reflections in signal transmission.

The drift length is from 30 μm to 120 μm with step length of 3 μm. Although the range of drift lengths are smaller than the experiments of trigger RPC, the signal amplitude is much larger due to the higher effective Townsend coefficient and electron drift velocity in trigger RPC.

It is not possible to obtain the drift velocity from the waveforms. However, by setting a threshold and time window, the time resolution, charge distribution, and finally the Effective Townsend coefficient can still be obtained.

The time resolution is 43 ps and the deviation of charge is only 7%.

6.3.1.2.1 Effective Townsend coefficient Before the calculation of the effective Townsend coefficient, a plot of the charge in dependence of the distance to anode and the repetition rate should be considered to make an estimation of the charge reduction effect. The signals are measured with different laser pulse rate, and the signal charge is plotted in Figure 6.11. The measurement points are selected to get rid of too small signals or saturation signals.

Each series of values are fitted with $Q = Ae^{\alpha d}$, where Q is the charge, A is a constant, d is the distance to anode. The effective Townsend coefficient α is calculated and plotted in Figure 6.12.

It can be seen that as the repetition rate is decreased, the obtained effective Townsend
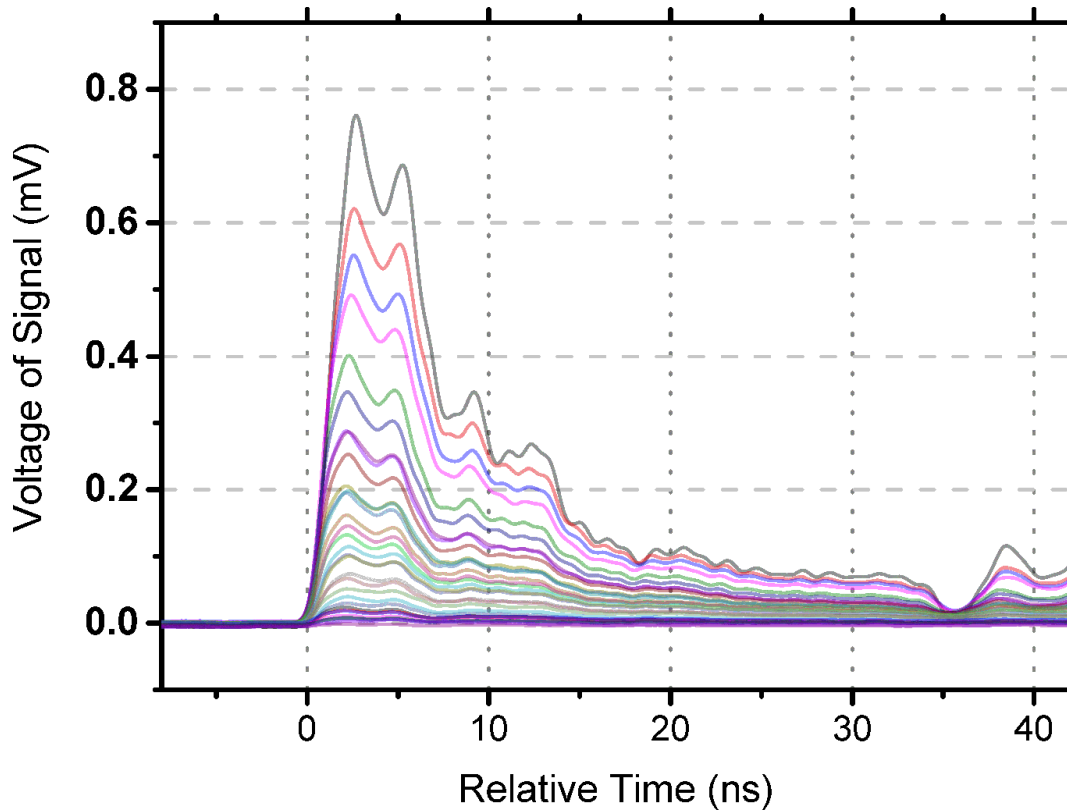
Figure 6.10: Waveforms of glass timing RPC. The drift length is from $30\,\mu m$ to $120\,\mu m$ with step length of $3\,\mu m$. The average laser intensity on the section of beam waist is $2 \times 10^8\,W/cm^2$. The estimated mean and fluctuation number of primary electrons is the same as discussed in Section 5.4.2. The current number is the data original waveforms from oscilloscope divided by the amplification of pre-amplifier. Each waveform is the average of 300 waveforms. It can be seen that each waveform contains two main peaks and multiple smaller peaks. Compared to Figure 6.2, the overlapping of rising curve is not observed. In the experiment of ceramic RPC(II), the double peak is proved to be a result of possible reflections of signal and the limit of bandwidth, see Figure 6.14 and Section 6.3.2.
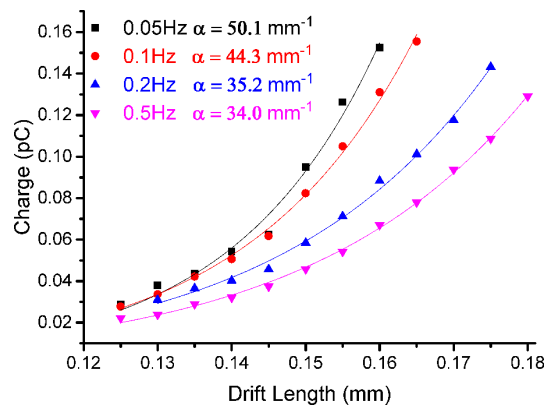
Figure 6.11: Dependence of signal charge on laser repetition rate and distance to anode. It can be observed that the reduction of charge is only avoided at $0.05\,Hz$ at most, which is $20\,s$ recovery time. The laser intensity amounts $2 \times 10^8\,W/cm^2$
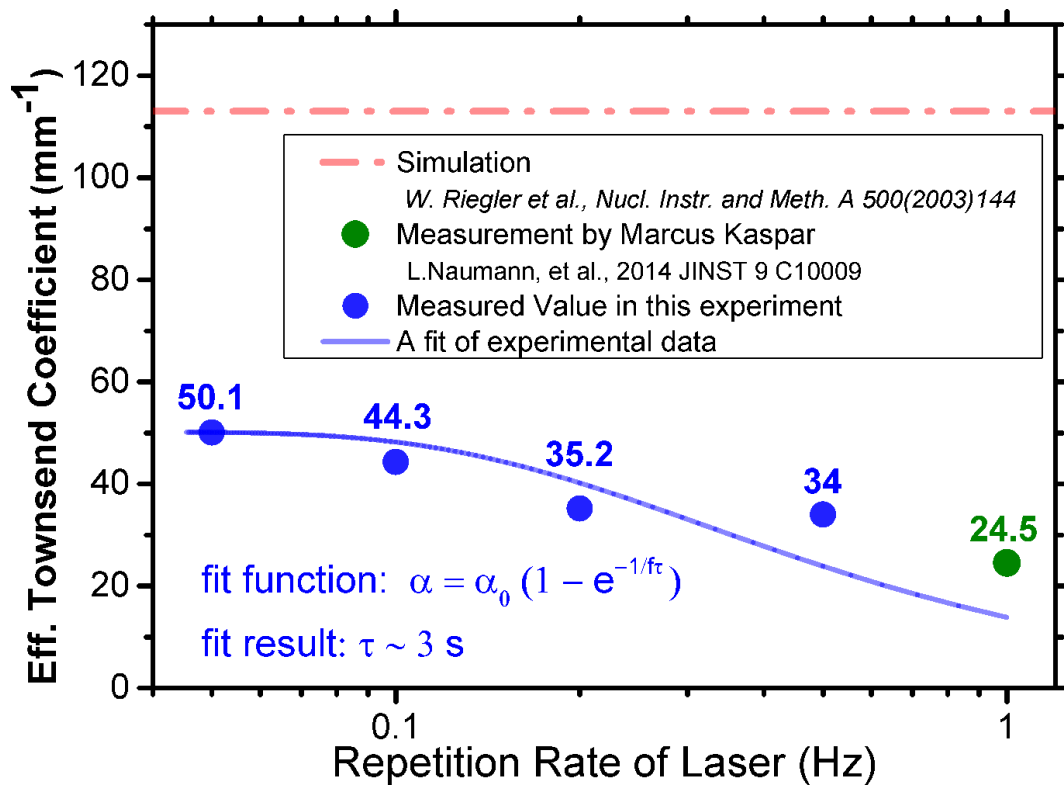
Figure 6.12: Dependence of measured effective Townsend coefficient on laser repetition rate. It can be concluded that for the repetition rate of 0.05 Hz where the field strength is nearly fully recovered, $alpha_{eff}$ is only approximately half of Magboltz value. Measurement result in [89] (green point) is reasonable, considering rate effect of RPC. The measured value is accumulated from data in Figure 6.11.

coefficient tends to a maximum value gradually. Assuming that the relation of effective Townsend coefficient with laser pulse rate follows approximately

$$\alpha_{measurement} = \alpha_0 \, e^{-\tau f} \, , \tag{6.1}$$

where α_0 is the effective Townsend coefficient in the non-reduced field strength, f is the pulse rate, and τ is a time constant. It is obtained that τ is around $3\,$s. It can also be estimated that the time constant measured in this experiment should be on the same order of magnitude with the time constant of RPC detector.

From the measurements of different pulse rate, it can be concluded that if the pulse rate is so low that the field is fully recovered, the effective Townsend coefficient will be approximately $50\,\mathrm{mm}^{-1}$. The value is about half of the calculation value obtained in [64].

6.3.1.2.2   The test of recovery time

As the recharge of detector has a very large influence in our measurements of effective Townsend coefficient, an additional experiment to investigate the field reduction is operated.

In this experiment, the position is fixed at distance to anode $d = 0.1mm$, and laser energy was also fixed. Then the repetition rate of laser pulse is changed to measure the signal charge.

The experiment is operated on both $0.3\,$mm RPC and $0.5\,$mm RPC. The charge-rate relation is plotted in Figure 6.13(i) and Figure 6.13(ii). We assume that the relation of signal charge Q and laser pulse rate f follows:

$$Q_{measurement} = Q_{max} \, e^{-\tau f} \, , \tag{6.2}$$

where τ is the time constant, the fitting result shows that the time constant of $0.3\,$mm RPC is longer than $0.5\,$mm RPC, which is the main reason why we chose $0.5\,$mm RPC for experiments.

The time constant τ in this measurement is not the time constant of RPC, but they should be in the same order of magnitude by assumption.

From the data in Figure 6.13, it can be concluded that the time constant of signal reduction depends not only on the repetition rate of signals, but also on the signal charge. When the signal charge is smaller than a certain value, the time constant begin to decrease as well. For the charges that is larger than this signal, the obtained value of time constant is around $3\,$s for $0.3\,$mm gap width and $2\,$s for $0.2\,$mm gap width.

A further discussion of time constant will be presented in Section 8.1.2.

6.3.2   Measurement with ceramic RPC(II)

Based on the experiments in Section 6.1, Section 6.2 and Section 6.3.1, the ceramic RPC(II) detector together with new signal readout was designed and assembled. The detailed description is presented in Section 4.5.3.2.

In the previous experiments, although a lot of achievements are obtained, some difficulties still remain. To get an explanation and to improve the performance of detector, The objectives and solutions in ceramic RPC(II) are described as follows in short:
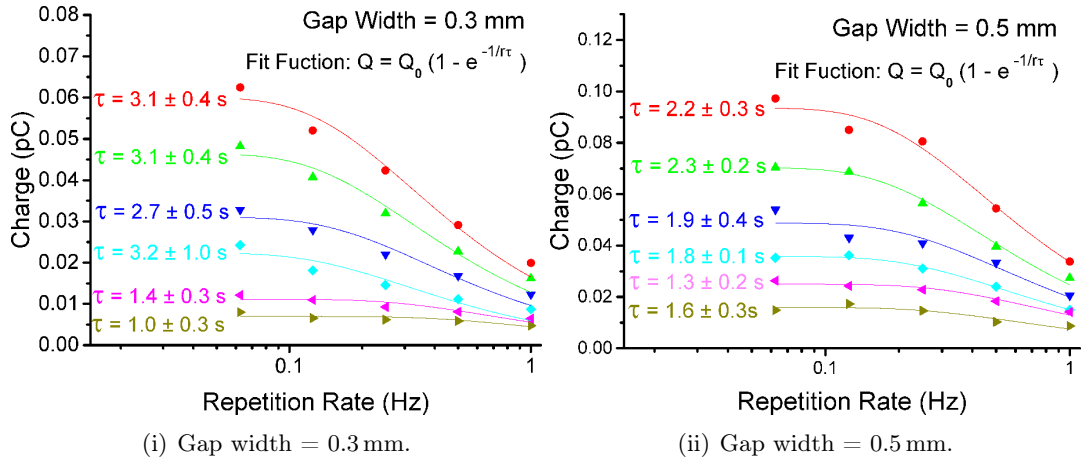
(i) Gap width = 0.3 mm.   (ii) Gap width = 0.5 mm.

Figure 6.13: The charge of signal in dependence repetition rate for different laser intensities. The laser intensities from small to large are 2.5×10^8, 3.54×10^8, 5×10^8, 7.07×10^8, 1×10^9 and $1.41 \times 10^9\,\mathrm{W/cm^2}$ respectively. The field strength are both $100\,\mathrm{kV/cm}$.

Position of laser focus is fixed for each of the experiment, however, the drift length is 0.1 and 0.15 mm for experiments with 0.3 and 0.5 mm gas gap, respectively. Considering that the absolute position accuracy is in the order of $10\,\mathrm{\mu m}$ and will result in a difference in the signal charge, the charge values in the two figures cannot be compared to each other.

- **1:** To reduce the recovery time, the resistivity of electrodes should be less. As discussed in Section 6.3.1.2.1 and Section 6.3.1.2.2, long recharge time of glass RPC detector makes it extremely time consuming for a measurement, but it is not possible to make systematic measurements in short time. If the time constant is related to volume resistivity, the ceramic electrodes should reduce the recovery time by two orders of magnitude due to the reduced volume resistivity of the ceramic in comparison with float glass.

- **2:** To properly measure the drift velocity, the signal readout system should be upgraded. The waveforms acquired from first RPCs are not in good shape, making it difficult to measure the drift velocity. Although the situation is not very clear, by estimation we believe that the reason is because the impedance of readout system is not uniform and reflection occurs. So that it worth trying to simplify the readout system. If the shape is still not improved, we should begin to consider the chips inside pre-amplifiers or connectors to oscilloscope.

- **3:** Reducing the dark current of ceramic RPCs. Because of the high dark current in the previous ceramic RPC samples, test on ceramic sample is skipped. A measurement with ceramic electrodes is necessary as a comparison to the results from glass RPC, in order to study the similarities and differences of electron avalanche process in RPCs of different resistivity. To avoid dark current, the edge of electrodes are rounded. If the dark current is caused by edge discharge effect in the ceramic RPC(I) samples, it should be reduced in ceramic RPC(II).

Because of the careful preparation, when the ceramic RPC(II) is assembled and tested, the three objectives are all proved to be successfully achieved.

6.3.2.1   Experimental setup and preliminary test

The ceramic RPC was mounted on the moving stage. The gas is 85% Freon + 5% iso-Butane + 10% SF_6, same as the timing glass RPC.

6.3.2.1.1   Dark current
The high voltage was set to $5\,kV$ in the first measurement, the dark current is only $0.0005\,\mu A$. The influence of the dark current on the field strength is very little. This has proved that edge discharge is the only cause of dark current in ceramic RPC(I) and that the edge should be rounded to avoid discharge if the volume resistivity of electrode is low.

6.3.2.1.2   Improvements on rate capability
The rate capability is also much improved. The waveforms seen on the oscilloscope when the laser pulse rate is 1 and $10\,Hz$ are compared, there are no visible differences on the signal amplitude or shape.

Then the signal rate was increased to $100\,Hz$, and it is observed that the streamer ratio is significantly increased from about 10% to 50%. If the streamer signals are removed in the data analysis process, the remaining avalanche signals still satisfies the requirement of statistic.

The comparison in this experiment has proved that the reduction of signal charge in the glass RPC is due to reduction of field strength due to the previous signal. If the resistivity of electrodes is lower, the recovery of electric field will be faster.

Because of the very high streamer ratio, no measurement is operated for the performance above $100\,Hz$. $10\,Hz$ is also fast enough for data acquisition with high statistics in reasonable short time. Repetition rate of $10\,Hz$ is applied as the laser pulse rate for all other measurements with ceramic RPC(II).

Another conclusion is that the rate capability is determined by the resistivity of electrodes and purity of gas. Further discussions are presented in Section 8.1.2.

6.3.2.2   Experiments and signal analysis

Using the same method described in Section 6.1.2.1, the average waveforms are acquired with ceramic RPC(II). As an example, the waveforms when electric field $E = 100 kV/cm$ are presented in Figure 6.14.

Compare to the waveforms of glass RPC in Section 6.3.1, it can be seen that the waveforms obtained in the ceramic RPC(II) is much improved due to the improvement of readout systems. As the distance to anode is different, the signals are ordered from low to high and can be well distinguished.

Compare to the waveforms from the trigger RPCs in Section 6.1, there are also some differences. First, the waveforms are not overlapped in the rising edge, it is believe that this is due to the diffusion and electrical system, a further explanation and discussion will be presented in Section C.4. Second, the rising time is much shorter, because the high effective Townsend coefficient and drift velocity both contribute to the signal growth.

The time of maximum voltage of waveforms are now well distinguished. If the time of each peak on the waveforms are analyzed, the time values vs. the distance to anode will be placed as a linear-like figure. If it is really linear, the drift velocity in this voltage can be obtained.
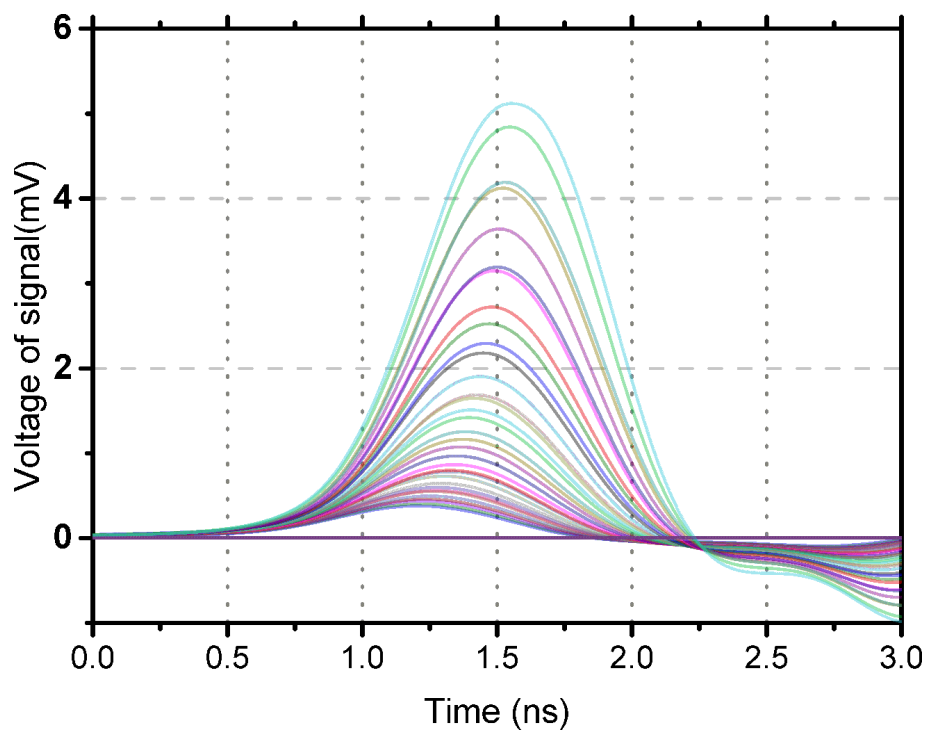
Figure 6.14: The waveforms taken from the ceramic RPC(II) working in timing RPC electric field strength of $100\,\mathrm{kV/cm}$. The gas mixture is 85% Freon + 5% iso-Butane + 10% SF_6. Drift length is from $20\,\mu\mathrm{m}$ to $80\,\mu\mathrm{m}$ with the step length of $2\,\mu\mathrm{m}$. Laser repetition rate is $10\,\mathrm{Hz}$, average laser intensity on the section of beam waist is $2 \times 10^8\,\mathrm{W/cm^2}$. The waveform is averaged from 1000 waveforms, saturation signals and too small signals are not shown in this figure according to the data selection process presented in Figure 6.15.

To obtain the effective Townsend coefficient, the time window is set to just contain the main peak, the voltage of each signal is obtained. The Townsend coefficient is acquired by fitting the charge-distance relation.

An example of data selection of charge is shown in Figure 6.15. In this figure, the upper limit is 80 μm, where saturation effect occurs. The lower limit is selected to be around 40 μm, where the σ time resolution calculated from relative threshold is above 30 ps.
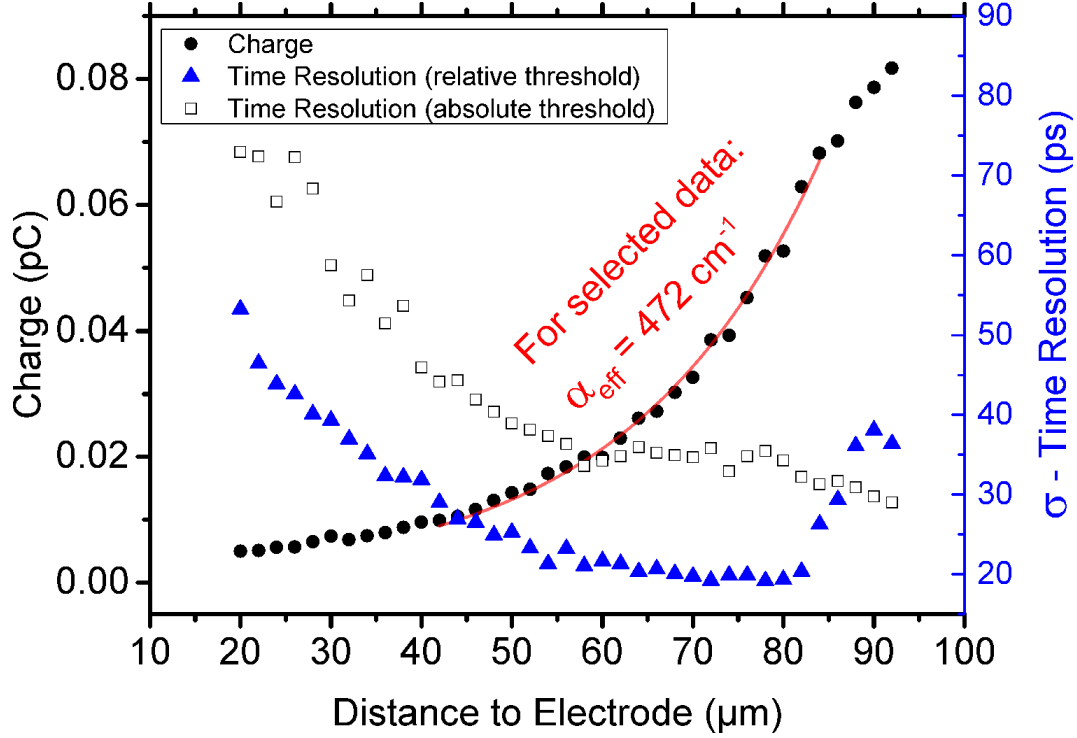
Figure 6.15: The average charge and time resolution as a function of distance to anode. This figure shows the upper and lower limit of charge in data selection for accumulating the effective Townsend coefficient. The experimental parameters are same with Figure 6.14. The selected data is accumulated from the waveforms shown in Figure 6.14.

6.3.2.3   Townsend coefficient and drift velocity

After the data selection process, the average charge as a function of different distances to anode is plotted shown in Figure 6.15, there is an exponential growth region with very wide range of 40 μm with 20 data points. The effective Townsend coefficient is fitted with function:

$$Q = A\, e^{\alpha d}\,, \tag{6.3}$$

where Q is the total charge of signal, d is the distance to anode, A and α are acquired in the fitting.

As the point of exponential range are selected, the time over threshold of the points are also measured. When the signal reaches maximum value of voltage, it is also the maximum number of electrons, the average drift velocity is then the time from when the signal is started to the time

of maximum voltage. Although we don't know the starting time of an avalanche, calculation on the arriving time of different distances to anode can still obtain the electron drift velocity. The trigger is set at 99% of maximum voltage as well as in the data analysis of trigger RPC in Section 6.1.2.5.

Two series of gas parameter scan are operated.

- **Precise field strength scan** around $100\,\mathrm{kV/cm}$. The step length is set at $2\,\mathrm{kV/cm}$, the scan range is from $94\,\mathrm{kV/cm}$ to $106\,\mathrm{kV/cm}$. The measurement was operated two times to confirm that the result is repeatable.

- **Wide range field strength scan** from $70\,\mathrm{kV/cm}$ to $120\,\mathrm{kV/cm}$. Starting from $70\,\mathrm{kV/cm}$ field strength, the field strength is increased with the step length of $10\,\mathrm{kV/cm}$. When the field strength is $110\,\mathrm{kV/cm}$, the gas parameters are still obtained. Unfortunately, the streamer ratio arise greatly when the field strength is $120\,\mathrm{kV/cm}$, and the ageing effect appears very fast. The ageing effect makes it impossible to make any experiment in a short period, because the dark current and the streamer ratio becomes very high. A further discussion will be presented in Section 8.1.4.

Using the stored waveform data, the effective Townsend coefficient and the electron drift velocity as a function of field strength has been obtained.

The result is plotted in Figure 6.16.

From the figure it can be seen that, the drift velocity and effective Townsend coefficient increases with the filed strength in the field range from $70\,\mathrm{kVcm}$ to around $100\,\mathrm{kV/cm}$. However, when the field strength reaches around $100\,\mathrm{kV}$, there seems to be a plateau of the effective Townsend coefficient. The measurement value of drift velocity before $104\,\mathrm{kV/cm}$ is in agreement with the simulation from Magboltz, however, the measurement value at $110\,\mathrm{kV/cm}$ has 10% variation from the simulation result.

The maximum drift velocity is around $200\,\mu\mathrm{m/ns}$, and the maximum effective Townsend coefficient is around $50\,\mathrm{mm}^{-1}$. The data of drift velocity is in agreement with the value calculated in [64] before the value reaches the plateau; when the plateau is reached, the measurement value of drift velocity becomes unchanged.

The effective Townsend coefficient obtained in glass RPC is also around $50\,\mathrm{mm}^{-1}$, in agreement with the value from ceramic RPC(II).

A detailed discussion of gas parameters will be presented in Section 7.1.

The drift velocity obtained from the measurements from ceramic RPC(II) is shown in figure 6.17. From the figure, it can be observed that the drift velocity measured from the laser test facility with ceramic RPC(II) is in agreement with Magboltz simulation results in the field strength of up to $160\,\mathrm{kV/cm}$. On the point of $110\,\mathrm{kV/cm}$, the electron drift velocity is below the simulation value. Although the explanation of the variation is not complete, a discussion is provided in Section 7.2.2.

6.3.3 Comparison

The effective Townsend coefficient of timing RPC for both glass and ceramic electrodes have been accumulated. Comparison of the obtained value is presented in Figure 6.16.

From the comparison, it can be concluded that the effective Townsend coefficient are in well agreement between the measurement value of two electrodes. The result has proved that our
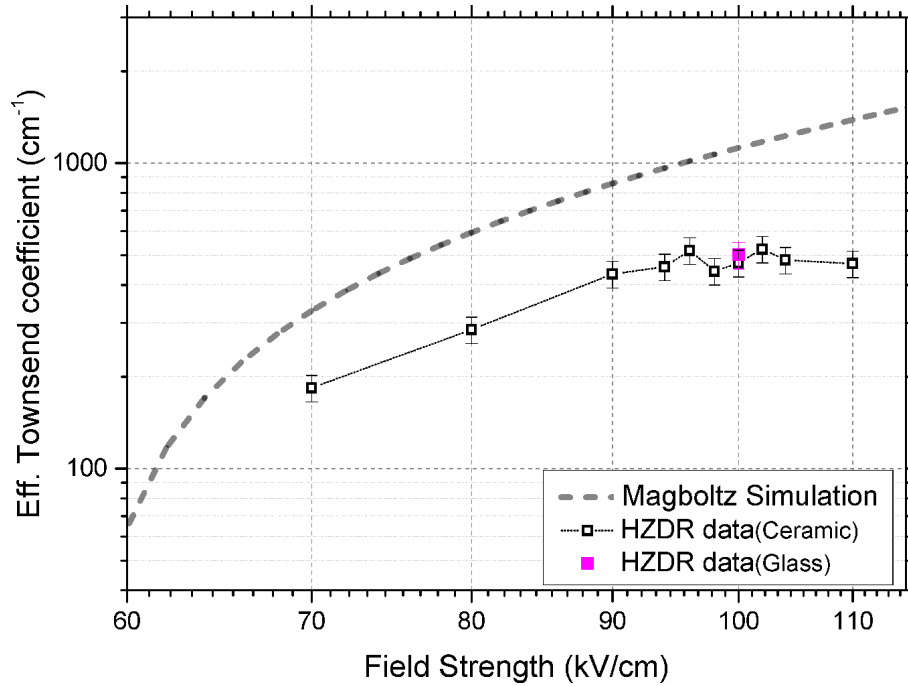
Figure 6.16: The effective Townsend coefficient for ceramic RPC(II) measured in a wide range of electric field. The gas mixture, laser characteristic are the same as shown in Figure 6.14. Simulation result is from [64].
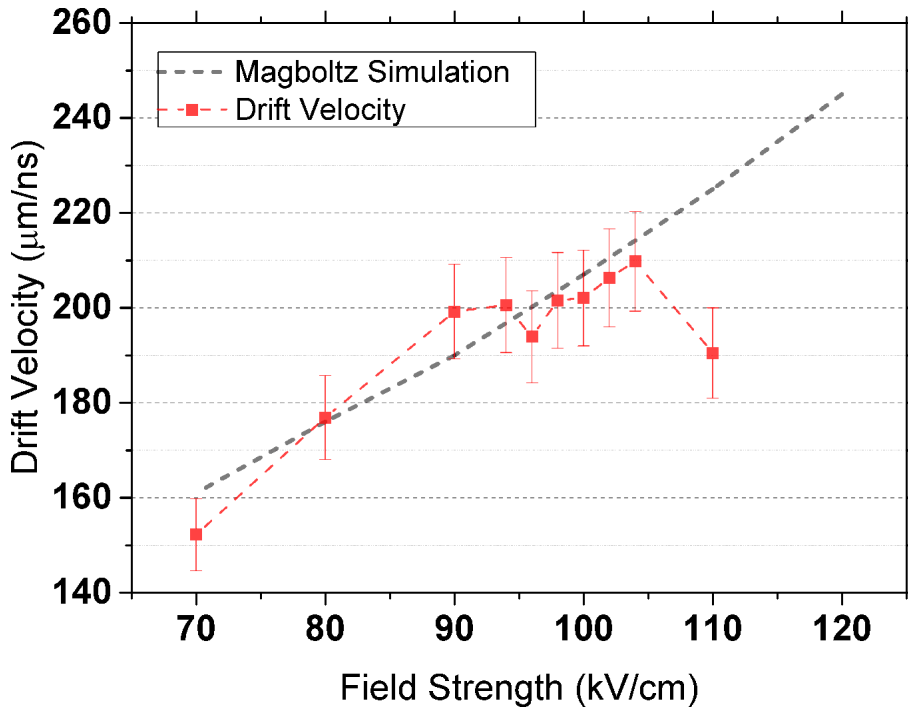

Figure 6.17: The electron drift velocity for ceramic RPC(II). The experimental setup is the same as in Figure 6.16. The gas mixture, laser characteristic are the same as shown in Figure 6.14. Simulation result is from [64].

method and measurement value is of high reliability.

As described in previous sections, the low rate capability with glass electrodes should be specially taken care of to accumulate the charge without repetition rate dependent electric field reduction, when the obtained value is in agreement to another detector, it can be concluded that our method to avoid rate effect in measurement is successful.

According to the calculation in Section 3.2.5.3, the value of τ is in the order of second for glass, millisecond for ceramic, while the time scale of an avalanche is in the order of nanosecond. The result is in agreement with the calculations in [3]: for the situation that the time constant τ of detector is much smaller than the time scale of avalanche, the signal will not be affected by the conductivity of the electrodes as the field strength has recovered from the previous signal.

6.4 Dependence of primary ionization on the results of gas parameters

Parallel to the experiments for RPC samples in timing RPC condition, there is a question that whether the number and position of primary electrons have a influence on the measurement data of the effective Townsend coefficient. Experiments are operated to investigate the question.

6.4.1 Measurement with glass RPC sample

The experimental setup is the same as described in Section 6.3.1. Data was taken from three different tests among various experiments: in these experiments, the laser intensity was approximately 1×10^8, 2×10^8 and 2×10^8 W/cm^2. However, because of the differences in alignment conditions, the exact relation of the laser intensities and number of primary electrons are unknown.

The experimental results are shown in Figure 6.18. From the figure, it can be seen that the obtained value of effective Townsend coefficient from exponential region of the figure, is not sensitive to the position and primary number of electrons.

6.4.2 Measurement with ceramic RPC(II) sample

The experimental setup is the same as described in Section 6.3.2. Data is taken from two different experiments with different laser intensities. The laser intensities cannot be directly compared, as the alignment conditions are not the same. Similar to the observation in Section 6.4.1, the the obtained values of effective Townsend coefficient is independent from the position and number of electrons in the primary ionization. The figure is presented in Figure 6.19.

Figure 6.18: The effective Townsend coefficient obtained from different laser intensities and positions by glass RPC sample. The repetition rate of laser is 0.5 Hz. The data is taken from different series of experiments, because of the differences in alignment conditions, the relation of the laser intensities and number of primary electrons are unknown. However, the obtained values of effective Townsend coefficient are similar.
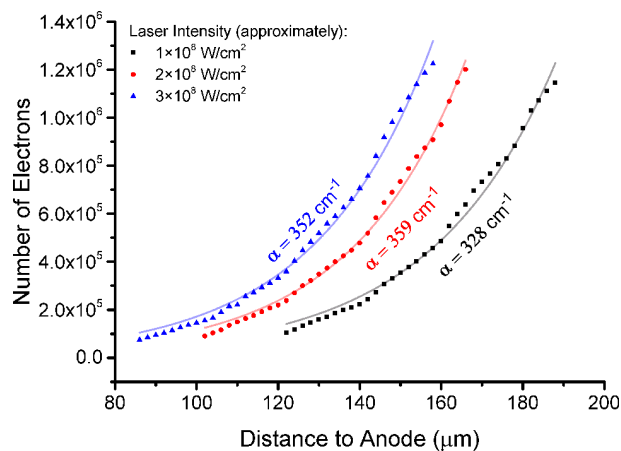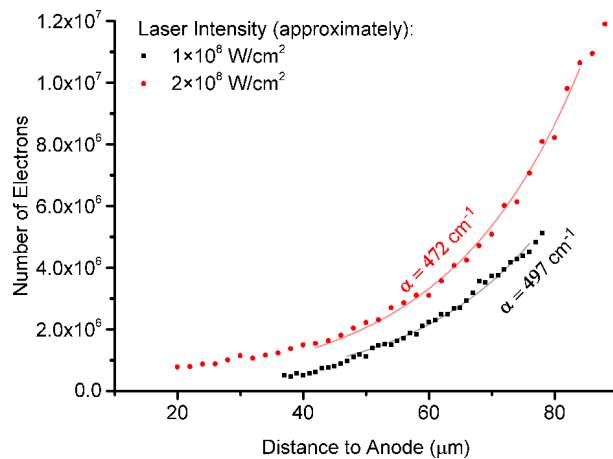

Figure 6.19: The effective Townsend coefficient obtained from different laser intensities and positions by ceramic RPC(II) sample. The repetition rate of laser is 10 Hz. The data is taken from different series of experiments, the relation of the laser intensities and number of primary electrons are unknown. However, the obtained values of effective Townsend coefficient are similar.

6.4.3 Conclusion

The ceramic RPC(II) sample test result is without influence of rate effects, while the glass RPC sample test results has the influence. For both the two conditions, the obtained effective Townsend coefficient is not sensitive to the position and number of electrons in the primary ionization.

6.5 Summary

In this chapter, the experimental setups and results obtained by RPC detectors in the field strength of trigger RPC and timing RPC are presented. Experiments are operated from trigger RPC field strength to timing RPC field strength, from smaller signal charge to larger signal charge. The experiments are operated step by step to be related in many ways, in order to examine each other's methods and results.

The gas parameters are obtained and be compared to other works, both simulation and calculation results. They are also compared to each other to increase the correctness.

The final design of ceramic RPC(II) has been proved a very efficient tool in the measurement of gas parameters for our objectives.

Chapter 7

Analysis study of timing RPC waveforms

In this chapter, a calculation script that is specially written for the simulation of waveforms is established. The purpose of the program is to improve the understandings of the waveforms acquired from the detectors, to better explain the shape, and the obtained values.

Although the script is only a rough estimation of the waveform, the calculation data shows similarity to the experimental results obtained in Chapter 6.

7.1 The calculations of waveforms

7.1.1 Discussion of real RPC waveforms

7.1.1.1 Waveforms obtained from different test methods

In the real RPC, the position of primary electrons is random, and the number of clusters also differs, so that all the measurement results that has been obtained are the result of the random distributions. Simulations have been made to analysis a signal of RPC, for example in [3, 64].

To make a simulation of RPC signal and compare it to a signal obtained from RPC, a signal can be generally divided into two steps:

1 A single electron as point charge at a certain location is assumed. Then we simulate the avalanche process, so that the development of signal as a function of position is built. The function will also include other parameters like cluster size, time, gas parameters, etc. The function that describes avalanche is in the form of $F(t, d)$, where t is the time and d is the initial distance to anode, $F(t, d)$ is the current, or the total number of electrons.

2 A real signal that contains multiple avalanches is obtained by adding the simulation waveforms that is initialized in different random locations. The process of a signal in RPC is then the sum of the avalanche signal in different locations, written in a form: $F(t) = \sum_d F(t, i), (i = d_1, d_2, ..)$. This is the waveform from RPC.

In many of the results obtained from a RPC experiment, only the total charge of signal is provided, which means the charge is written as: $Q \sim \int_0^{t_{max}} F(t)dt$, this is far away from

96

the original calculation in step.1 that there is only one cluster in a known position. Therefore, the results related to waveforms that contains the information of signal shape, which can be compared to the signal process in step.2 also has its difficulties to be compared to the simulation because the position of primary electrons and number of clusters are unknown.

Only by the laser test facility, the waveforms are possible to be recorded that can be directly compared to the formulas from step.1, as the initial position is controlled and the waveforms are recorded.

7.1.1.2 Influence of electronics in data acquisition system

The signal waveforms recorded in the oscilloscope is from the output signal of the amplifier, and the input signal of amplifier is the signal from the RPC detector. The full electronic system is an continuous-time linear time-invariant system, as described in [103]. The signal waveform is the convolution of the input signal and the impulse response of the system.

For the experiments on a detector, it is usually required that bandwidth of the amplifier is high which means the impulse response is fast so that the signal output is not deformed. In the experiment of ceramic RPC(II), the bandwidth of the pre-amplifier is 3500 MHz, it can be estimated that if the rising time of the original signal is faster than approximately 0.1 ns, the signal output will be deformed.

The waveforms from ceramic RPC(II) in Figure 6.13(i) has shown that the time scale of the signal waveform is approximately 1 ns which is one order of magnitude larger than than the system limit, so that the output signal should not be influenced by the data acquisition system in the experiment in ceramic RPC(II).

In this section, it is assumed that the readout waveforms are the amplified signal from induced charge of RPC detector without deformation.

7.1.2 Equations of induced signal

7.1.2.1 Without electron diffusion

As is introduced in Section 3.2.3.1, the induced current by avalanche follows:

$$I_{induced}(t) = N_e(t) \frac{e \, v_{drift}}{d} = \frac{e \, v_{drift}}{d} N_0 \, e^{(\alpha-\eta) \, v_{drift} \, t} \, , \tag{7.1}$$

where $N_e(t)$ is the number of electrons at time t, e is the charge of an electron, v_{drift} is the electron drift velocity, d is the gap width, α is the first Townsend coefficient, η is the attachment coefficient.

Consider that in a high homogeneous field in timing RPC condition, when the avalanche is well below the Raether Limit, the electron drift velocity v_{drift} should be constant, then:

$$I_{induced}(t) \sim N_0 \, e^{(\alpha-\eta)v_{drift} \, t} \, . \tag{7.2}$$

In the avalanche process, the induced current $I_{induced}(t)$ will be exponential growth with the power of $(\alpha - \eta) \, v_{drift}$.

The total charge of the signal Q_l of the length of drift path l is given by:

$$Q_l = \int_0^{l/v_{drift}} I_{induced}(t)\, dt \sim \frac{N_0}{(\alpha - \eta)\, v_{drift}}\, e^{(\alpha-\eta)\, l} \sim e^{(\alpha-\eta)\, l} \,. \tag{7.3}$$

7.1.2.2 With diffusion of electrons

In a realistic situation, the diffusion of electrons will also influence the induce current of detector. As is presented in [3], the induced current $I_{induced}(t)$ at time t and total charge Q_l with electron diffusion is given as:

$$I_{induced}(t) \sim e^{\alpha_{eff}\, v_{drift}\, t} \left[v\left(1 + erf\left(\frac{l - v_{drift}\, t}{2\, D\, t}\right)\right) - \sqrt{\frac{D}{\pi\, t}}\left(-\frac{(l - v_{drift} t)^2}{4\, D\, t}\right)\right] \,, \tag{7.4}$$

$$Q_l \sim e^{\alpha_{eff}\, l} \,, \tag{7.5}$$

where α_{eff} is the effective Townsend coefficient, v is the electron drift velocity, D is a constant defined as the diffusion coefficient of electrons.

Comparing Equation (7.5) and (7.3), it is notable that the total charge of the signal Q_l is independent from the diffusion coefficient.

An example of the waveforms calculated from Equation (7.4) and (7.2) is shown in Figure 7.1. The figure has shown that diffusion effect has resulted in a change of the time when the induced charge has reached the maximum value.
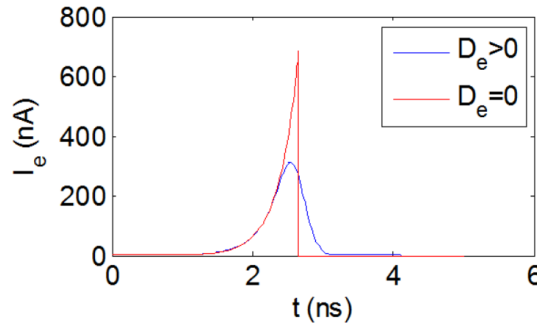
Figure 7.1: Induced current with and without diffusion D_e[1] calculated from the same parameters. In the diffusion case, $D = 7 \times 10^{-2}\,\mathrm{mm^2/\mu s}$. The corresponding induced charge is the same for both cases. Figure is taken from [3].

7.1.3 Numerical calculation

A program is implemented for calculating the signal waveform following Equation (7.4). The step length is set to $1\,\mathrm{ps}$, the range of time is set to maximum $3\,\mathrm{ns}$.

The parameters in the calculation is the effective Townsend coefficient α_{eff}, the electron

(i) α_{eff}=100 mm^{-1} (ii) α_{eff}=50 mm^{-1}
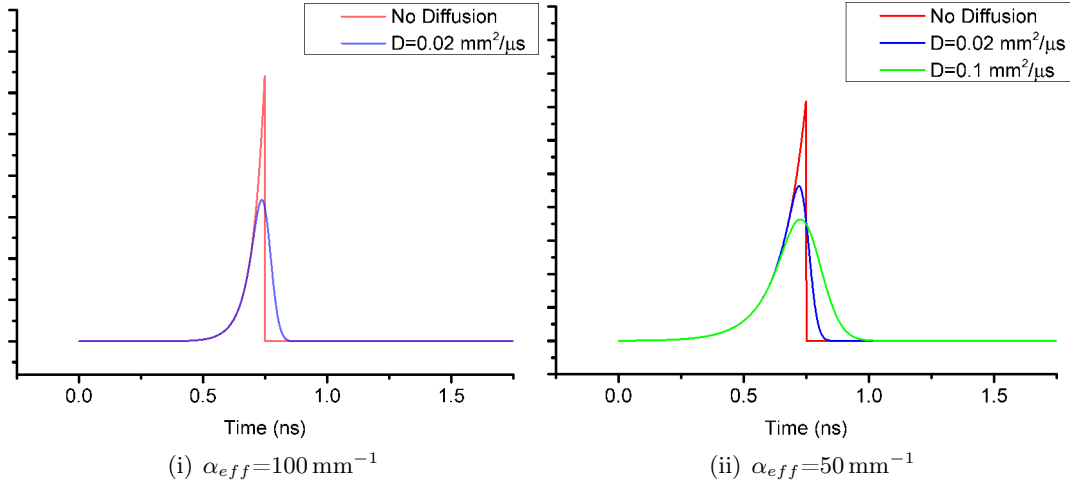
Figure 7.2: The calculation of waveforms with and without diffusion following Equation (7.4). The effective Townsend coefficient is selected approximately close to results of simulation ($\sim$100 mm^{-1}) and HZDR measurement ($\sim$100 mm^{-1}) respectively. The electron drift velocity is 200 µm/ns. Drift length is 0.15 µm. The diffusion coefficient D is shown in figures.

drift velocity v, the length of drift path l and the diffusion coefficient D. Results of waveform calculations of different D value is presented in Figure 7.2(i) and Figure 7.2(ii) respectively.

It can be concluded that the diffusion effect only appears when the total number of electrons have reached a certain value. Before the value is reached, the induced charge follows an exponential growth with the factor $\alpha_{eff}v$, and the equation is described by 7.2. After the value is reached, the influence of diffusion appears.

In the calculation it is observed that when D and α_{eff} is relatively large, for example when $D = 1 \times 10^{-1}$ mm^2/µs and $\alpha_{eff} = 100$ mm^{-1}, or when $D = 5 \times 10^{-1}$ mm^2/µs and $\alpha_{eff} = 50$ mm^{-1}, the calculated charge will vary from the of the non-diffusion situation, which is in contradiction with equation7.5. Having considered the failure of Equation (7.4), in the calculations operated and presented in this chapter, the D value is small enough that Equation (7.4) is valid and the variation of total charge is negligible.

7.1.3.1 Calculation of waveforms in dependence of drift length

Waveforms are calculated by fixed parameter α_{eff}=50 mm^{-1} or α_{eff}=100 mm^{-1}. Initial value of $v = 200$ µm/ns. Parameters of D is set as $D_1 = 1 \times 10^{-1}$ mm^2/µs and $D_2 = 2 \times 10^{-2}$ mm^2/µs respectively. For each setups, waveforms are calculated when the drift length of Z is from 0.03 mm to 0.15 mm with the step length of 0.03 mm in order to be compared to the data waveforms acquired from experiment in Section 6.3.2. The Calculation results are shown in Figure 7.3(i) and Figure 7.3(ii).

7.1.3.2 Influence of diffusion on electron drift velocity measurement

The calculated waveforms can also be analyzed following the methods of accumulating the electron drift velocity in RPC waveforms. The threshold is set at maximum value, and the time

(i) $D_1 = 1 \times 10^{-1} \, \mathrm{mm}^2/\mu\mathrm{s}$ (ii) $D_2 = 2 \times 10^{-2} \, \mathrm{mm}^2/\mu\mathrm{s}$
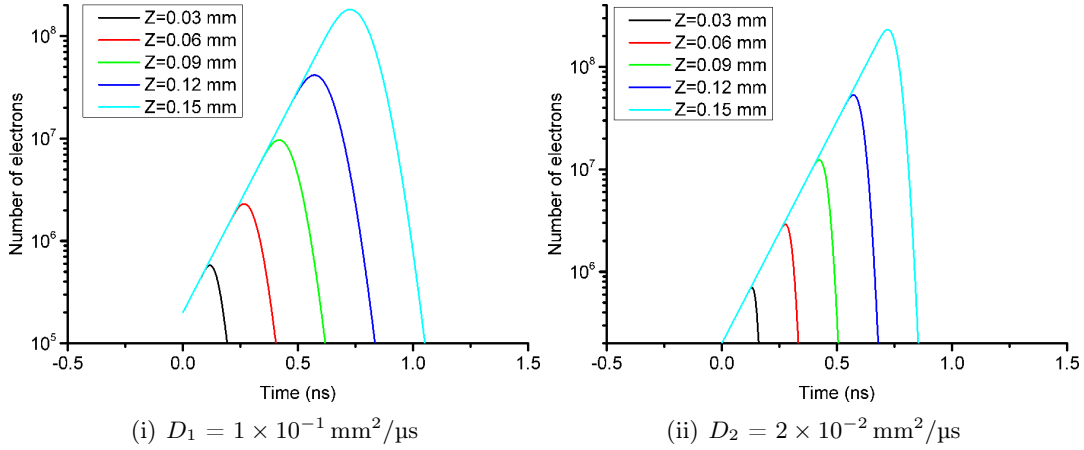
Figure 7.3: The calculation of waveforms with different number of diffusion coefficients following Equation (7.4). The effective Townsend coefficient is $\sim 50 \, \mathrm{mm}^{-1}$), electron drift velocity is $200 \, \mu\mathrm{m/ns}$. Drift length is from $0.03 \, \mathrm{mm}$ to $0.15 \, \mathrm{mm}$ with the step length of $0.03 \, \mathrm{mm}$. The diffusion coefficient is D.

over threshold is obtained in order to calculate the electron drift velocity. The initial parameter of electron drift velocity is set as $200 \, \mu\mathrm{m/ns}$, and the accumulated values of electron drift velocity are:

- when $D_1 = 1 \times 10^{-1} \, \mathrm{mm}^2/\mu\mathrm{s}$, $V_{calculation} = 197 \pm 1 \mu\mathrm{m/ns}$;

- when $D_2 = 2 \times 10^{-2} \, \mathrm{mm}^2/\mu\mathrm{s}$, $V_{calculation} = 203 \pm 1 \mu\mathrm{m/ns}$.

It can be concluded that, with different parameters of diffusion coefficient, the result of drift velocity can be either larger or smaller than the initial value. The values from two calculations have variation of less than 2% compared to the initial value, which is a negligible difference. However, as is discussed in previous section of the Equation (7.4), the number of D is limited due to calculation requirements. As a result, the validation of the conclusion is only verified in a certain range of D.

The calculation result can be taken as a reference to be compared with the waveforms.

7.2   Discussion of waveform analysis

7.2.1   Compare to calculation results

In HZDR test, the signal waveforms are recorded for detailed analysis of signal process and gas parameters. The signal waveforms from ceramic RPC(II) in timing RPC mode is presented in Figure 6.14. The gap width is $0.5 \, \mathrm{mm}$, the distance from laser focus to anode is 20 to $120 \, \mu\mathrm{m}$ with the step length of $2 \, \mu\mathrm{m}$. Figure 7.4 is the same data from Figure 6.14, plotted in logarithmic scale. From figure 7.4, the process of avalanche can be investigated. Saturated signals are not shown in the figure.

From Figure 7.4, the waveform data has shown the process of avalanche of different drift
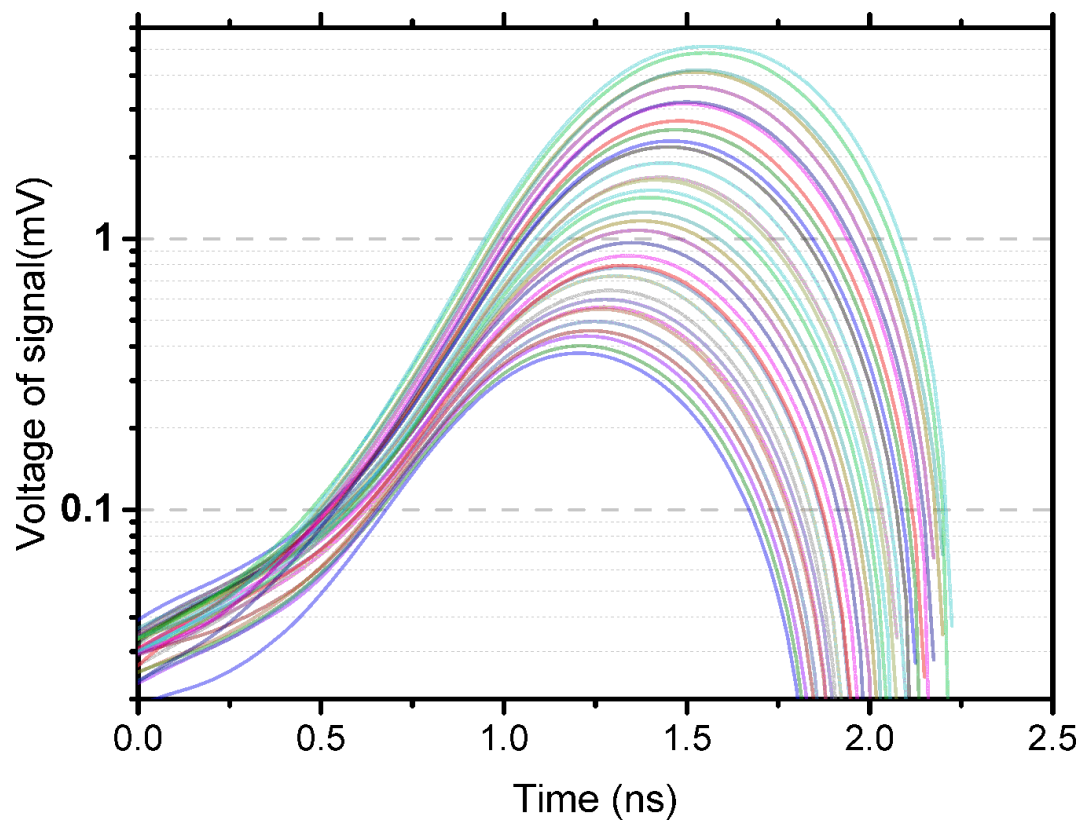
Figure 7.4: Signals induced from avalanches generated at $100\,\text{kV/cm}$ field strength in ceramic RPC(II). The lines represent the position scan of laser focus from $20\,\mu\text{m}$ to $80\,\mu\text{m}$ with the step length of $2\,\mu\text{m}$. Plotted in log scale.

lengths from $20\,\mu m$ to $80\,\mu m$ with the step length of $2\,\mu m$. It can be briefly concluded from the waveforms that:

- From 0 to 0.5 ns, the voltage of the waveforms is below $0.1\,mV$ (before amplification), and fluctuations of voltage occurs. the waveforms from different positions are close to parallel, but not overlapped. In an avalanche, this area is part of the exponential growth region. In this situation, the voltage is very small so that the noise cannot be ignored.

- From 0.5 to 1.0 ns, all the waveforms have shown an exponential growth. From the logarithmic scale, it can be observed that all the waveforms are parallel. The exponential growth of the induced current is in agreement with the growth of avalanche. The power of exponential growth is $(\alpha - \eta)v_{drift}$.

- From about 1.0 to 1.3 ns, the parallel waveforms begin to separate. Signal with shortest drift distance $20\,\mu m$ in this figure has reached a point where the growth begin to be limited at approximately 1.0 ns, while for the signal with longest drift distance reaches the point at approximately 1.3 ns. This is in agreement with the fact that electron drift will be stopped only by the anode.

- From the approximately 1.0 ns to the end, the signals are not directly shut, but drop down rapidly. The waveforms have shown how an avalanche signal is ended in a timing RPC.

The different regions of signal process have shown informations about the avalanche process in a RPC. The most notable information is that there is a parallel growth region for waveforms of different ionization positions. it is in agreement with the behaviour of Equation (7.4). The power of the exponential growth $\alpha_{eff}v_{drit}$ can be calculated.

However, from Equation (7.2) and simulated waveforms shown in Figure 7.3, the induced charge should be independent from the initial position, while in the acquired waveforms the signal are not overlapped. From the waveforms, the rising curve are located in order, from the minimum distance to maximum distance, showing that there is a clear dependence of ionization position. A possible explanation to this problem is that this is the limitation of experimental instruments.

Consider that the rising time of waveforms in the experiments is in the order of 0.5 ns. To explain the separation of waveforms, consider the physical and practical experiences, the bandwidth should not be a problem. the explanation should be as follows:

The signal separation occurs because of the pre-amplifier. Then the response is a possible reason. The output signal of an electronic system at time t is related to the response function of the electronics and the input signal before t. Even the rising edge of original signal is overlapped, because of the difference of signal process, the rising edge of output signal can be separated.

Whichever possibility it is, there are more unknown issues in the analysis of waveform than in the analysis of charge.

7.2.2   Obtaining the electron drift velocity

A possible issue in measurement of electron drift velocity has been discussed in Section 7.1.3.2. However, from the calculation of two specific diffusion coefficients, the difference compared to initial value is below 2%. As a comparison, the error of experimental value is in the order of 10%. It can be assumed that in a normal experimental situation, the influence of diffusion on the measurement of electron drift velocity is negligible.

Considering the measurement results presented in Figure 6.17, measurement values are in agreement with calculations except for the value measured under 110 kV/cm field strength. The agreement parts have shown that the method to measure the drift velocity is valid. The disagreement is not fully understood, could be either from experimental error, limit of system, or huge diffusion.

7.2.3 Obtaining the effective Townsend coefficient

Equation (7.2) and 7.5 has provided two different ways to calculate the effective Townsend coefficient.

- **Method 1:** By Equation (7.5), the effective Townsend coefficient can be obtained by the value of signal charge as a function of the drift length.

- **Method 2:** By Equation (7.2), the effective Townsend coefficient can be obtained by the exponential growth region in a signal. It requires the value of electron drift velocity.

In general, Method 1 is a better choice than Method 2, as a more precise value of total charge Q and length of drift path l can be obtained, the requirement for l is only the relative value but not the absolute value and that Q is independent from diffusion.

On HZDR laser test facility, Method 2 has become possible so that the effective Townsend coefficient can be obtained by two different methods. By comparing the measurement results from two methods, the result of gas parameters can be further investigated.

7.2.3.1 Comparison of experimental results of two methods

The waveforms obtained in the experiments of different field strengths of timing RPC are shown in Appendix D. It can be seen that for each voltage, similar waveforms have been observed as Figure 7.4. The exponential growth power is calculated by averaging all the waveforms and make an exponential fit for the exponential growth region.

The power of the exponential growth is $\alpha_{eff}v_{drift}$. The number is then divided by the electron drift velocity obtained from the difference of time and charge on signal peak in Section 6.3.2.3. The results of effective Townsend coefficient obtained from signal process are shown in Table 7.1.

The effective Townsend coefficient calculated from signal growth and from obtained signal charge (presented in Section 6.3.2.3) has shown different results. The comparison is shown in Figure 7.5. By comparing the effective Townsend coefficient obtained with two different methods, it can be seen obtained that:

- On the data point of $E = 70$ and $80 \, \text{kV/cm}$, the effective Townsend coefficient is in good agreement. The agreement has shown that both the methods can be taken to calculate the gas parameters in this region.

- From data point of $E = 90 \, \text{kV/cm}$, the two values are separated. The value obtained from signal process is around $300 \, \text{cm}^{-1}$, and from signal charge is around $500 \, \text{kV/cm}$.

Field Strength kV/cm	Growth factor ns^{-1}	Drift velocity $\mu m/ns$	Eff. Townsend Coefficient cm^{-1}
70	2.685	152.2	176.4
80	4.8609	176.9	274.7
90	5.8426	199.2	293.3
94	5.8683	200.6	292.5
96	5.5585	193.9	286.6
98	6.2045	201.6	307.8
100	6.8806	202.1	340.5
102	6.3641	206.3	308.5
104	6.2432	209.8	297.6
110	6.3112	190.5	331.3

Table 7.1: The effective Townsend coefficient obtained from signal waveforms.
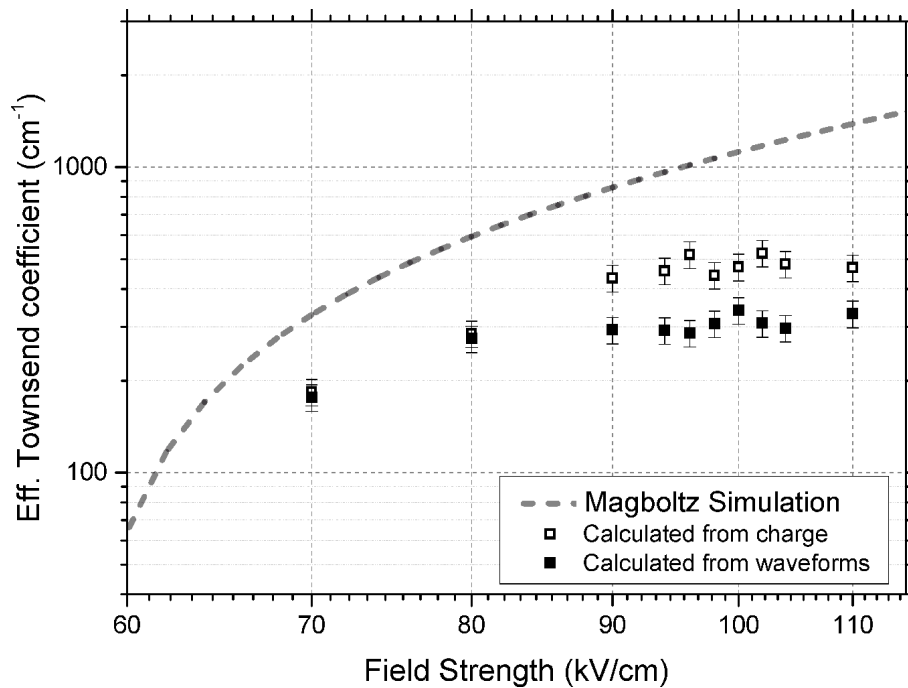

Figure 7.5: The comparison of Townsend coefficient deduced by two different methods. Simulation result is from [64].

7.2.3.2 Comparison and selection of two accumulation methods of effective Townsend coefficient

As is discussed in Section 7.2.3, the effective Townsend coefficient obtained by different methods have shown variation when the electric field is beyond $90\,\mathrm{kV/cm}$. A comparison should be made to investigate the realistic number. And the data that is closer to realistic situation should be taken as the final measurement result.

The agreement below $90\,\mathrm{kV/cm}$ and disagreement beyond $90\,\mathrm{kV/cm}$ may probably revealed a hint that, there is a difference in the mechanisms of induced signal with the border around $90\,\mathrm{kV/cm}$ field strength. Shown in Figure 7.5.

It is beyond the objective of this thesis to clarify this issue. For the objective of measuring gas parameters, comparison of two methods have shown that the experimental results obtained by Equation (7.5) is in good agreement with that by Equation (7.2) and (7.4), in the field strength below $90\,\mathrm{kV/cm}$. It is a strong prove of the experimental method.

We have decided that the gas parameters obtained from charge is the measurement results of the experiment, as the result is not interrupted by diffusion effect, and it is a well accepted method by other experiments.

As a conclusion, the data of Townsend coefficient is obtained with charge as a function of length of drift path which is discussed and plotted in Section 6.3.2.3. The data measured in Section 6.3.2 will be taken as the final experimental results.

Chapter 8

Conclusions and discussions

With the completion of the laser test facility, our research of methods for measuring the precise gas parameter in high electric field and atmospheric pressure therefore begun. Series of experiments are operated step by step. As the experiment progressed, the experimental methods are tested, verified and developed. Finally, the detector system that is most suitable for the measurement of gas parameters in timing RPC is constructed and the gas parameters are acquired.

The experimental observations are referred and cross-checked, and are also compared to calculations or to other researches as much as possible to guarantee that the correctness and precision of methods and results. In this section, the details of our observations will be discussed, including the detector performance, the process of avalanche signal and the gas parameters.

In this section, the experimental results will be discussed, in order to further develop the understanding the physical process behind the values.

The experiments with glass and ceramic RPC samples have shown that the electron drift velocity is in agreement with simulations for most situations, on the other hand, the effective Townsend coefficient is clearly below the predictions from simulations.

This phenomenon of reduction of effective Townsend coefficient has been discussed, and the existence of 'space charge effect' is a possible explanation. In this thesis, there are agreements and disagreements found between the experimental results and the simulation results.

8.1   Performance of RPC sample and real detectors

Our detectors are designed aiming at presenting the real RPCs. During our research, many practical methods and knowledges related to RPC operation can be realized. RPC is already a well developed technology, and our research results are quite fundamental, As a result, the observations can be compared to real phenomena in real RPCsto help understanding or explaining the performances of RPC detectors.

8.1.1 Charge Distribution and time resolution

In our case, the primary electrons are generated around the laser focus, although the number of primary electrons is still not very clear as described in Section 5.5, estimation can be made that the number of electrons is at least beyond 10 and below hundreds.

The beam waist of laser focus is in the order of $5\,\mu m$, the time variation from the spatial distribution is much smaller than common RPC. In our case, the charge deviation is so little that it follows a normal distribution, because of the well defined position of ionization.

Considering the above facts, the time resolution obtained from signals of laser test facility should be smaller than from a common RPC detector. From our experimental results in trigger RPC (Section 6.1) and timing RPC (Section 6.3.2), the obtained time resolution (σ resolution) of RPCs are:

- trigger RPC: Our measurement: $\approx 700\,ps$, common: $\approx 1\,ns$

- timing RPC: Our measurement: $\approx 20\,ps$, common: $\approx 50\,ps$

It can be concluded that our test results have shown better time resolution on the same magnitude, compared to similar on-site RPC detectors. The performance of our RPC with laser ionization method is comparable to the best time resolution obtained by MRPC detector which is also around 20 ps [104].

8.1.2 Field reduction and rate capability

8.1.2.1 The time constant

As is discussed in Section 3.2.5.3:

$$\tau_{real} = \rho \, \varepsilon_r \, \varepsilon_0 \ . \tag{8.1}$$

The resistivity of our float glass and ceramic is in the order of 1×10^{13} and $1 \times 10^9\,\Omega \cdot cm$, respectively. As the permittivity of the materials is 8 for float glass material and 12 for the ceramic material of the electrodes of RPC respectively. And it is known that $\varepsilon_0 = 8.85 \times 10^{-12}\,F/m = 8.85 \times 10^{-14}\,F/cm$. Then the time constant is 7.1 s and 1.62 ms

Our measurement of glass RPC has shown that the time constant of glass RPC is around 3 seconds, which is in the same order of magnitude with estimation. It has also been found that RPC with narrower gap has larger time constant than wider gas gap, this is also in agreement with the calculation in Equation (3.16).

8.1.2.2 The area of field reduction

For the ceramic RPC, as the rate capability is so high (in the order of $100\,Hz/cm^2$), the limitation of rate has become the purity of gas.

For the glass RPC, although the time constant is in the order of seconds, a typical value of rate capability of RPC detector with glass electronics is in the order of $1\,kHz/cm^2$. it is assumed and widely believed that the reduction range is very small [105].

The laser focus is fixed on a certain position, so that the rate capability in the unit of rate per area cannot be directly compared to our results. The experimental fact can be described as follows: when the avalanche is distributed randomly in a region, the rate capability is in the order of $1\,kHz/cm^2$; when the position of avalanche is fixed at an exact position with accuracy better than $1\,\mu m$, the rate capability is only about $0.3\,Hz$. As it is already measured in Section 5.4 that the width and length of laser focus is around 10 and $400\,\mu m$, assuming that the dimensions of final avalanche is the same dimensions as the laser focus, so that then the width of field reduction area is $10\,\mu m \times 400\,\mu m$.

Consider the rate capability of $1\,kHz/cm^2$, if the area is limited to $10\,\mu m \times 400\,\mu m$, then the rate capability is $0.04\,Hz$, which is only one magnitude of difference compared to experimental data of $0.3\,Hz$. Consider that the drift length of the experiments are approximately $0.1\,mm$, from the comparison, it can be concluded that the area where field reduction area of an avalanche is in the order of $10\,\mu m^2$.

For the ceramic RPC, as the rate effect is not observed, there are fewer information of the field reduction area. But the field reduction area should be the same as glass RPC, as the field reduction process happens with the smaller time scale in discussed Section 8.1.2 and the volume resistivity has no influence in the small scale process.

8.1.3   The influence of gas purity on RPC performance

In the test with ceramic RPC(II), when the laser repetition rate is up to $100\,Hz$, the charge of avalanche signals is not significantly reduced, but the streamer ratio rises rapidly. The streamer ratio when operated with $10\,Hz$ repetition rate is around 10% to 15% and independent from the signal charge; with the repetition rate of $100\,Hz$, the streamer ratio is approximately beyond 50%.

Because that the charge of avalanche signals are not reduced, the field has been fully recovered. The cause for increasing the streamer ratio may be the purity of gas. It can be assumed that an avalanche generate impurities on its position, and requires some time for diffusion. If the diffusion time is too short, the impurities will contribute to the streamer ratio greatly.

Still, it is rather a discovery than a research conclusion. It is not too much related to the main objectives of this thesis. It should be mentioned because of its practical value that it is related to the upper limit of RPC rate capability.

8.1.4   Ageing effect

Ageing effect is also an important issue in RPC operation. Usually, a RPC detector is required to work continuously for several years without degradation in the performance. When the ageing effect appears, or called 'aged', the dark current will be much higher and all the parameters of RPC such as time resolution, streamer ratio, efficiency, spatial resolution will become worse.

Ageing test is one of the most important performance test. There are a lot of ageing test results for different RPCs and the results differs a lot depending on different conditions which means that there are different mechanism in the ageing in RPC.

8.1.4.1   How we find ageing effect

Although we did not intend to make an investigation of ageing effect in our RPC detector, the ageing effect does not appear in a very long period of experiment, but occurs dramatically fast in the test with very high field and very high streamer ratio.

As described in Section 6.3.2.3, before the field strength is set to 120 kV/cm, from all the operated the experiment for ceramic RPC(II) and with 10 Hz repetition rate, the streamer ratio is always around $10 - 15\%$.

When the field strength is increased from 110 kV/cm to 120 kV/cm, the streamer ratio becomes about 80%, the detector is working at streamer mode now. The avalanche signals becomes very low in this situation and the measurement of gas parameters is nearly impossible.

In order to observe the performance, a full scan of waveforms on different positions. is still operated The test was finished within 10 minutes. After the test, the voltage is reduced to 100 kV/cm. In this situation, a larger dark current is observed.

The unusual performances have shown that the detector is perhaps aged. Then the voltage is set to about 70 kV/cm to avoid dark current and placed the detector for about 40 hours to test that whether it can recover by time. Then, high voltage supply is increased again, but the dark current remains high.

More ways are taken into consideration about how to recover the performance of RPC detector. As reported in [87], an inversion of electric field will result in a recover of surface resistance, this method is worth trying although we are having different kind of ageing effect. We reversed the polarity of electric field so that the anode and cathode electrodes are exchanged, however the dark current is still high. Now we confirmed that there is a non-recoverable ageing effect in our RPC.

The gas box is opened and electrodes are dismounted. A white layer has covered the anode, and the cathode is covered by a much thinner layer. The white layers are not totally flat, they actually formed of many small 'white dots', with several 'black dots' within them. This is very similar with the ageing effect introduced in [1, 106].

8.1.4.2   The white layer as the ageing effect

As the ageing effect appears dramatically in a well-controlled situation in a very short period, the reason of RPC ageing must be connected to the situation. In our case, field strength is 120 kV/cm, streamer ratio is around 80% and stain of 'white layer' appears soon. It can be assumed that the relations between them is one of the following:

- The white stain is caused by some effect in an avalanche of very high charge. The stain is the reason of streamers and dark current.

- The white stain is caused by huge streamers developed from avalanches with high charge in high electric field. The stain then becomes the cause of streamers and dark current.

No matter which one is the physical process, the white stain certainly decrease the performance of the detector.

In our case the white layer of stain is found on both sides, but the thickness is totally different, a possible explanation is that the stain will only be generated on the anode; when we reversed

Figure 8.1: The picture of aged electrodes. The bottom electrode is anode, top electrode is cathode.

the direction of electric field, the white layer is generated on the cathode acting as the anode now. Another possible explanation is that there are two different ageing effect on the cathode and anode that both generates stain.

We put the two electrodes under the Field Emission Scanning Electron Microscope(FE-SEM), and made investigation of elements with Energy-Dispersive X-ray Spectroscopy(EDX) method.

The surface scans have shown that the stain on anode and cathode has different pattern, as shown in Figure 8.2. Both surfaces are crude, we cannot really tell it is only stain on the surface, or the electrode surface is already damaged.

From the EDX analysis, the spectrum has shown that the white stain on the surface is Fluorine.

8.1.4.3   Conclusion

From the unexpected ageing effect, similar phenomena compared to former experiments are observed.

In this kind of ageing effect, white stain consist of Fluorine is generated on the surface of anode (perhaps together with cathode), and result in a loss of the performance of RPC detector like increasing of dark current and streamer ratio, decreasing of time resolution and efficiency.

The dark current occurs by edge discharge on the crude surface of white stain. The continuous discharges will result in a decrease of field strength reducing the signals, so that the efficiency and time resolution becomes worse. At the same time, as described in Section 8.1.3, the continuous avalanches or streamer will make the gas contaminated so that the streamer ratio becomes high. Then the streamers will amplify the generation of white dots of stain again.

There are still unclear things in the ageing effect, because we only obtain the results from a coincidence occurred in the middle of an experiment, and before we open the detector, we

(i) Anode, larger scale

(ii) Anode, smaller scale

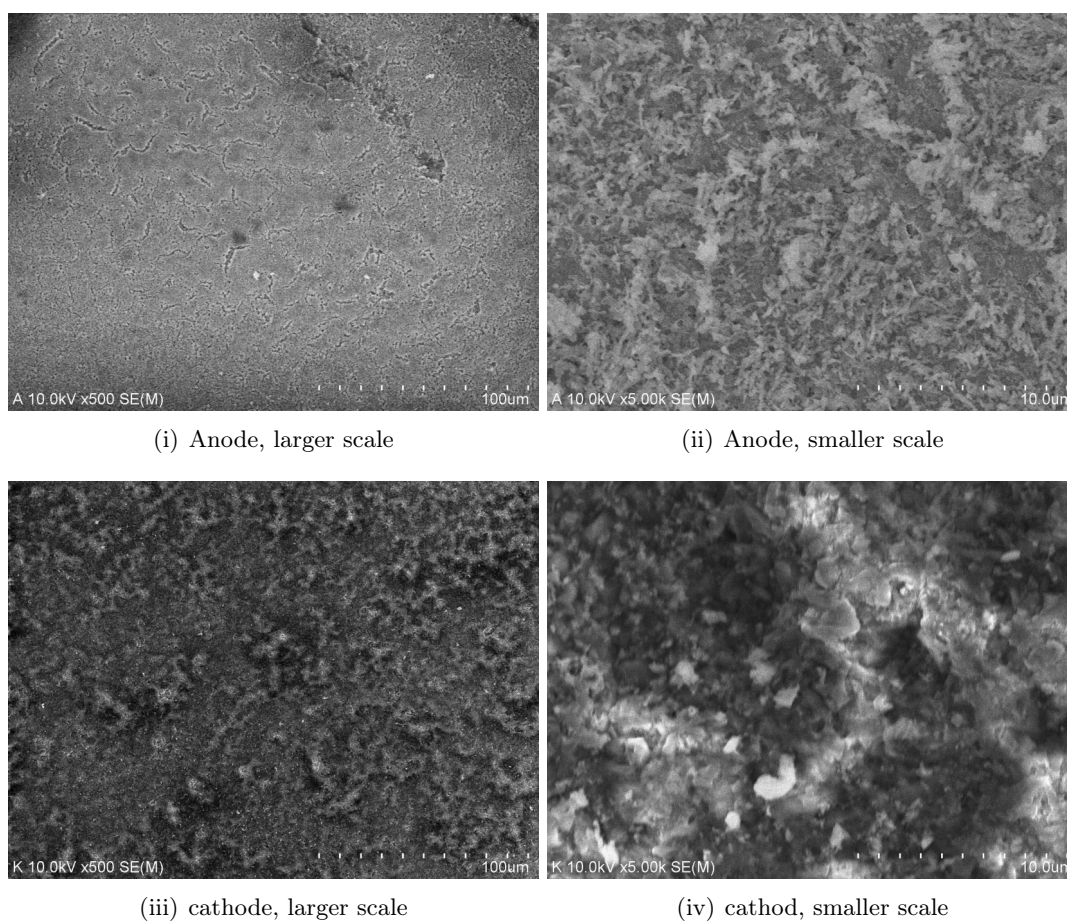(iii) cathode, larger scale

(iv) cathod, smaller scale

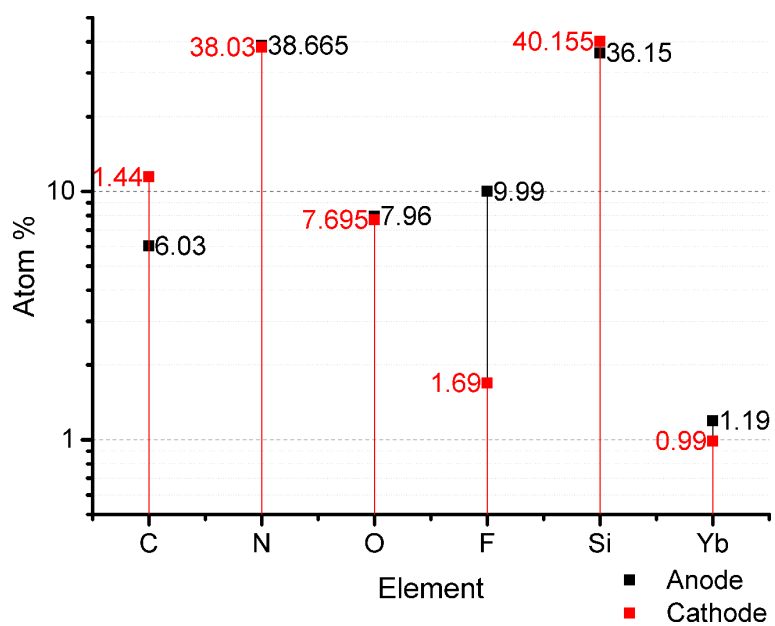Figure 8.2: The surface of electrodes scanned by FE-SEM.

Figure 8.3: The elemental analysis by EDX method. The ratio is uniformed. Only the Fluorine element is of great difference.

reverse the field strength so that there is a doubt that whether the white stain on the cathode is generated together with the stain on the anode, or it is generated because we reverse the field.

For further research, a more systematic experiment is required. It is possible on our laser test facility because we have known that how to generate the white dots or layer. This is not related to the objective of this thesis.

8.1.5   Dark current or breakdown

8.1.5.1   For glass electrodes

Many tests are operated in the field strength of glass trigger RPC. From the experimental experiences, the breakdown of detector never occurs. The conclusion is that it is very hard to make a breakthrough in RPCs with glass electrodes, trigger RPC field strength and normal RPC gas. In some tests, the laser rate is increased to produce more impurities, but no breakthrough is observed.

As a conclusion, the breakdown performance is better than normal RPC detectors. Compared to normal detectors, the RPC samples are smaller and the experimental condition is more simple.

8.1.5.2   For low resistivity electrodes

Comparing the performance of ceramic RPC(I) and ceramic RPC(II), it can be observed that the dark current is significantly reduced by rounding the edge of the electrodes. As a conclusion, when the resistivity of electrodes becomes lower, more efforts should be taken to prevent the discharges on the edges of electrodes.

8.2   Space charge effect and measured eff. Townsend coefficient

8.2.1   Existing models

As is introduced in Section 3.3.2, the space charge effect is used to explain that, the number of electrons calculated from exponential growth is several orders of magnitude larger than the measurement results.

Space charge effect is caused by the electrons and ions in the avalanches. Space charge field will reduce the gas gain to limit the number of electrons, therefore prevent the development of streamer signal. There are many different models for explanation of space-charge effect (for example, in [73], and models in [107]).

In [73], detailed 1D to 3D models are built to make a simulation of effective charge effect. The signal process as a function of time has shown that the signal will follow exponential growth at the beginning, and then reaches a saturation region. As shown in Figure 8.4, the avalanche first grows as an exponential function, and then saturation effect appears and the growth is limited.
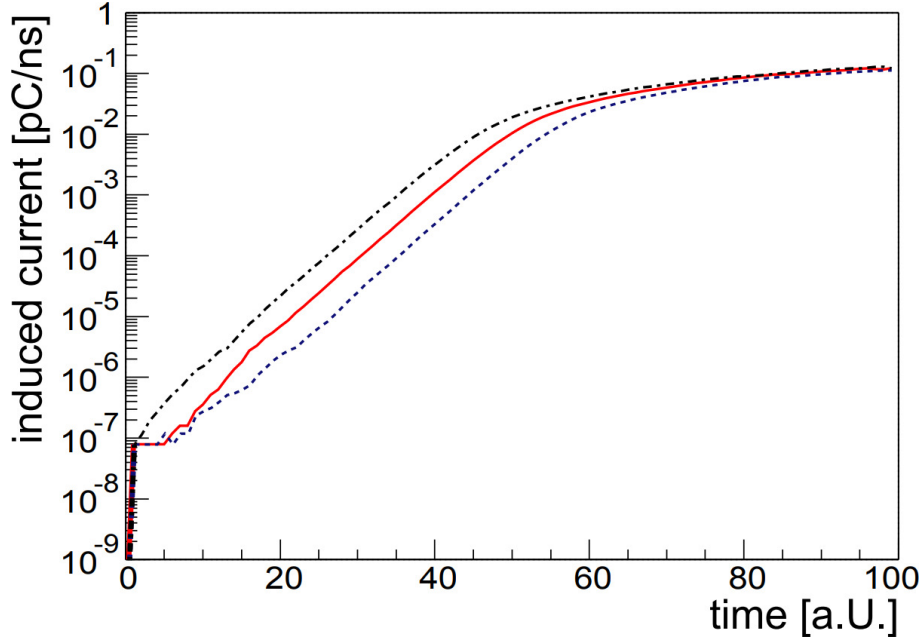
Figure 8.4: Simulation result of a signal process from [73]. The time step is 14 ps. The space charge effect is applied. Saturation effect is observed.

In [107], it is assumed that the effective Townsend coefficient follows the function:

$$\alpha(q_e) = \alpha_0 \frac{q_{sat}}{q_e + q_{sat}} , \qquad (8.2)$$

where q_e is the number of electrons and q_{sat} is the saturation number of electrons. The effective Townsend coefficient remains undisturbed for number of electrons far less than saturation number of electrons, and tends to 0 when much larger than the saturation number of electrons.

From the existing models of space-charge effect, despite the differences in methods and models, it can concluded that the space charge only appears after a certain saturation number of electrons. When the number of electrons is more than one order of magnitude smaller than the saturation charge, the exponential growth of signal follows Equation (7.2).

8.2.2   Comparison to measurement results

The measurement results of signal charge in dependence of length of drift path has been presented in Figure 6.15. In order to calculate the number of electrons, as is discussed in Section 3.2.3.3, the total charge Q_{total} follows:

$$Q_{total} = Q(\alpha - \eta)d , \qquad (8.3)$$

where Q is the induced signal, α is the first Townsend coefficient, η is the attachment coefficient, d is the total drift length. The data plotted in logarithmic scale is shown in Figure 8.5.

From the figure, it can be seen that the number of electrons follows exponential growth as a function of distance from ionization to anode when the number of electrons is between 10^6 and 10^7. The saturation effect occurs when the number of electrons is beyond 10^7.
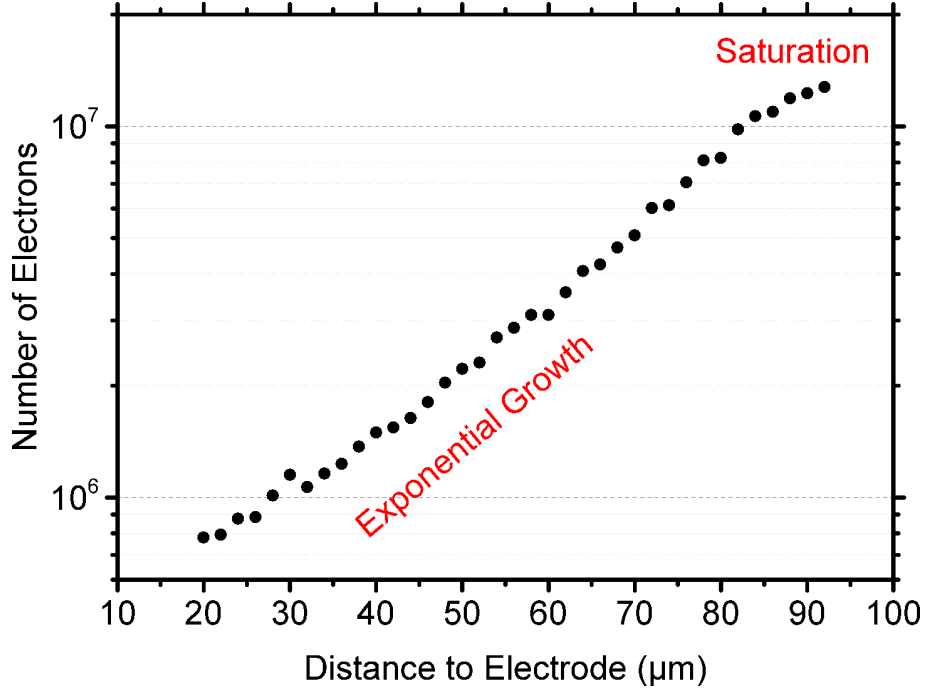
Figure 8.5: The number of electrons as a function of distance to anode. The effective Townsend coefficient calculated from the exponential region is $472\,\mathrm{cm}^{-1}$.

The effective Townsend coefficient for the smaller number of electrons can be calculated from Figure 7.4. According to Equation (3.12), the number of electrons follows:

$$N_e(t) = I_{induced}(t) \frac{d}{e\,v_{drift}} \; , \tag{8.4}$$

where $I_{induced}(t)$ is the current at time t, d is the gap width and v_{drift} is the drift velocity. The data is plotted in Figure 8.6.

It can be concluded that from the electron number of 3×10^4 to approximately 10^6, the number of electrons follows exponential growth.

As a conclusion, from the measurement results of HZDR laser test facility, the saturation effect is observed. The saturation effect appears after a certain threshold, which is in agreement with physical models. The space charge effect has no influence on the experimental result of effective Townsend coefficient and electron drift velocity, as the gas parameters are obtained with non-saturation signals.

8.3   Summary

8.3.1   Comparison of our results to other works

The electron drift velocity measured from HZDR test facility with ceramic RPC(II) has shown agreement in the electric fields from $70\,\mathrm{kV/cm}$ to $106\,\mathrm{kV/cm}$, as shown in Figure 6.17. The
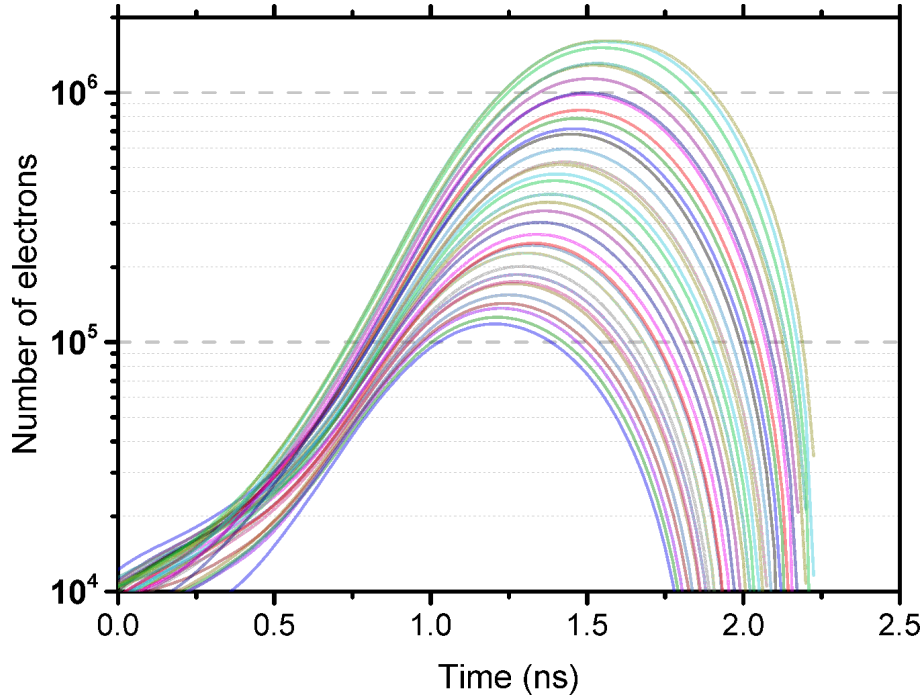
Figure 8.6: The number of electrons within the signal process. As is introduced in Section 7.2.3, the effective Townsend coefficient in the exponential region is around $30\,\mathrm{mm}^{-1}$. No saturation effect can be observed from the figure, as the reduction of signal is because the electrons are absorbed by the anode.

agreements have shown that the objective of testing the drift velocity is achieved. On the value of $110\,\mathrm{kV/cm}$, the drift velocity is lower than simulation, however it has a clear connection to the measurement of Townsend coefficient that a plateau is reached.

A comparison of the effective Townsend coefficient between our measurement data and other data from simulations and from other methods is presented. We put together our experimental result, and some of the most comparable results that related to our experiment of gas parameters in Figure 8.7.

- **W. Riegler's simulation [64].** A integrated description of detector physics, signal process and gas parameters is introduced in this work. The method to accumulate gas parameters with Monte Carlo simulation is developed, and the data is provided. We take the data of effective Townsend coefficient as a reference.

- **G. Chiodini's data [6].** This measurement is operated for trigger RPC for the purpose of measuring the gas parameters for ATLAS RPC. This measurement is operated at atmospheric pressure using UV laser as the ionization source.

- **J. de Urquijo's data [4].** This measurement is operated under reduced gas pressure using Equation (3.27). The measurement is operated with pure R134a, and it is a good reference to compare with.

- **HZDR data.** HZDR measurement is operated with laser test facility. The rate effect is avoided by using low resistivity ceramic RPC. The effective Townsend coefficient is measured in room temperature, atmospheric pressure. The measurement of trigger RPC and timing RPC are presented respectively. The error bar of the effective Townsend coefficient is set 10%, according to the fact that the measurement data of Townsend coefficient varies
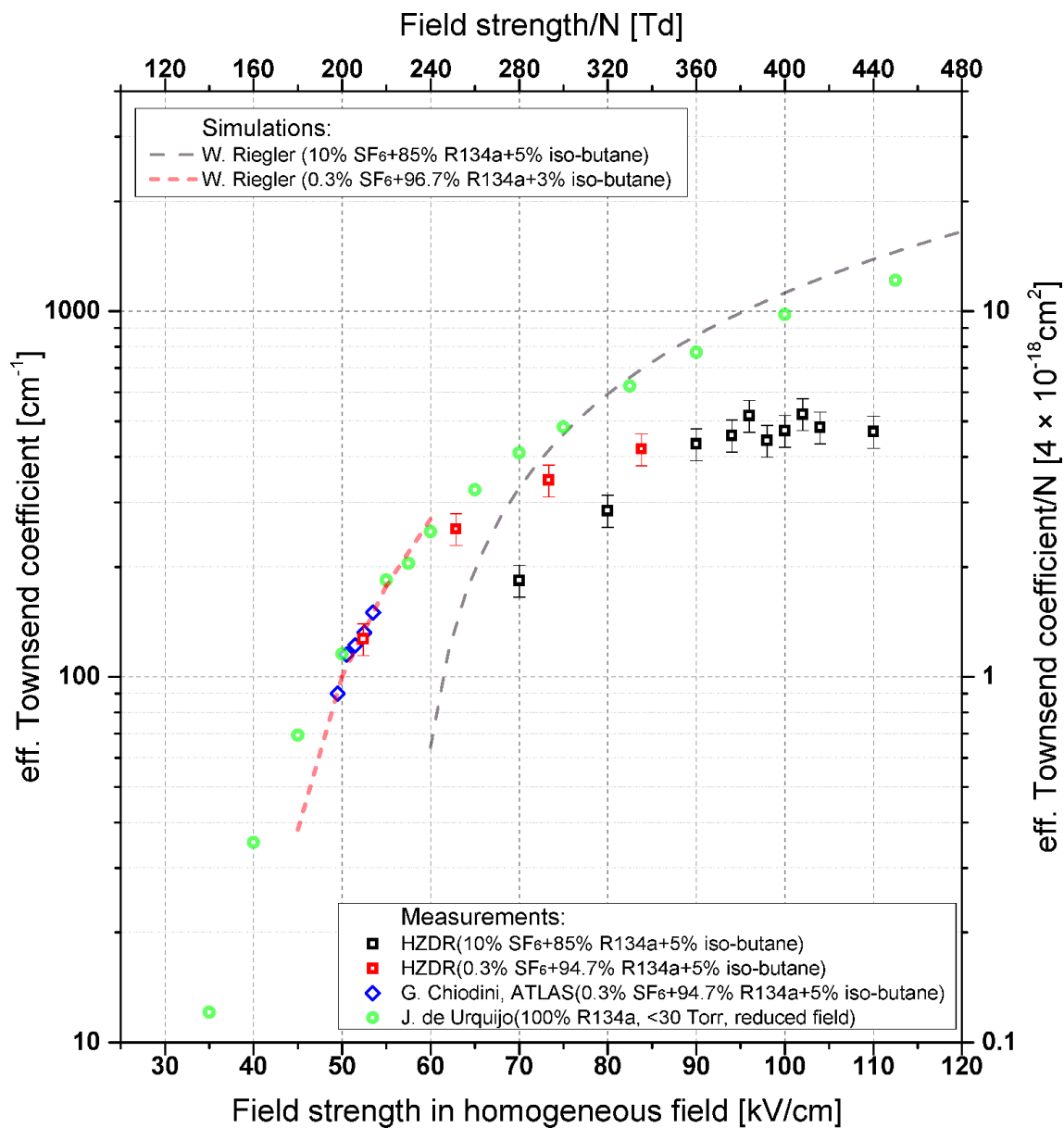
Figure 8.7: The comparison of effective Townsend coefficient data with different experiments and simulations.

about 3% depending on data selection, and the measurement data differs about 3% when we test the same parameter in a different run, and the systematic error also cannot be ignored. So that if the error bar of 10% is already an over estimation of total error.

The comparison from the simulation and measurement data has shown varied performances with different ranges of electric field strengths according to the data shown in Figure 8.7, Figure 6.16 and Figure 6.7(iii).

8.3.1.0.1 At the field strength of trigger RPC. When the field strength is about $50 \, \text{kV/cm}$ (about $200 \, \text{Td}$ as reduced field strength), the simulation result and measurement results are comparable. The measurement of drift velocity compared to existing data is below 20%, and accumulated effective Townsend coefficient is in agreement with existing data. This is the proof that the test method and facility has achieved the requirements for measurement of gas parameters.

8.3.1.0.2 In the field range between trigger RPC and timing RPC From $70 \, \text{kV/cm}$ to around $95 \, \text{kV/cm}$, effective Townsend coefficient of two gas mixtures have been measured. The drift velocity is not discussed as the systematic difficulty of data acquisition would be solved until the measurements with timing RPC range. Further details are described in Appendix B.

For the trigger RPC gas, a gradually variation from experimental data is observed as the field strength is increased. It possibly indicates that a mechanism that limits the signal amplification begins to appear in this region of field strength.

For timing RPC gas, on the first possible measurement point at the field strength of $70 \, \text{kV/cm}$ in figure8.7, the measurement data is only about half of the value compared to the value obtained by pure R134a in reduced field, and also only about two third of the value of simulation. In this range, the measurement data from HZDR is approximately in a parallel relation to the other two results, about half of the value from simulation or obtained in pure R134a in reduced field.

As is discussed in Section 7.2.3 and Section 8.2, the reduction of effective Townsend coefficient is not from diffusion or space-charge effect. The mechanism is not yet contained in current understanding of RPC detector physics.

8.3.1.0.3 At the field strength of timing RPC From $90 \, \text{kV/cm}$ to $110 \, \text{kV/cm}$, the drift velocity is in agreement with simulation results. However, in this region, the measurement value of Townsend coefficient stops growing, and performs like a 'plateau' until the breakdown of RPC at $120 \, \text{V/cm}$.

The mechanism of the 'plateau' is also not clear. It can be explained the same phenomenon as discussed in Section 8.3.1.0.2, or a different mechanism of reduction of gas parameters, or due to the limits of experimental devices. Further understandings are required.

8.3.2 Comparison to performances in real RPC

With the well calibrated high precision laser test facility, a lot of researches related to performances of RPC detector has been operated. Experimental results have shown agreements in

nearly all the aspects of RPC detectors, including the time resolution, rate capability, avalanche development, ageing effect and streamers.

Especially, the experimental results of gas parameters obtained from the experiments at the field strength of timing RPC in atmospheric pressure has shown that the assumption of very strong space-charge effect is not necessary due to a smaller realistic value of effective Townsend coefficient. The experimental results are useful for extending the knowledges of RPC avalanche process.

For the research of eco-friendly alternative gas for timing RPC, both accurate values of gas parameters and better understandings of avalanches and streamers are required. The results in this thesis can contribute to both of the two objectives.

Appendices

Appendix A

Paschen's law and Brunner's equation

The Townsend coefficient for the same gas at different pressures and on different electric fields, can be determined by the equation [72]:

$$\alpha_{eff}/p = A\,e^{-B/(E/p)}\ ,\tag{A.1}$$

where p is the pressure, E is the field strength, A is a parameter related to the saturation ionization in the gas at a certain E/p, B is a parameter related to excitation and ionization energies. A and B are usually determined in experimental research.

Considering that when the positive ions have reached the cathodes and secondary electrons are emitted from cathodes and start new avalanches in the gas gap, the total discharge current i is given by [108]:

$$i = i_0\,\frac{e^{\alpha_{eff}\,d}}{1 - \gamma\,[e^{\alpha_{eff}\,d} - 1]}\ ,\tag{A.2}$$

where i_0 is the initial current of electrons leaving the cathode, d is the distance from anode to cathode, γ is the effective secondary emission coefficient for the cathode. Each positive ion will result in γ electrons when hitting the cathode. Then the requirement for having a self sustaining discharge is given by [109]:

$$\gamma\,[e^{\alpha_{eff}\,d} - 1] \geqslant 1\ .\tag{A.3}$$

Consider Equation (A.3) and (3.27), define the breakdown voltage by U_b and the breakdown field strength by E_b, and the distance from anode to cathode is d, we have the Paschen's law:

$$U_b = E_b\,d = \frac{B\,p\,d}{ln\left(\frac{A\,p\,d}{ln(1+1/\gamma)}\right)}\ .\tag{A.4}$$

Due to the assumption that the equations are valid in the full range of electric field of RPC detectors, measurements of gas parameters under reduced pressure and reduced electric field is operated.

From the experimental results in this work in Chapter 7.2.3.2, we suspect that the application of the equations is conditional.

Appendix B

The detector samples and electronic system

(In this chapter, the design of detector samples and upgrades of electronic system are presented. The drift tube detector is for calibration use. The RPCs have two generations, RPC(I) with glass and ceramic electrodes and RPC(II) with ceramic electrodes.

For the drift tube and RPC(I), signals are readout from the HV cable by a signal-splitter box; for ceramic RPC(II), the signal has an individual readout.
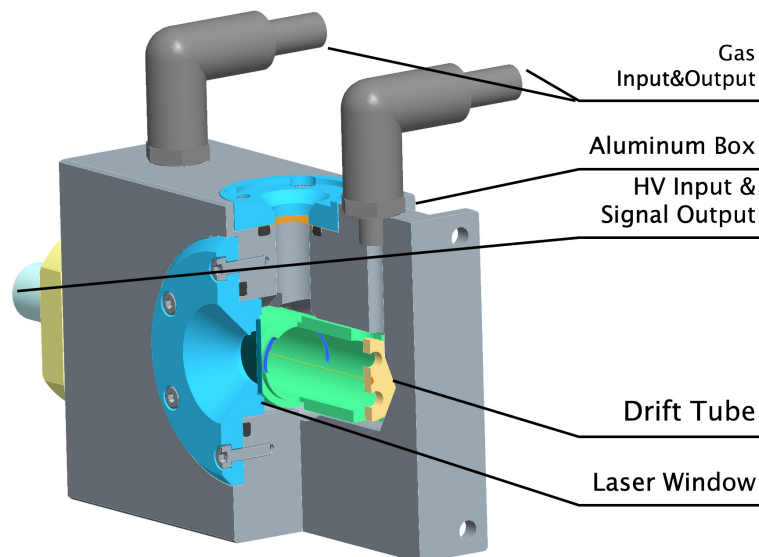
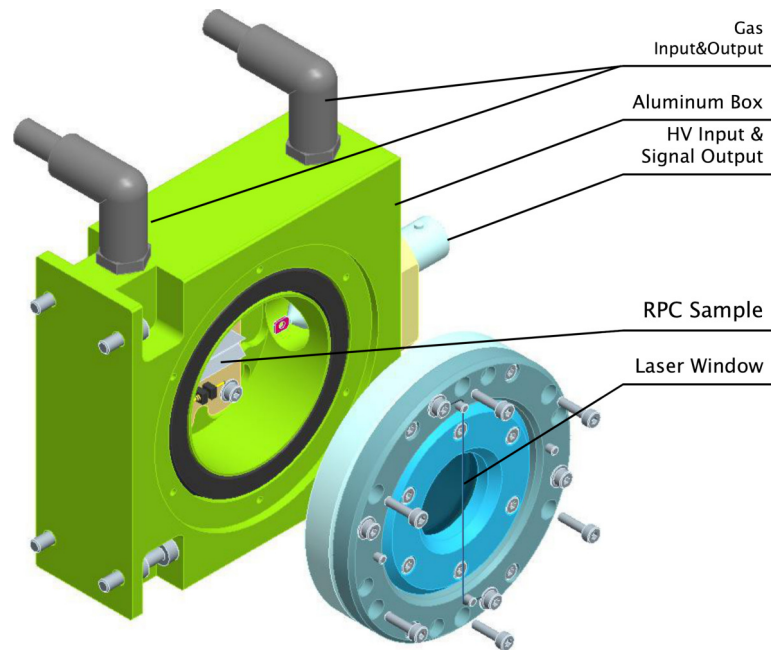

Figure B.1: Design of drift tube sample.
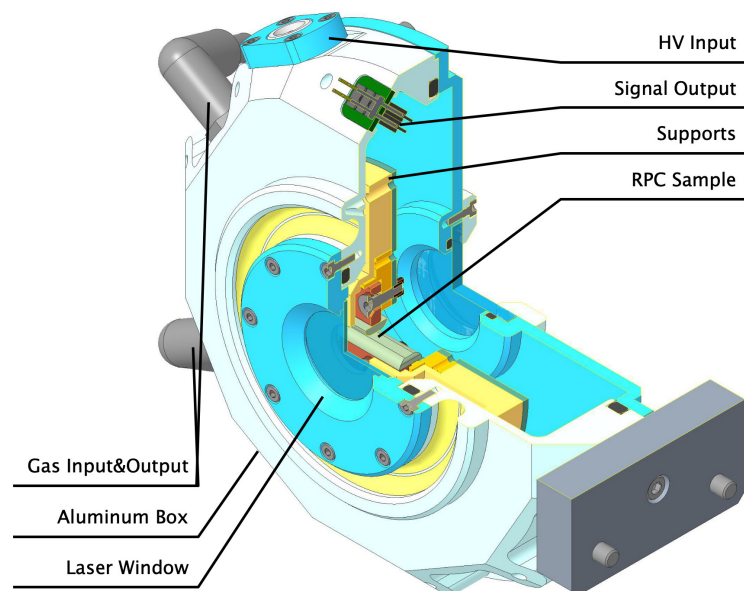
Figure B.2: Design of RPC(I).

Figure B.3: Design of RPC(II).

Appendix C

Programs for systematic remote experiments

The Labview automation program plays a very important role in the laser test facility, not only because it is a remote way of operating experiments, but because it simplifies the tests into simple step. With the program, a test can be performed by pre-set parameters and chick 'begin' button. In most of our measurements, the number of measurement points is usually decades to hundreds; at each position, statistical number of events is required.

An automatic program is a good replacement of manpower. It can run continuously without time gap so that it is time saving. Also, as the experimental data is huge, the program is more reliable than human.

C.1   Experiments without automatic programs

We should first consider the situation without the automatic program. Such measurements were operated several times, but each one of them takes a very long time, because a common experiment requires a long time of repetitive work. Here we present an example of how to make a measurement with the RPC detector sample without automatic program:

1 Turn on the laser generator and make proper alignment of optic system to make sure the laser focus is in good shape and the laser energy is well limited to a certain value.

2 Arrange all the sensors, instruments and the detector, then check the status to make sure all devices are working. Especially, the oscilloscope need to be set to analysis mode and be programmed to measure the time over threshold and charge, therefore the histogram and statistic value of data are obtained.

3 Manually adjust the position (by default control program provided by OWIS) to place the laser beam through the gas gap of RPC. In this step, we set the position of detector while looking at the laser intensity measured from the laser sensor behind the detector, until the laser sensor shows the laser energy is not zero.

4 Continue to measure the laser with small step length, perpendicular to the direction of laser beam. A plateau of laser pulse energy will appear at different positions, and as the position continue to change, the value of laser energy goes to zero again. The plateau should contain several points, to provide the information of the relative position of focus inside gas gap.

5 Increase the supply voltage of RPC detector, adjust the oscilloscope to display the waveform of reference and RPC signal properly.

6 Move the position of RPC along the direction of laser beam, measure the laser energy and charge of RPC signal roughly, and find the position when the laser focus is placed in the center.

7 Reduce the supply high voltage to zero, repeat the measurement in Step 4 especially on the edge of plateau to make the precise calibration of laser focus position.

In the above procedures, Steps 3, 4, 6 and 7 are very time consuming and are kind of repetitive work. As a result, it is difficult to make a precise calibration to investigate the position of focus. On the other hand, after the preparation is finished, the experimental procedure is also a kind of repetitive work:

8 Move the detector to a certain position where the distance from laser focus and anode is d_1.

9 Refresh the oscilloscope to clear all the waveforms in memory, and begin to acquire new waveforms.

10 Wait for some time until the number of waveforms has already reached the requirement of statistics. As the analysis mode of oscilloscope will calculate the mean and variation of time difference of time over threshold and reference time, the value will be shown on the screen, and what the researcher do is to record it. If we are working with glass RPC sample with the laser rate of 2 Hz, and 1000 waveforms are required for statistics, it will take eight minutes for each one position.

11 Move to position d_2 and repeat the measurement from Step 9 until all the positions are measured.

The process of experiments is also time consuming. It requires the researcher to set value and record value continuously. Even we can ignore the difficulty in time and attention, there is another problem that can not be neglected: we only have the value of time and charge according to the pre-set formulas and parameters in oscilloscope, we cannot record the original waveforms. Those facts have limited the possibility of further investigation of waveforms.

C.2   Objectives and conceptional design

Because of the above reasons, we have developed the programs in order to reduce the time, simplify the process and implement the storage functions for the system, so that the signal storage and signal analysis are independent. Consider all the devices in the laser test facility, our objectives for the programs are as follows:

Connecting devices:

1 Oscilloscope. The oscilloscope is used in all the experiments that the signal from the detector is acquired. The oscilloscope has a lot of built-in functions for waveform analysis, which is also helpful in calibrations.

2 Laser sensor. In laser intensity test, the laser sensor is placed behind the blade; In detector test, the laser sensor is placed behind the detector to make sure that the laser is not in touch with the detector edges, anodes or electrodes.

3 Moving stage. The blade or detector is implemented on the moving stage. In most of the experiments, the moving stage plays an important role.

4 Rotation stage. A 'round continuously density filter' is implemented on the rotation stage to adjust the laser intensity. In most of the experiments, the filter is fixed. It is active in the experiments related to laser intensity.

Functions:

1 Checking the statues of devices, checking connections and communications.

2 Allow input of parameters by user and transfer the settings to devices; control the devices both automatically and manually; read the data from the devices.

3 In the beginning of the test, there should be a function to make a plan of scanning. The user will determine several points, whether they are distributed in a line or in a section. In the end of this process, a chart with all the positions to scan will saved.

4 In the experimental process, the program will read the positions from the chart one after another, and control the moving stage to the position. On each position, data acquisition process will be activated and the waveforms of data will be stored temporarily. When the process is finished, the program will read the next line in the chart and make the measurement in the next position.

5 After all the positions are measured, one or both of the following functions should be activated: to analysis or to store the original waveform data. The results of analysis are better to be visible, so that it is easier for understanding the measurement results.

6 The stored data can be analysed individually by another program. This program should be able to operate data analysis, including the time over threshold, charge and amplitude. The settings and parameters such as threshold, time window should be opened to the user to perform precise analysis. Based on the data, the gas parameters can be calculated.

With a program that contains the above functions, the efficiency of experiment will be much higher. The program should be an integration of all the functions. A conceptional design of the program is shown in Figure C.1. The devices are initialized in the beginning of the program. Then the user will select the experimental mode, such as deciding which parameter to measure, and which axis to scan, etc. The program will then call the necessary instruments, and pre-set all parameters. The program will then proceed into a loop, in which the program will set the moving devices to a position written in the process table and then make the measurement in this position, store the measurement data and then move to next position.

For the experimental process described in Section C.1, many steps are much simplified:

1 The alignment of laser generation system should also be manually done, but the detection and setting of laser energy can be operated on PC.
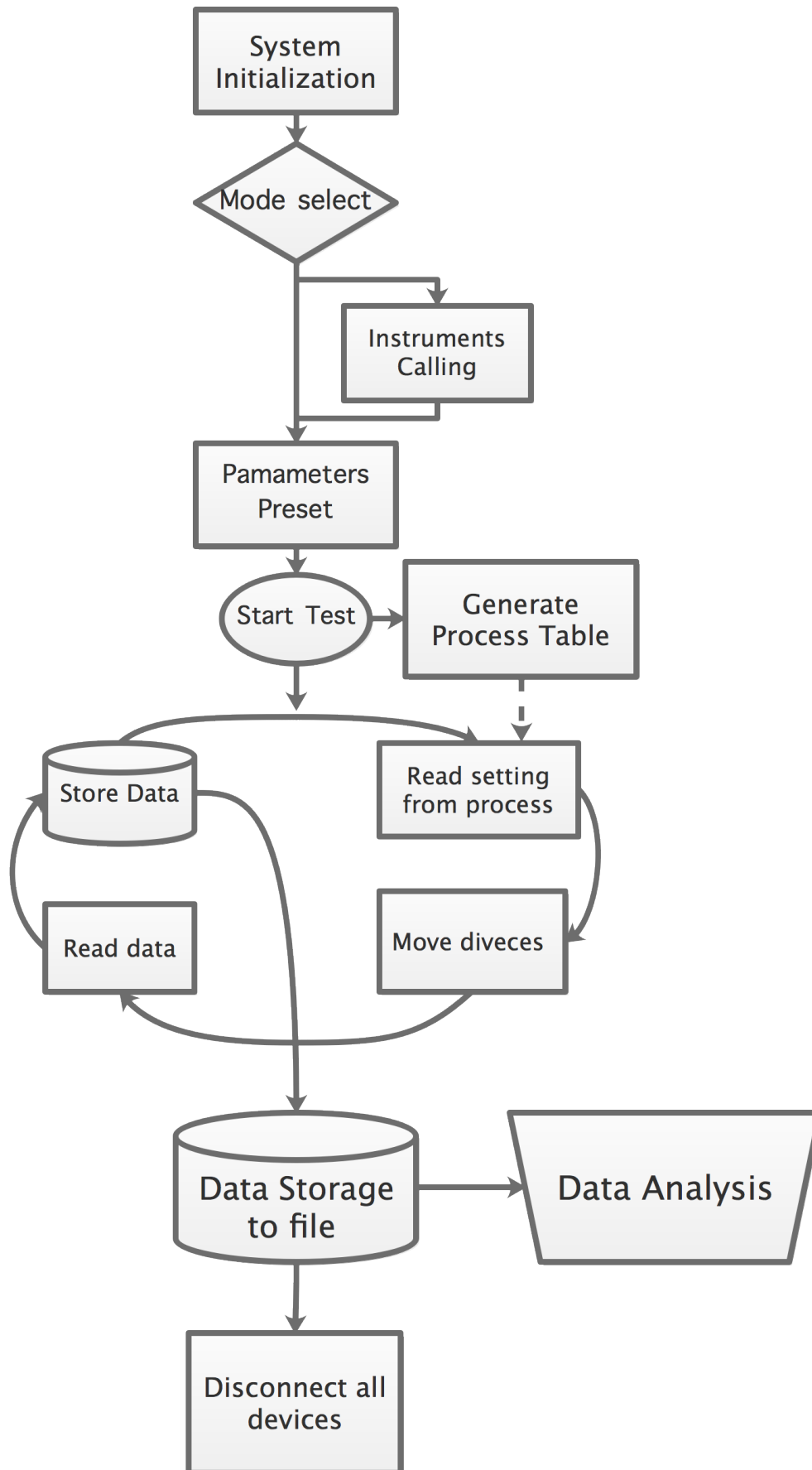
Figure C.1: The conceptional design of the programs for automation.

2 The connection of devices is still manual, but the communication can be checked with program, and by reading the saved working parameters and settings, the system can be prepared much faster.

3-7 The linear scanning is now operated by program. What we only need to do is to give the commands in the preparation stage, and wait until it is finished.

9 Now the program will record the waveform data.

10 With the programs, although it still takes time, but it does not require a researcher to sit aside. This allows us to make experiments over nights.

We have chosen Labview for our programming as Labview is a visual programming environment with powerful functions for communication to instruments. The development time is short and the modification of program is easier. Few program details need to be concerned.

C.3 Structure of program

Many scripts are developed and packaged as functions for free calling. Several subroutines are developed for specific experimental tasks. Based on the functions and subroutines, five executable programs are developed aiming at different types of experimental tasks.

C.3.1 Instrumental Interface

Programs for the instruments are developed first. Each package contains input and output scripts, and other necessary control or communication functions.

1 Oscilloscope: Initialization, shut down, mode select, channel activation/deactivation, parameters set, readout of waveforms from multiple channel.

2 Laser sensor: Initialization, shut down, range select, readout of laser pulse energy and frequency, high energy warning.

3 Moving stage:Initialization, shut down, reading the current position, moving to new position. Other parameters like defining the position of zero point, moving speed is not set in the programs.

4 Rotation stage:Initialization, shut down, reading the current angle, moving to new angle. Zero angle and rotating speed is not set in the programs.

C.3.2 Basic operating functions

In order to achieve the experimental objectives, a lot of scripts are written, including:

- Calculation. A lot of numbers and arrays will be generated and calculated during the program. Especially, large array contains thousands of data is often dealt with, so that many scripts are related to array.

- Logical and process control. Conditional judgement is always required in the programs.

- Storage and read. According to different targets, we store simple data, analyzed data and step chart in binary files, and original waveforms which has huge size in .tdms file provided in Labview. Especially, to limit the memory occupation while writing and reading .tdms file, special efforts should be taken.

- Writing and reading of step chart. A step chart is the list of positions to scan in an experiment. In most of our experiments, the positions are distributed evenly along a line, or along parallel lines in a Section The user need to set the start position, end position and step number for each dimensions, the chart will be generated. If we would like to scan a non-evenly geometry, we can also use additional scripts to write the chart.

- Waveform analysis. We use the same waveform analysis scripts for real-time analysis and individual analysis. The time, charge and amplitude of signal will be investigated for a signal.

These functions are placed in different classes and be embedded in all the subroutines and main programs. We have wrapped the scripts as much as possible so that different programs can share the scripts well to keep the program easy to understand and maintain.

C.3.3   Subroutine

A subroutine is usually called when we want to operate a specific job. Subroutine is between basic scripts and main program: it usually operate a simple job and be called as a process by the main program, but it also calls a lot of basic scripts with many adjustable input parameters. The subroutines can be executed just like a main program, or be called.

We have the following subroutines:

- Position management. To control the movement of moving stages in a simple, save and precise way.

- Laser sensor management. To auto adjust the working mode and range of laser sensor and give information to the program.

- Step chart management. Write different types of step chart in a simple way.

- Waveform readout. To connect to the oscilloscope and transfer the waveform into the program and make analysis or store.

- Waveform storage. Similar to above subroutine, but store the waveform in .tdms file instead of analyse them.

- Waveform analysis. A subroutine which makes all the analysis work.

- Gas parameter calculation. The analyzed data are concluded, and the effective Townsend coefficient and the drift velocity are calculated. This subroutine is often operated as an individual program.

We don't want to go into detail of above subroutines here as some of them are similar to that are already described in Section C.3.2, and the waveform analysis will be shown in Section C.4. We only take 'Waveform readout' subroutine as an example. The process is shown in Figure C.2.
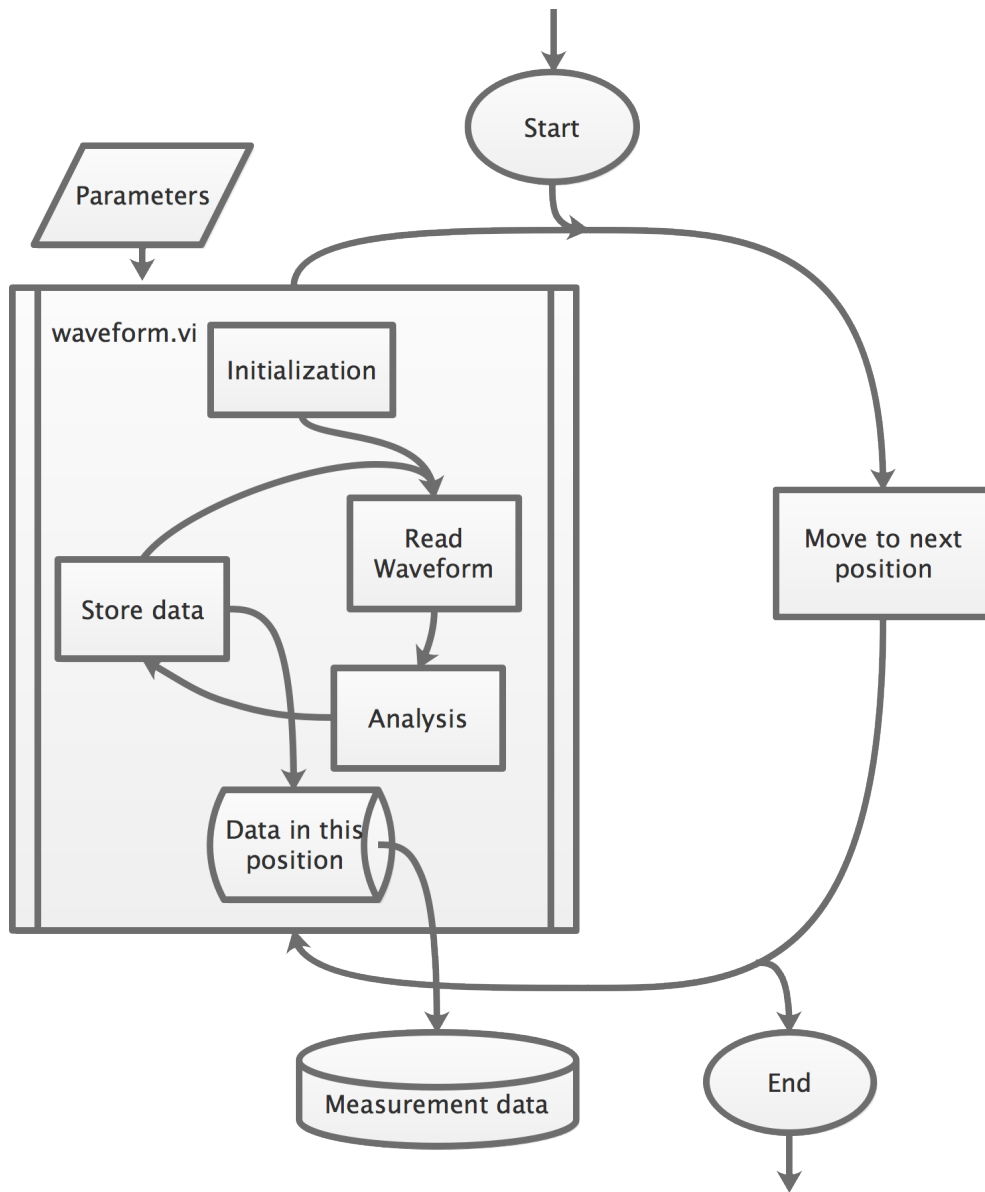
Figure C.2: The sketch map of subroutine 'waveform.vi'.

The name of the subroutine is 'waveform.vi'. This subroutine is for continuously acquisition of waveforms on a fixed position, while analyse the time, charge and amplitude of the waveforms, then store the result to binary file. It should contain start, shut-down, parameter input and output; the sub-programs called in this subroutine is oscilloscope subroutines, logical, process control, waveform analysis, read/write, array calculations.

It is executed in the following process:

1 The main program calls 'waveform.vi', and transfer the necessary parameters including number of waveforms N, initial settings, etc.

2 'waveform.vi' transfer the parameters to the oscilloscope and start waveform acquisition. Initialization and check of oscilloscope is already done by main program, if not, the subroutine will do it.

3 A loop begins in 'waveform.vi' to acquire waveforms until the number reaches N. Analysis of waveforms is performed at the same time, and the data is written into memory.

4 When the number reaches N, the oscilloscope is paused. After a very short time of analysing the last waveform, the data in memory will be saved into binary file. 'waveform.vi' will be terminated and tell the main program to continue.

5 Main program will move on to next position and activate 'waveform.vi' again until finished.

From the example, we can see that there is not a clear boundary between subroutine and main program, subroutine also calls other subroutines. It is an integration of multiple scripts for a certain purpose.

C.3.4   Main program

The main program is executable program directly used in experiments. It is designed and integrated for the aiming at operating a measurement from the beginning to the end, to minimum the experimental process and ensure the reliability. We would like to be able to achieve any specific experimental targets within one main program.

The main program is also the user interface, so that it requires a lot of initial parameters. We set all the parameters to a proper default value, and open the parameter to user for changing the parameters any time. In most of the experiments, we don't need to concentrate on the parameters.

Five different main programs are carried out according to our practical need of experiments:

- Position scanning of laser. This program connects to the laser sensor and moving stage in order to make a scan of laser intensity of different positions of edge or detector.

- Position scanning of signal. This program connects to the moving stage and oscilloscope to scan the signals from detector on different positions. This program is used for most of our experiments.

- Angle scanning of signal. This program connects to the rotation stage and oscilloscope. It is used to measure the relation between laser intensity and induced charge. The laser sensor is also connected for monitoring.

- Remote position control. This program connects the moving stage. It is designed for scanning of special geometry.

- Time scan of signals. This program connects only the oscilloscope to make record waveforms with time. It is only used for streamer test for now.

C.4 Waveform Analysis

Storage and analysis of waveforms are programmed in subroutines.

In the process of calibration, the data is usually analysed and stored in binary files. We can read the files or draw the figure of the data to know the position, intensity or other useful information to decide the next calibration step. After the calibration process, we will store all the waveforms in the experiment. Readout program will unpack the stored file and send the waveforms to analysis function.

Considering that waveform analysis is of great importance to the accuracy on the measurement of gas parameters, it will be detailed discussed in this Section.

C.4.1 Normal analysis

In the test of detectors, time and charge of signal are commonly acquired. In our system, we also perform the time and charge measurement.

Without storage and readout functions, the result is usually the number of measured value. In our experiments, we have the possibility to change the settings of threshold and time window to see the influence of the settings on the experimental result.

C.4.1.1 Time

In the experiments, two channels of the oscilloscope will be activated. One is the signal from a photo-diode in the laser beam using as reference, the other is the signal from pre-amplifier connected to the detector. The trigger is set on the reference signal.

The time we measured is the difference of the time over threshold of detector signal and laser signal. This is the same as other common experiment of detectors.

In our system, we have a larger flexibility in setting the threshold. We can set an absolute threshold as any other experiments, or we can set a relative threshold, which is the percentage of the amplitude of signal. This provides the possibility to compare the time performance for time measured from different signal charge.

C.4.1.2 Charge

After we acquire the time over threshold, we can obtain the signal charge. If we define the start of time window to be t_0, the end of the time window is t_{end}, the current at time t_i is i_i, then the total charge Q measured within the time window is:

$$Q = \sum_{t_0}^{t_{end}} t_i \times i_i \ . \tag{C.1}$$

The start of time window t_0 is defined as $t_0 = t_1 - \Delta t$, where t_1 is the time over threshold, Δt is a small time gap, in our experiment it is usually set at 1 to 100 ns according to waveform.

The end of time window t_{end} is also set manually depending on the shape of waveform. We usually set the t_{end} to the position where the whole peak is contained in the time window.

C.4.1.3   Amplitude

The amplitude is the maximum value in a waveform. Amplitude is often measured to represent the signal charge in other experiments. We also export the amplitude value.

In our experiments, we have discovered that the amplitude is in proportion to the charge. So that the amplitude information is not taken in obtaining the gas parameters.

C.4.2   Removing pedestal

The waveforms acquired in the oscilloscope usually contain a pedestal (or called a baseline). In our system, the pedestal comes from the laser generator. The pedestal signal is associated with the reference signal, as the laser and electrical noise are both from the laser generator. This has provide us the way to remove the noise generated from laser system in the pedestal.

In the beginning of the experiment, we will first make a measurement without any laser input. The number of events is high enough to remove random noise. The waveforms are averaged, and the obtained waveform will be taken as the pedestal of all the measured waveforms in this experiment.

C.4.3   Averaging the waveforms

Because that we have about ± 5 to ± 20 μV random noise, the SNR (signal noise ratio) becomes larger when the signal amplitude is smaller. As we have usually about several thousand waveforms on a position, we can average the waveforms to reduce random noise.

After the waveforms are averaged, the low amplitude signals becomes a clear waveform.

Appendix D

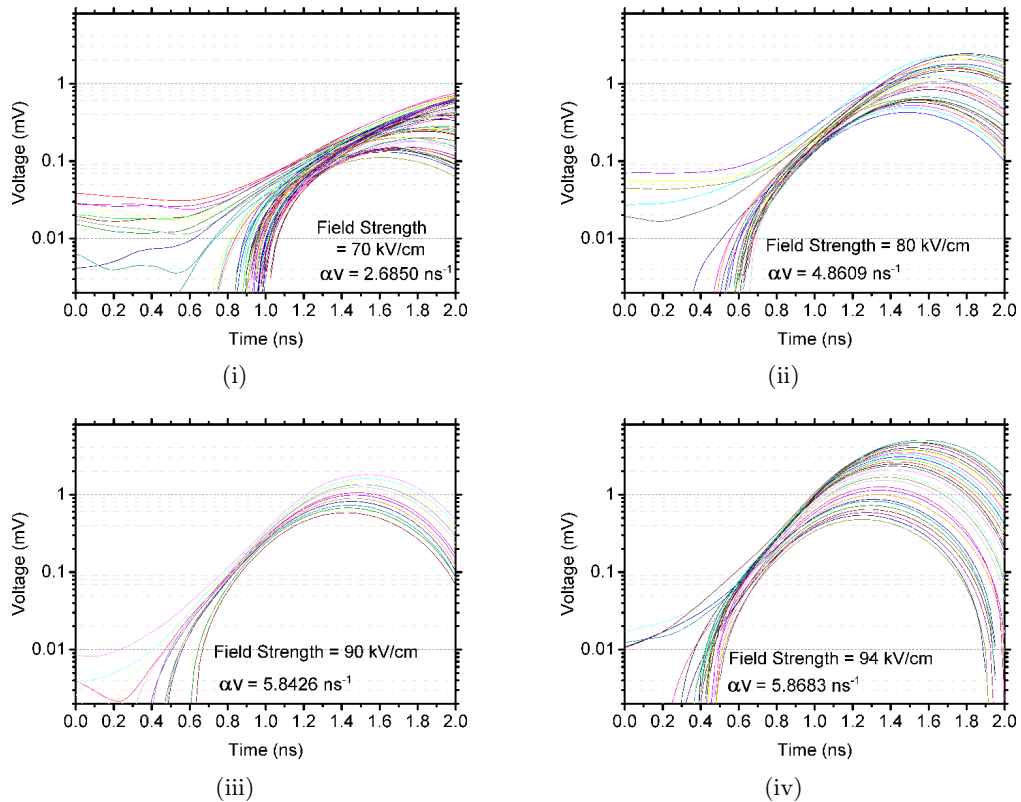# The waveforms from ceramic timing RPC(II)

Figure D.1: The waveforms of timing RPC of different field strengths measured from ceramic RPC(II) in timing RPC mode. Each waveform at a position is averaged from 1000 waveforms to reduce noise. The waveforms are plotted in logarithmic scale. The power of exponential growth is therefore obtained from the slope of the parallel region.
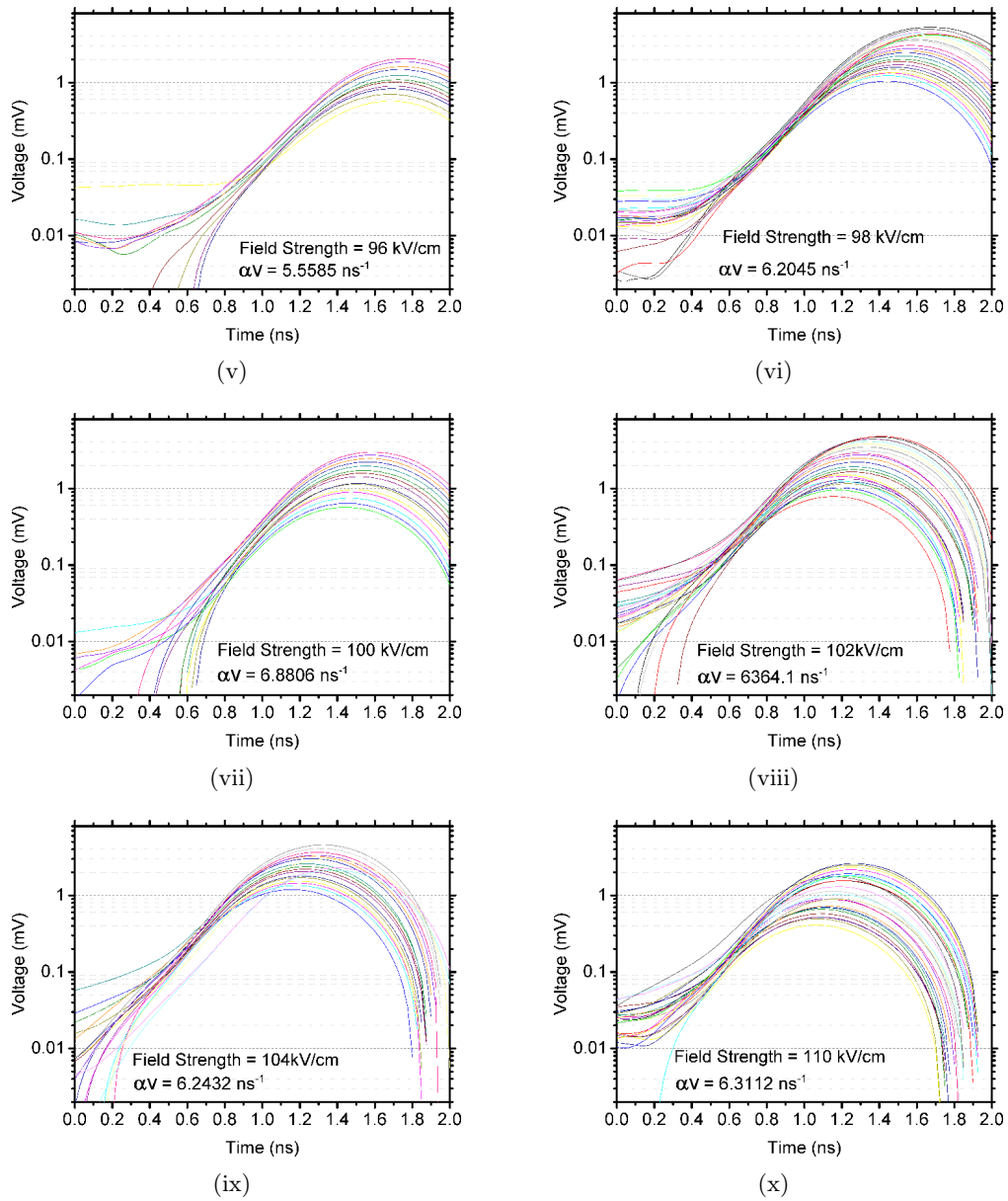
Figure D.1: (Continued figure.)

References

[1] V. Peskov, M. Abbrescia, and P. Fonte. *Resistive Gaseous Detectors: Designs, Performance, and Perspectives.* John Wiley & Sons, 2018.

[2] W. Riegler and C. Lippmann. The physics of resistive plate chambers. *Nucl. Instrum. Meth. A*, 518(1-2):86–90, 2004.

[3] P. Fonte. Survey of physical modelling in resistive plate chambers. *JINST*, 8(11):P11001, 2013.

[4] J. de Urquijo, A. M. Juárez, E. Basurto, et al. Electron swarm coefficients in 1,1,1,2 tetrafluoroethane (R134a) and its mixtures with Ar. *Eur. Phys. J. D.*, 51(2):241–246, 2009.

[5] A. Colucci, E. Gorini, F. Grancagnolo, et al. Measurement of drift velocity and amplification coefficient in $C_2H_2F_4$-isobutane mixtures for avalanche-operated resistive-plate counters. *Nucl. Instrum. Meth. A*, 425(1-2):84–91, 1999.

[6] G. Chiodini, M. R. Coluccia, E. Gorini, et al. Studies of electron drift velocity and charge spectra in RPC by a UV laser source. *Nucl. Instrum. Meth. A*, 602(3):757–760, 2009.

[7] K. Fukushima and T. Hatsuda. The phase diagram of dense QCD. *Rep. Prog. Phys.*, 74(1):014001, 2010.

[8] M. G. Alford, A. Schmitt, K. Rajagopal, et al. Color superconductivity in dense quark matter. *Rev. Mod. Phys.*, 80(4):1455, 2008.

[9] U. Heinz and M. Jacob. Evidence for a new state of matter: An assessment of the results from the CERN lead beam programme. *arXiv preprint nucl-th/0002042*, 2000.

[10] I. Arsene, I. G. Bearden, D. Beavis, et al. Quark-gluon plasma and color glass condensate at RHIC? The perspective from the BRAHMS experiment. *Nucl. Phys. A*, 757(1):1 – 27, 2005.

[11] J. Cleymans, H. Oeschler, and K. Redlich. Particle ratios at sps, ags and sis. *J. Phys. G.*, 25(2):281, 1999.

[12] N.A. Tahir, A. Adonin, C. Deutsch, et al. Studies of heavy ion-induced high-energy density states in matter at the gsi darmstadt sis-18 and future fair facility. *Nucl. Instrum. Meth. A*, 544(1):16 – 26, 2005. Proceedings of the 15th International Symposium on Heavy Ion Inertial Fusion.

[13] Introduction to the CBM experiment, 2017. http://www.gsi.de/fair/experiments/CBM/1intro.html.

[14] P. Senger. Cosmic matter in the laboratory - the compressed baryonic matter experiment at FAIR. *EPJ Web Conf.*, 182:02117, 2018.

[15] P. Senger, T. Galatyuk, A. Kiseleva, et al. The compressed baryonic matter experiment at FAIR. *J. Phys. G.*, 36(6):064037, 2009.

[16] J. M. Heuser. The compressed baryonic matter experiment at FAIR. In *EPJ Web Conf.*, volume 13, page 03001, 2011.

[17] N. Herrmann et al. Technical design report for the CBM time-of-flight system (TOF). GSI-2015-01999.

[18] A. Malakhov and A. Shabunov. Technical design report for the CBM superconducting dipole magnet. GSI-2015-02000.

[19] M. Koziel, A. Dorokhov, J. C. Fontaine, et al. Development of radiation tolerant monolithic active pixel sensors with fast column parallel read-out. *Nucl. Instrum. Meth. A*, 624(2):437–442, 2010.

[20] J. Heuser, W. Müller, V. Pugatch, et al. Technical design report for the CBM silicon tracking system (STS). GSI-2013-05499.

[21] C. Höhne et al. Technical design report for the CBM ring imaging cherenkov detector. GSI-2014-00528.

[22] CBM collaboration. Technical design report for the CBM muon chambers. GSI-2015-02580.

[23] CBM collaboration. The transition radiation detector of the CBM experiment at FAIR : Technical design report for the CBM transition radiation detector (TRD). GSI-2018-01091.

[24] I. E. Korolko, M. S. Prokudin, and Yu. M. Zaitsev. The CBM ECAL. *J. Phys. Conf. Ser.*, 798:012164, 2017.

[25] F. Guber and I. Selyuzhenkov. Technical design report for the CBM projectile spectator detector (PSD). GSI-2015-02020.

[26] M. C. S. Williams. Particle identification using time of flight. *J. Phys. G.*, 39(12):123001, 2012.

[27] C. Lippmann. Particle identification. *Nucl. Instrum. Meth. A*, 666:148–172, 2012.

[28] I. Deppner and N. Herrmann. The CBM time-of-flight system. *arXiv preprint arXiv:1807.02070*, 2018.

[29] E. Berdermann, M. Pomorski, W. De Boer, et al. Diamond detectors for hadron physics research. *Diam. Relat. Mater.*, 19(5-6):358–367, 2010.

[30] L. Naumann, R. Kotte, D. Stach, et al. Ceramics high rate timing RPC. *Nucl. Instrum. Meth. A*, 628(1):138 – 141, 2011.

[31] R. Santonico and R. Cardarelli. Development of Resistive Plate Counters. *Nucl. Instrum. Methods.*, 187(2-3):377–380, 1981.

[32] ARGO-YBJ Collaboration. The ARGO-YBJ Experiment. http://argo.na.infn.it.

[33] M. Ablikim, Z. H. An, J. Z. Bai, et al. Design and construction of the BESIII detector. *Nucl. Instrum. Meth. A*, 614(3):345–399, 2010.

[34] W. J. Llope and STAR Collaboration. Multigap RPCs in the STAR experiment at RHIC. *Nucl. Instrum. Meth. A*, 661:S110–S113, 2012.

[35] A. Airapetian, V. Dodonov, L. Micu, et al. Atlas detector and physics performance: Technical design report. volume 1. *CERN-LHCC*, pages 99–14, 2017.

[36] A. N. Akindinov, A. Alici, F. Anselmo, et al. Latest results on the performance of the multigap resistive plate chamber used for the ALICE tof. *Nucl. Instrum. Meth. A*, 533(1-2):74–78, 2004.

[37] P. Paolucci. The CMS muon system. Technical Report CMS-CR-2006-006, CERN, Apr 2005.

[38] P. Paolucci, R. Hadjiiska, L. Litov, et al. CMS resistive plate chamber overview, from the present system to the upgrade phase i. *JINST*, 8(04):P04005–P04005, 2013.

[39] I. Duerdoth, S. Clowes, J. Freestone, et al. The transition from proportional to streamer mode in a resistive plate chamber. *Nucl. Instrum. Meth. A*, 348(2-3):303–306, 1994.

[40] R. Cardarelli, V. Makeev, and R. Santonico. Avalanche and streamer mode operation of resistive plate chambers. *Nucl. Instrum. Meth. A*, 382(3):470–474, 1996.

[41] T. Moers, H. Tuchscherer, G. L. Bencze, et al. Measurement of the efficiency and time resolution of double-gap resistive plate chambers. *Nucl. Instrum. Meth. A*, 345(3):474–481, 1994.

[42] E. Cerron-Zeballos, I. Crotty, D. Hatzifotiadou, et al. A comparison of the wide gap and narrow gap resistive plate chamber. *Nucl. Instrum. Meth. A*, 373:35–42, 1995.

[43] E. C. Zeballos, I. Crotty, D. Hatzifotiadou, et al. A new type of resistive plate chamber: The multigap RPC. *Nucl. Instrum. Meth. A*, 374(1):132–135, 1996.

[44] A. Akindinov, F. Anselmo, M. Basile, et al. The multigap resistive plate chamber as a time-of-flight detector. *Nucl. Instrum. Meth. A*, 456(1-2):16–22, 2000.

[45] CMS Collaboration. Specialized trigger detector. https://userswww.pd.infn.it/ zotto/ beauty97/rpc.html.

[46] Y. Wang, X. J. Huang, P. F. Lyu, et al. A solution for the inner area of CBM-TOF with pad-MRPC. *Nucl. Instrum. Meth. A*, 845:318–321, 2017.

[47] C. Simon, I. Deppner, N. Herrmann, et al. Performance test of a fully differential float-glass multi-strip MRPC prototype for the CBM ToF wall with cosmic rays. *JINST*, 9(09):C09028, 2014.

[48] I. Deppner, N. Herrmann, M. Ciobanu, et al. A glass type Multistrip-MRPC prototype for the low rate region of the CBM time-of-flight wall. *JINST*, 7(10):P10008, 2012.

[49] I. Deppner, N. Herrmann, J. Fruhauf, et al. Performance studies of MRPC prototypes for CBM. *JINST*, 11(10):C10006, 2016.

[50] W. P. Zhu, Y. Wang, S. Q. Feng, et al. A real-size MRPC developed for CBM-TOF. *Sci. China. Technol. Sc.*, 56(11):2821–2826, 2013.

[51] M. Petriş, D. Bartoş, G. Caragheorgheopol, et al. Time and position resolution of high granularity, high counting rate MRPC for the inner zone of the CBM-TOF wall. *JINST*, 11(09):C09009, 2016.

[52] A. Akindinov, J. Dreyer, X. Fan, et al. Radiation-hard ceramic resistive plate chambers for forward TOF and T_0 systems. *Nucl. Instrum. Meth. A*, 845:203–205, 2017.

[53] A. Laso Garcia. Timing resistive plate chambers with ceramic electrodes. PhD Thesis, TU-Dresden, 2014.

[54] R. Cardarelli, A. Diciaccio, and R. Santonico. Performance of a resistive plate chamber operating with pure CF_3Br. *Nucl. Instrum. Meth. A*, 333(2-3):399–403, 1993.

[55] M. Abbrescia, E. Bisceglie, G. Iaselli, et al. An environmental safe gas mixture for resistive plate chambers operated at low pressure. *Nucl. Instrum. Meth. A*, 417(1):16–23, 1998.

[56] United States Environmental Protection Agency (EPA). Understanding Global Warming Potentials. https://www.epa.gov/ghgemissions/understanding-global-warming-potentials.

[57] R. Guida, M. Capeans, and B. Mandelli. Characterization of RPC operation with new environmental friendly mixtures for LHC application and beyond. *JINST*, 11(07):C07016, 2016.

[58] Regulation (EU) No 517/2014 of the european parliament and of the council of 16 April 2014 on fluorinated greenhouse gases and repealing regulation (EC) No 842/2006. *Official J. Eur. Union*, 57(L 150):195–230, 2014.

[59] D. M. Rossi and H. Simon. A closed-circuit gas recycling system for RPC detectors. *Nucl. Instrum. Meth. A*, 661:S230–S233, 2012.

[60] G. Saviano, M. Ferrini, L. Benussi, et al. Properties of potential eco-friendly gas replacements for particle detectors in high-energy physics. *JINST*, 13(03):P03012, 2018.

[61] L. Benussi, S. Bianco, M. Ferrini, et al. A study of HFO-1234ze (1, 3, 3, 3-Tetrafluoropropene) as an eco-friendly replacement in RPC detectors. *arXiv preprint arXiv:1505.01648*, 2015.

[62] M. Abbrescia, L. Benussi, D. Piccolo, et al. Eco-friendly gas mixtures for resistive plate chambers based on tetrafluoropropene and Helium. *JINST*, 11(08):P08019, 2016.

[63] B. Yongwook, K. Do-won, P. Woosung, et al. MRPC with eco-friendly gas. *arXiv preprint arXiv:1806.00649*, 2018.

[64] W. Riegler, C. Lippmann, and R. Veenhof. Detector physics and simulation of resistive plate chambers. *Nucl. Instrum. Meth. A*, 500(1-3):144–162, 2003.

[65] W. Riegler. Induced signals in resistive plate chambers. *Nucl. Instrum. Meth. A*, 491(1-2):258–271, 2002.

[66] R. Arnaldi, A. Baldit, V. Barret, et al. A low-resistivity RPC for the ALICE dimuon arm. *Nucl. Instrum. Meth. A*, 451(2):462–473, 2000.

[67] A. Akindinov, V. Ammosov, V. Gapienko, et al. RPC with low-resistive phosphate glass electrodes as a candidate for the CBM TOF. *Nucl. Instrum. Meth. A*, 572(2):676–681, 2007.

[68] Y. Wang, J. B. Wang, Q. Yan, et al. A prototype of a high rating MRPC. *Chin. Phys. C*, 33(5):374–377, 2009.

[69] D. Gonzalez-Diaz, D. Belver, A. Blanco, et al. The effect of temperature on the rate capability of glass timing RPCs. *Nucl. Instrum. Meth. A*, 555(1):72 – 79, 2005.

[70] G. Aielli, C. Bacci, B. Bartoli, et al. Temperature effect on RPC performance in the ARGO-YBJ experiment. *Nucl. Instrum. Meth. A*, 608(2):246–250, 2009.

[71] P. Camarri, R. Cardarelli, A. Di Ciaccio, et al. Streamer suppression with SF_6 in RPCs operated in avalanche mode. *Nucl. Instrum. Meth. A*, 414(2-3):317–324, 1998.

[72] G. Brunner. Townsend coefficients of gases in avalanche counters. *Nucl. Instrum. Methods*, 154(1):159–163, 1978.

[73] C. Lippmann. Detector physics of resistive plate chambers. PhD Thesis, U. Frankfurt, 2003.

[74] H. Anderhub, M. J. Devereux, and P.-G. Seiler. On a new method for testing and calibrating ionizing particle detectors. *Nucl. Instrum. Methods*, 166(3):581 – 582, 1979.

[75] H. J. Hilke. On the formation and application of laser-induced ionization tracks in gases. *Nucl. Instrum. Methods*, 174(1-2):145–149, 1980.

[76] J. Bourotte and B. Sadoulet. Ionization of Multiwire Proportional Chamber gas by double photon-absorption. *Nucl. Instrum. Methods*, 173(3):463–470, 1980.

[77] M. Desalvo and R. Desalvo. Measurement of laser-induced ionization in an Argon Ethane gas-mixture. *Nucl. Instrum. Methods.*, 201(2-3):357–360, 1982.

[78] J. C. Guo, F. G. Hartjes, and J. Konijn. The use of laser-induced electron clusters for drift chamber tests. *Nucl. Instrum. Methods.*, 204(1):77–83, 1982.

[79] C. Raine, K. W. D. Ledingham, and K. M. Smith. Laser-induced ionization in proportional-counters. *Nucl. Instrum. Methods.*, 217(1-2):305–310, 1983.

[80] K. W. D. Ledingham, C. Raine, K. M. Smith, et al. Wavelength dependence of laser-induced ionization in proportional-counters. *Nucl. Instrum. Meth. A*, 241(2-3):441–447, 1985.

[81] G. Hubricht, K. Kleinknecht, E. Muller, et al. Ionization of counting gases and ionizable gaseous additives in proportional chambers by UV lasers. *Nucl. Instrum. Meth. A*, 228(2-3):327–333, 1985.

[82] H. J. Hilke. Detector calibration with lasers - a review. *Nucl. Instrum. Meth. A*, 252(2-3):169–179, 1986.

[83] J. Abele, J. Berkovitz, J. Boehm, et al. The laser system for the STAR time projection chamber. *Nucl. Instrum. Meth. A*, 499(2-3):692–702, 2003.

[84] A. Lebedev. A laser calibration system for the STAR TPC. *Nucl. Instrum. Meth. A*, 478(1-2):163–165, 2002.

[85] E. M. Gushchin and S. V. Somov. On the laser calibration of charged particle detectors. *Instrum. Exp. Tech.*, 43(4):470–480, 2000.

[86] J. De Urquijo, C. A. Arriaga, C. Cisneros, et al. A time-resolved study of ionization, electron attachment and positive-ion drift in methane. *J. Phys. D.*, 32(1):41, 1999.

[87] V. Golovatyuk, F. Grancagnolo, and R. Perrino. Laser beam studies of RPC behaviour in avalanche mode. *Nucl. Instrum. Meth. A*, 508(1-2):29–33, 2003.

[88] P. Fonte, A. Mangiarotti, S. Botelho, et al. A dedicated setup for the measurement of the electron transport parameters in gases at large electric fields. *Nucl. Instrum. Meth. A*, 613(1):40–45, 2010.

[89] L. Naumann, M. Siebold, M. Kaspar, et al. Precision measurement of timing RPC gas mixtures with laser-beam induced electrons. *JINST*, 9(10):C10009, 2014.

[90] W. S. Boyle and P. Kisliuk. Departure from paschen's law of breakdown in gases. *Phys. Rev.*, 97(2):255, 1955.

[91] M. Loeser, M. Siebold, F. Roeser, et al. High energy CPA-free picosecond Yb: YAG amplifier. In *Advanced Solid-State Photonics*, pages AM4A–16.

[92] M. Siebold, M. Loeser, F. Roeser, et al. High energy Yb:YAG active mirror laser system for transform limited pulses bridging the picosecond gap. *Laser Photonics Rev.*, 10(4):673–680, 2016.

[93] National Instruments Corporation. Labview user manual. 1998.

[94] C. E. Garcia-Ortiz, E. Pisano, and V. Coello. Description and characterization of plasmonic Gaussian beams. *J. Opt.*, 19(8):085001, 2017.

[95] K. Burnett and M. H. R. Hutchinson. Multiphoton physics. *J. Mod. Opt*, 36(7):811–816, 1989.

[96] C. K. Rhodes. Multiphoton ionization of atoms. *Science*, 229(4720):1345–51, 1985.

[97] G. Mainfray and C. Manus. Multiphoton ionization of atoms. *Rep. Prog. Phys.*, 54(10):1333–1372, 1991.

[98] S. L. Chin. *From multiphoton to tunnel ionization*. World Scientific, 2004.

[99] P. Gibbon. *Short pulse laser interactions with matter*. World Scientific Publishing Company Singapore, 2004.

[100] S. L. T. Drysdale, K. W. D. Ledingham, C. Raine, et al. Detection of toluene in a proportional counter gas by resonant two photon ionisation spectroscopy. *Nucl. Instrum. Meth. A*, 252(2):521 – 523, 1986.

[101] F. Bossu, M. Gagliardi, M. Marchisone, et al. Performance of the RPC-based ALICE muon trigger system at the LHC. *JINST*, 7(12):T12002, 2012.

[102] H. Raether. *Electron avalanches and breakdown in gases*. Butterworth, 1964.

[103] A. V. Oppenheim, A. S. Willsky, and S. H. Nawab. *Signals and systems, vol. 2*, volume 6. Prentice-Hall Englewood Cliffs, NJ, 1983.

[104] S. An, Y. K. Jo, J. S. Kim, et al. A 20 ps timing device—a multigap resistive plate chamber with 24 gas gaps. *Nucl. Instrum. Meth. A*, 594(1):39 – 43, 2008.

[105] A. Akindinov, A. Alici, F. Anselmo, et al. A study of the multigap RPC at the gamma irradiation facility at CERN. *Nucl. Instrum. Meth. A*, 490(1-2):58–70, 2002.

[106] M. Titov. *Radiation damage and long-term aging in gas detectors*. World Scientific, 2004.

[107] P. Fonte. High-resolution timing of mips with RPCs - a model. *Nucl. Instrum. Meth. A*, 456(1-2):6–10, 2000.

[108] L. N. Dobretsov and M. V. Gomoyunova. *Emission electronics*. Keter Press, 1971.

[109] M. Radmilovic-Radjenovic, B. Radjenovic, A. Bojarov, et al. The breakdown mechanisms in electrical discharges: The role of the field emission effect in direct current discharges in micro gaps. *Acta Phys. Slovaca*, 63(3):105–205, 2013.

Acknowledgement

Erklärung

Hiermit versichere ich, dass ich die vorliegende Arbeit ohne unzulässige Hilfe Dritter und ohne Benutzung anderer als der angegebenen Hilfsmittel angefertigt habe. Die aus fremden Quellen direkt oder indirekt übernommenen Gedanken sind als solche kenntlich gemacht. Die Arbeit wurde bisher weder im Inland noch im Ausland in gleicher oder ähnlicher Form einer anderen Prüfungsbehörde vorgelegt.

Xingming Fan

Dresden, am